10. TITAN-I FUSION-POWER-CORE ENGINEERING

Steven P. Grotz
James P. Blanchard
Edward T. Cheng
Patrick I. H. Cooke
Richard L. Creedon
William P. Duggan
Nasr M. Ghoniem
Mohammad Z. Hasan
Robert A. Krakowski
Rodger C. Martin
Farrokh Najmabadi
George O. Orient
Kenneth R. Schultz
Shahram Sharafat
Don Steiner
Dai-Kai Sze
Carl Weggel
Clement P. C. Wong

Contents

10. TITAN-I FUSION-POWER-CORE ENGINEERING

10.1. INTRODUCTION

The TITAN-I reactor is a compact, high-neutron-wall-loading ($18\,MW/m^2$) design. The TITAN-I fusion power core (FPC) is cooled by liquid lithium and uses a vanadium alloy (V-3Ti-1Si) as the structural material. An overview of the TITAN-I design is given in Section 9. Figures 10.1-1 and 10.1-2 show the elevation view and the poloidal cross section of the TITAN-I FPC. Global parameters of the design are summarized in Table 10.1-I. A detailed list of the TITAN-I operating parameters can be found in Appendix A.

In this section, the detailed engineering design and analysis of the TITAN-I FPC is presented. The FPC components considered here are the reactor torus (including the first wall, blanket, and divertor), hot shield, and coil sets. The areas of materials (Section 10.2), neutronics (Section 10.3), thermal and structural design (Section 10.4), magnet engineering (Section 10.5), and power-cycle analysis (Section 10.6) are discussed. Other engineering aspects of the TITAN-I design, such as divertor and vacuum engineering, tritium systems, safety and waste disposal, and maintenance are presented in Sections 12 through 14.

The emphasis of the TITAN study has been on the investigation and demonstration of the feasibility of the compact, high-power-density reactors and also identification of the critical issues for these devices. Therefore, some of the engineering issues that were not considered crucial to the design were for the most part not covered in detail in this study.

10.2. MATERIAL SELECTION

The attractiveness of commercial fusion power devices depends to a large extent on material performance. Components of a fusion reactor are exposed to a unique set of stress, thermal, radiation, electromagnetic, and chemical loads and should function properly for the duration of the design lifetime. Material options are even more limited

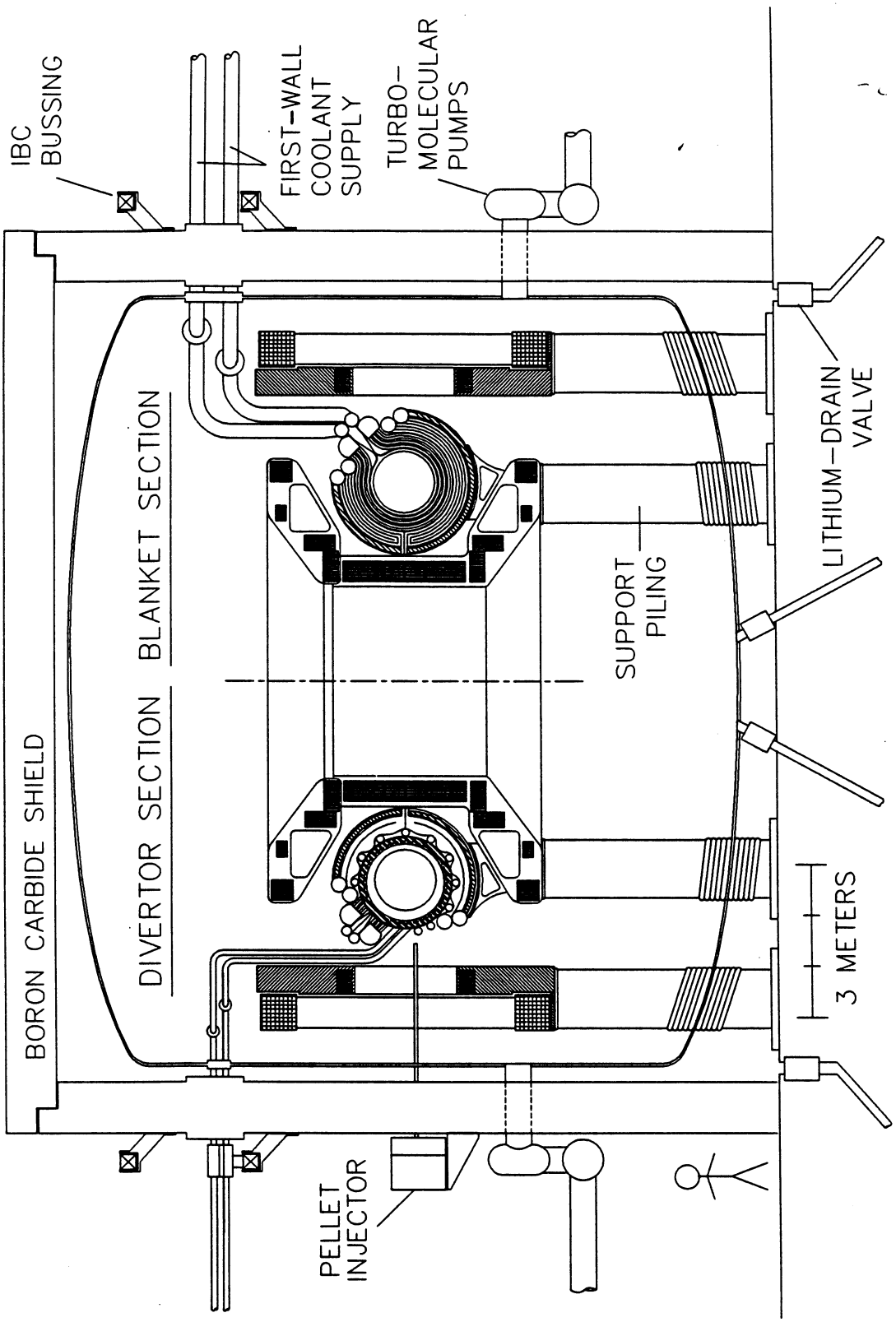

Figure 10.1-1. Elevation view of the TITAN-I fusion power core.

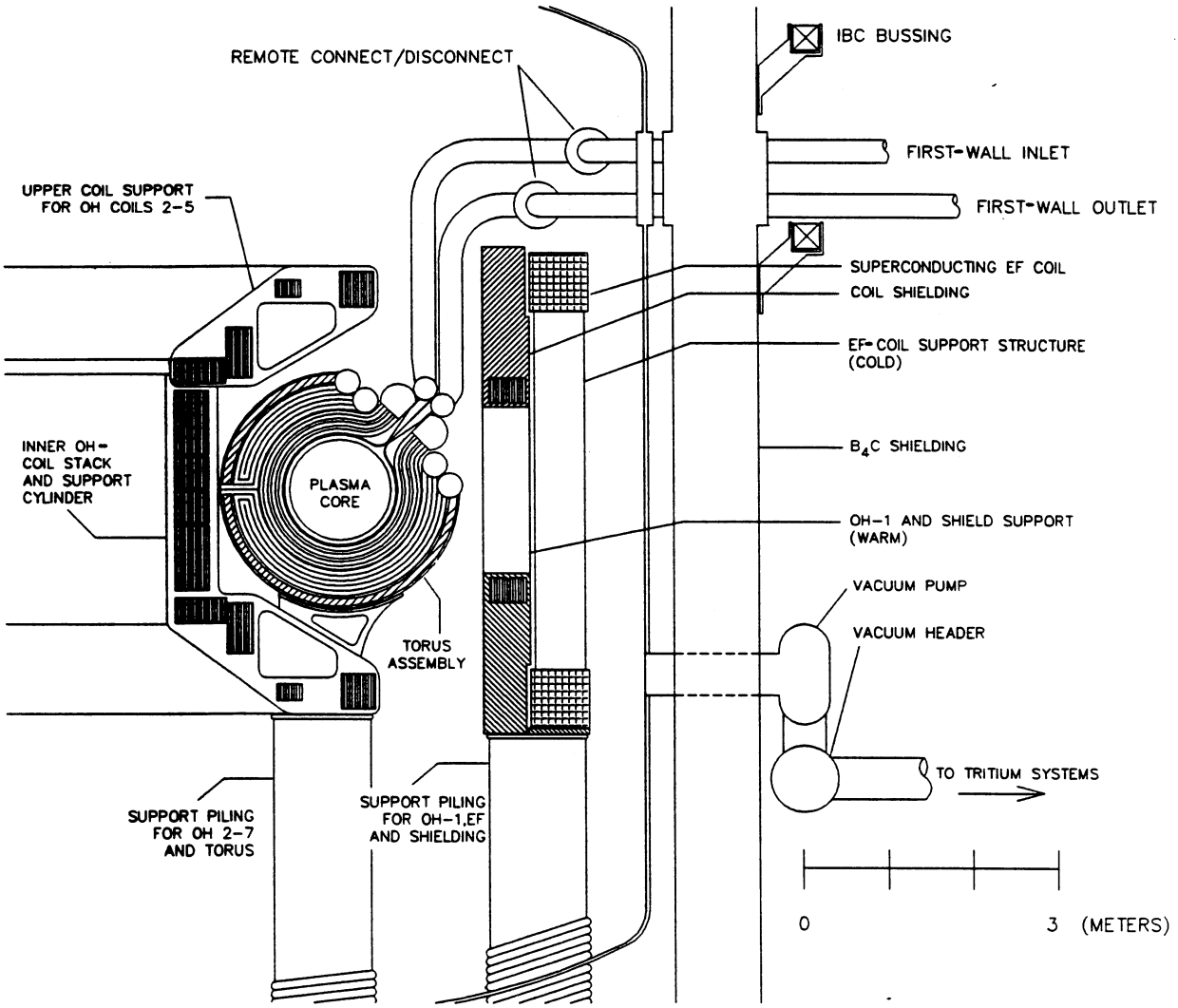

Figure 10.1-2. Poloidal cross section of the TITAN-I fusion power core.

for a compact, high-power-density reactor such as TITAN because of high heat and radiation fluxes. Safety and waste-management criteria further restrict material options; the goal of the TITAN reactor study has been to satisfy Class-C waste disposal criteria and achieve a Level-2 of safety assurance (Section 13).

The following sections highlight various material selection issues for FPC components. Section 10.2.1 focuses on structural material. The TITAN-I design uses liquid lithium

Table 10.1-I.

TITAN-I OPERATING PARAMETERS

Major toroidal radius, R_T	3.90	m
Minor plasma radius, r_p	0.60	m
First-wall radius, r_{FW}	0.66	m
Primary coolant	Lithium	
Structural material	V-3Ti-1Si	
Coolant inlet temperature, T_{in}	320	°C
First-wall-coolant exit temperature, $T_{ex,FW}$	440	°C
Blanket-coolant exit temperature,$T_{ex,B}$	700	°C
Pumping power, P_{pump}	48.1	MWe
Neutron wall load, I_w	18.1	MW/m^2
Radiation heat flux on first wall, q''_o	4.6	MW/m^2
Fusion power, P_f	2301	MW
Total thermal power, P_{th}	2935	MW
Net electric power, P_{net}	970	MWe
Gross efficiency, η_{gross}	44%	
Net efficiency, η_{net}	33%	
Mass power density, MPD	757	kWe/tonne

as the primary coolant. A discussion of the compatibility of liquid lithium with the structural material is given in Section 10.2.2. In Section 10.2.3 options for insulator materials are presented. Results are summarized in Section 10.2.4.

10.2.1. Structural Material

The advantage of vanadium-base alloys over others for fusion reactor structural materials has been pointed out in previous publications [1,2]. In particular, when compared with ferritic-steel alloys, vanadium-base alloys exhibit better physical, mechanical, and nuclear properties. For example, compared to HT-9, vanadium-base alloys have a higher melting temperature, a lower thermal expansion coefficient, and a lower density. Furthermore, compared to ferritic alloys at $1\,\mathrm{MW/m^2}$ of neutron wall load, vanadium-base alloys have about half the nuclear heating rate ($\sim 25\,\mathrm{W/cm^3}$), about a third of the helium generation rate ($\sim 57\,\mathrm{He}$ appm), about half the hydrogen production rate ($\sim 240\,\mathrm{H}$ appm/MW y/m^2), and lower long-term afterheat [1].

The high melting temperature of vanadium alloys ($T_m = 1890\,^\circ\mathrm{C}$) has significant bearing on safety related issues. The higher ultimate tensile strength ($\sigma_u \sim 600\,\mathrm{MPa}$ at $600\,^\circ\mathrm{C}$), the lower expansion coefficient, and the slightly higher thermal conductivity of vanadium-base alloys are reflected in higher thermal stress factors when compared to HT-9 [1]. The thermal stress factor is a measure of heat load capability. The high T_m, coupled with a high thermal stress factor, promises a high operating temperature and a high-neutron-wall-loading capability. High T_m combined with a low helium production rate is also desirable for fusion reactor materials, since below $\sim 0.5\ T_m$ (K), strength and ductility are retained and fracture remains transgranular [3] ($0.5\,T_m$: vanadium $\simeq 1082\,\mathrm{K}$, HT-9 $\simeq 846\,\mathrm{K}$). Because helium embrittlement is directly related to the helium production rate, a low helium generation rate in vanadium-base alloys is a favorable characteristic.

After consideration of several vanadium-base alloys, the V-3Ti-1Si alloy was chosen as the primary structural material for TITAN-I. Table 10.2-I shows selected properties of vanadium-base alloys. These values were adopted for the TITAN-I structural alloy throughout the study because physical properties of vanadium-base alloys are not sensitive to moderate compositional variations [1].

In the following subsections, the effects of gaseous transmutations (*i.e.*, hydrogen and helium) on the mechanical properties of vanadium-base alloys are first discussed (Section 10.2.1.1). Based on extrapolation of the limited available data to TITAN-I

Table 10.2-I.

PHYSICAL PROPERTIES OF VANADIUM-BASE ALLOYS [1] (ADOPTED FOR V-3Ti-1Si)

Atomic weight	50.9	
Density[(a)]	6100	kg/m^3
Crystal structure	b.c.c.	
Melting temperature	1890	°C
Boiling temperature	3400	°C
Heat of fusion	143	kJ/kg
Heat of vaporization	2265	kJ/kg
Heat capacity		
at 400 °C	535	J/kg-K
at 500 °C	560	J/kg-K
at 600 °C	575	J/kg-K
Thermal conductivity		
at 400 °C	26.8	W/m-K
at 500 °C	28.0	W/m-K
at 600 °C	29.5	W/m-K
Coefficient of thermal expansion		
at 400 °C	10.2×10^{-6}	/K
at 500 °C	10.3×10^{-6}	/K
at 600 °C	10.5×10^{-6}	/K
Electrical resistivity		
at 400 °C	0.67	$\mu\Omega$ m
at 500 °C	0.74	$\mu\Omega$ m
at 600 °C	0.81	$\mu\Omega$ m
Poisson ratio	0.36	
Young's modulus	127	GPa

(*a*) Properties are at room temperature.

operating conditions, irradiation hardening and helium and hydrogen embrittlement of V-3Ti-1Si set an upper limit of approximately 18 MW y/m^2 for the TITAN-I first wall. Irradiation-induced swelling of the V-3Ti-1Si alloy was also investigated, and it was concluded that swelling would be negligible for the lifetime of the TITAN-I first wall. The creep behavior of V-3Ti-1Si was estimated by using minimum-commitment method, and based on the anticipated end-of-life mechanical properties of the alloy, a maximum allowable design stress was determined (Sections 10.2.1.2 and 10.2.1.3).

10.2.1.1. Embrittlement

Hydrogen generation in structural material during irradiation may cause hydrogen embrittlement. Loomis and Carlson [4] have reported that hydrogen concentrations above 5000 appm are required to raise the ductile-to-brittle transition temperature (DBTT) of vanadium above room temperature. Table 10.2-II shows anticipated hydrogen and helium production rates in the V-3Ti-1Si alloy first-wall structure exposed to an 18.1 MW/m^2 neutron wall loading. The hydrogen production rate in the TITAN-I first wall is slightly below the 5000 appm necessary to cause any significant increase in the DBTT following one full-power year (FPY) of operation.

Since the hydrogen concentration required for the formation of hydrides in metals is generally large, hydrogen production and pickup has not been of much concern [5]. Vanadium-hydrogen interactions are discussed in Section 10.2.2.2. In principle, vanadium forms stable hydrides only at relatively low temperatures ($< 400\,^{\circ}$C). When the structure is kept at temperatures above 400 °C, most of the hydrogen will migrate down the temperature gradient towards the coolant. It should be noted, however, that in addition to transmutations, tritium will also penetrate the first wall from the plasma side. Some aspects of plasma-driven tritium permeation through the first wall are discussed in Section 12.2.

Helium, unlike hydrogen, will not generally diffuse out of the metal at normal operating temperatures. Instead, helium accumulates inside the matrix to form helium-filled bubbles. These bubbles form mainly along the grain boundaries and sometimes inside the grain material. The formation of helium bubbles on grain boundaries is the basic mechanism responsible for helium embrittlement in materials exposed to high levels of neutron irradiation. Neutron irradiation increases the number of trapping sites available for nucleation of helium bubbles. The combined effects of helium generation plus irradiation-produced defects have been investigated recently [6]. Helium was pre-implanted into the vanadium-base alloy samples and then irradiated in the fast-flux test facility to up to

Table 10.2-II.

HYDROGEN AND HELIUM PRODUCTION RATES IN THE TITAN-I FIRST WALL (V-3Ti-1Si)[a]

Isotope	appm/y
H	4267
D	225
T	24
Total Hydrogen	4516
^{4}He	1018
^{3}He	*nil*
Total Helium	1018

(*a*) For 15 MW y/m^2 neutron fluence.

40 dpa. These studies were undertaken to examine and compare the response of different vanadium-base alloys to the anticipated high-energy neutron irradiation in fusion devices.

Among the various vanadium-base alloys, the most promising candidates for fusion reactor applications are V-15Cr-5Ti, VANSTAR-7 (V-9Cr-3Fe-1Zr), and V-3Ti-1Si. Previously, the V-15Cr-5Ti alloy received considerable attention [2]. In particular V-15Cr-5Ti has a higher thermal-creep resistance than the other two alloys. Investigation of the effects of neutron irradiation with pre-implanted helium atoms, however, suggests that V-15Cr-5Ti may be subject to unacceptable losses in ductility. Braski [6] irradiated specimens of V-15Cr-5Ti, V-3Ti-1Si, and VANSTAR-7 at 420, 520, and 600 °C to a damage level of 40 dpa and implanted helium atoms up to a concentration of 80 appm. Tensile tests showed that helium pre-implanted V-15Cr-5Ti had zero ductility in tension after irradiation at 600 °C. Under the same conditions, VANSTAR-7 and V-3Ti-1Si retained uniform elongations of about 3.3% and 8.3%, respectively. Figure 10.2-1 shows the stress-strain behavior of the candidate vanadium-base alloys before and after irradiation. These

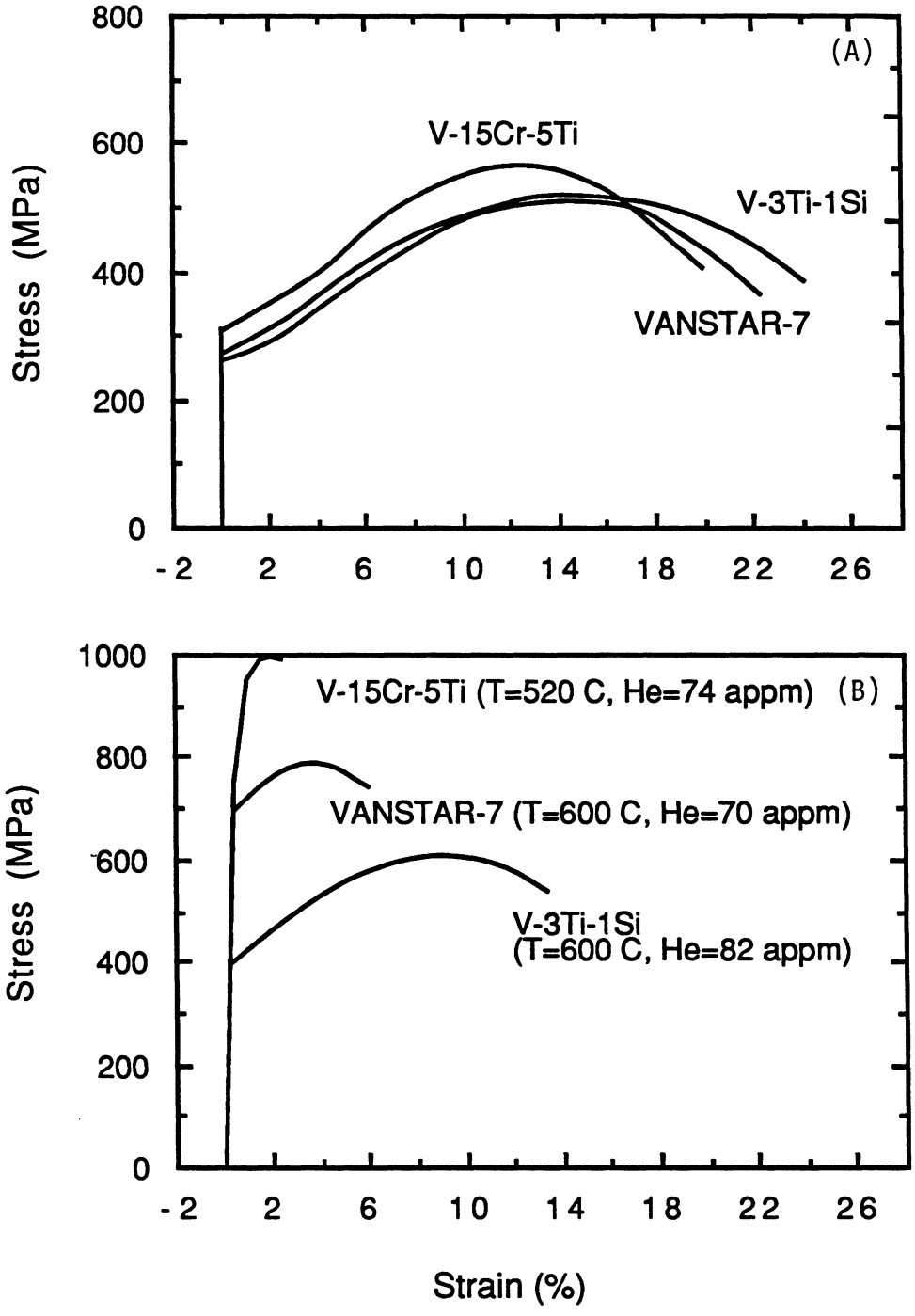

Figure 10.2-1. Stress-strain behavior of three unirradiated (A) and irradiated (B) candidate vanadium-base alloys [6].

Table 10.2-III.

SWELLING, $\Delta V/V$ (%), OF THREE VANADIUM-BASE ALLOYS [6][(a)]

Alloy	420 °C	520 °C	620 °C
V-3Ti-1Si	0.09	0.002	0.05
VANSTAR-7	0.004	6.0	0.06
V-15Cr-5Ti	0.005	0.005	0.3

(*a*) Irradiated to 40 dpa with a He content of $\sim$ 80 appm.

measurements indicate that V-3Ti-1Si suffers the least amount of irradiation hardening and helium embrittlement.

Table 10.2-III shows the swelling results of the three vanadium-base-alloy samples with pre-implanted helium. The data, although limited, indicate that the V-3Ti-1Si alloy has the lowest swelling rates at temperatures above 500 °C after 40 dpa. Using the above test data and assuming a linear swelling behavior, the maximum swelling ($\Delta V/V$) of the TITAN-I first wall would be $\sim$ 0.2% after 1 FPY of operation (164 dpa). Thus, a reasonable extrapolation of Braski's results [6] indicates that neutron-radiation-induced swelling of V-3Ti-1Si could be negligible.

Because the above test data show that V-3Ti-1Si has the lowest swelling, irradiation hardening, and helium embrittlement rates, this alloy is chosen as the primary structural material for the TITAN-I reactor design.

10.2.1.2. Creep behavior

Creep may be defined as the time-dependent deformation of the material under an applied load. Creep is a complex mechanism that depends on stress, strain, time, temperature, and microstructure. In a radiation environment, microstructural changes are generally accelerated, and drastic effects on the creep behavior of metals can be expected. Many mechanisms which may cause creep have been identified, such as dislocation creep, diffusion creep, grain-boundary sliding, and irradiation creep. Except for the irradiation

creep mechanism, the others involve deformation of the solid by overcoming internal barriers caused by the thermal activation or applied stresses. Irradiation creep involves the production of internal stresses which are greater than the external stresses because of irradiation-induced microstructural changes. The material then creeps under the influence of this internal stress. Because of the complexity of creep deformation, designers rely heavily on empirical equations to predict creep deformation. For vanadium-base alloys, the expected service life is much longer than the duration for which experimental creep data are available. Extrapolation of the creep data, in particular the creep-rupture data, to longer times has been studied extensively over the past decades [7 - 9].

Widely used extrapolation techniques for creep-rupture data include the Larson-Miller, White-LeMay, and Orr-Sherby-Dorn methods [7]. These methods predict the value of the rupture time (t_r) as a function of the material temperature and for different applied stresses. The choice and success of these methods depends on the behavior of the creep-rupture data and assumed pattern for the data in each method. As a result, it is possible for these methods to predict very different values of stresses appropriate to long-life conditions [7]. To overcome this problem, the minimum-commitment method (MCM) was developed at NASA [8] to extrapolate creep-rupture data, without forcing the creep data to any specific pattern. Ghoniem *et al.* [9] developed a modified-minimum-commitment method (MMCM) in which the stress, the time to rupture, and the temperature are related by the following functional form:

$$\ln(\sigma_r) = A(T) + B(T)\ln(t_r)\,, \tag{10.2-1}$$

where σ_r is the stress to rupture in MPa, t_r is the time to rupture in hours, and $A(T)$ and $B(T)$ are temperature-dependent parameters given by:

$$A(T) = a_o + a_1 T \qquad \text{and} \qquad B(T) = b_o + b_1 T\,. \tag{10.2-2}$$

The temperature (T) is in Kelvin and a_o, a_1, b_o, and b_1 are constants determined by fitting creep-rupture data. The coefficients of Equation 10.2-2 for V-3Ti-1Si and V-15Cr-5Ti are given in Table 10.2-IV.

Creep-rupture stress data for vanadium alloys, in particular V-3Ti-1Si, is very limited. Some V-3Ti-1Si creep-rupture stress data [10] are available at 750 and 850 °C. At 650 °C, data were found only for a V-3Ti alloy containing unspecified amounts of silicon. The creep-rupture data at these three temperatures is used to develop a phenomenological stress-rupture equation (similar to Equation 10.2-1). A similar equation was also developed for V-15Cr-5Ti using more recent creep-rupture data [11].

Table 10.2-IV.

COEFFICIENTS FOR THE CREEP-RUPTURE STRESS EQUATION

Coefficient	V-3Ti-1Si	V-15Cr-5Ti
a_o	9.507209	7.239522
a_1	-3.50498×10^{-3}	-1.04844×10^{-3}
b_o	4.85748×10^{-1}	2.17853×10^{-2}
b_1	-6.07858×10^{-4}	-7.38258×10^{-5}

Figure 10.2-2 shows the experimental data points [10] and MMCM calculational results (lines) for the creep-rupture stress of V-3Ti-1Si at several temperatures, as well as the expected stress range in the first wall of TITAN-I during normal and off-normal operation. Based on the results of the MMCM extrapolation equation, operation of the first wall at a pressure close to 100 MPa and at temperatures below 700 °C will not lead to creep rupture within one year of normal operation. During off-normal conditions, coolant pressure is lost and creep rupture would not occur even if the structure were kept at elevated temperatures (1000 °C) for a prolonged period of time. However, high-temperature (850 °C) creep-rupture data are necessary to gain more confidence in the creep-rupture behavior at these higher temperatures.

Among the three candidate vanadium-base alloys, V-15Cr-5Ti has the highest resistance to thermal creep. For the purpose of comparison, a creep-rupture equation using the MMCM was also developed for V-15Cr-5Ti. Figure 10.2-3 shows the data and the extrapolated creep-rupture curves for V-15Cr-5Ti. Note that the creep-rupture stresses for V-15Cr-5Ti are well above 100 MPa at all temperatures, while those of V-3Ti-1Si fall below 100 MPa, depending on temperature and holding time.

Recovery of dislocations in vanadium-base alloys starts at $\sim$ 800 °C. Above 900 °C, recrystallization (realignment of grain boundaries) sets in and around 1000 to 1100 °C grain growth begins. For design purposes, measurements of the 50% recrystallization temperatures are necessary (50% recrystallization temperature is the temperature at which 50% of the base material is completely recrystallized during a specified holding time). Because

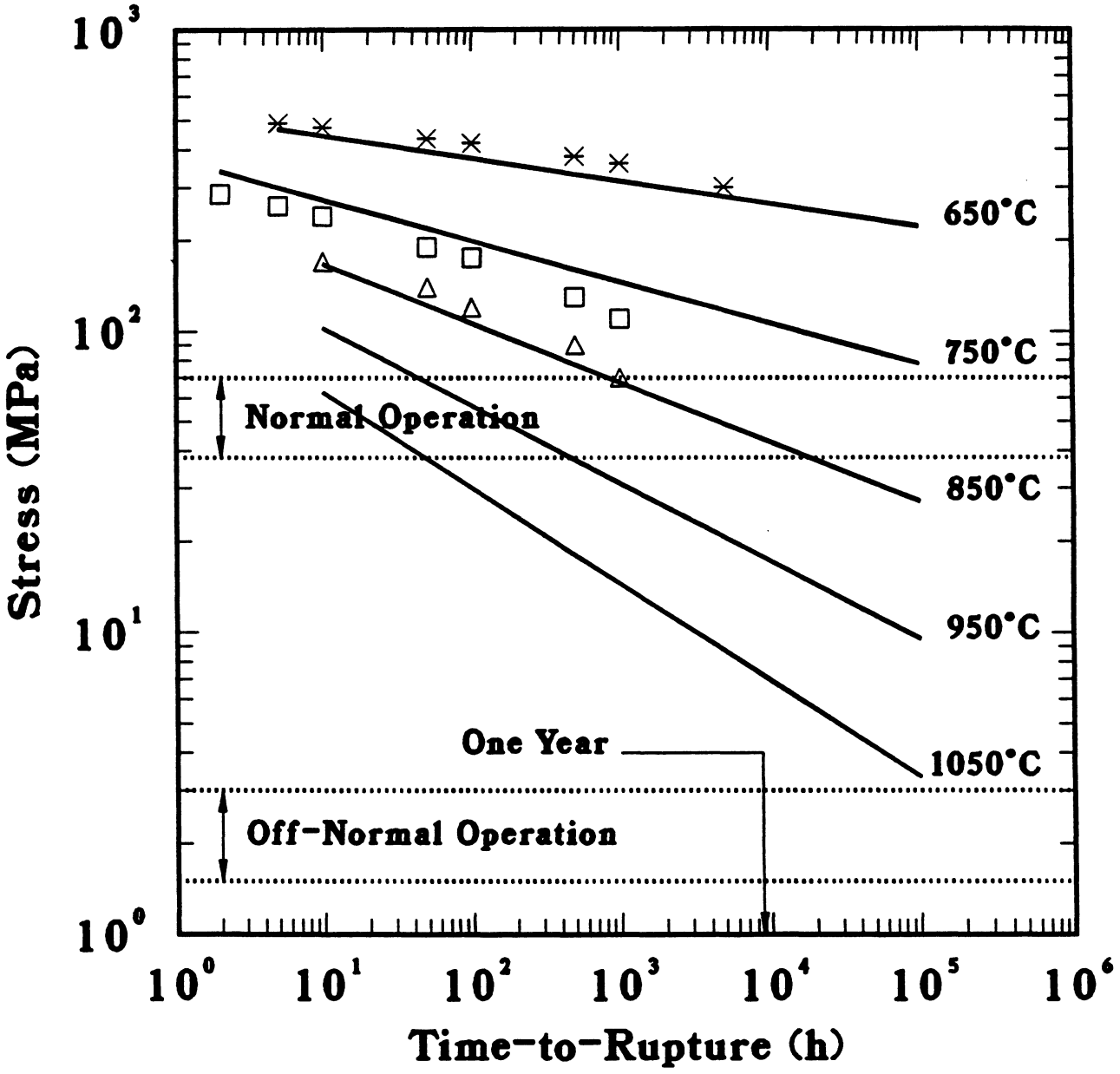

Figure 10.2-2. Creep-rupture stresses of V-3Ti-1Si at various temperatures. Symbols are creep-rupture data points [10] and solid lines are estimates using MMCM [9]. Also shown are the expected stress ranges during normal and off-normal operations of the TITAN-I design.

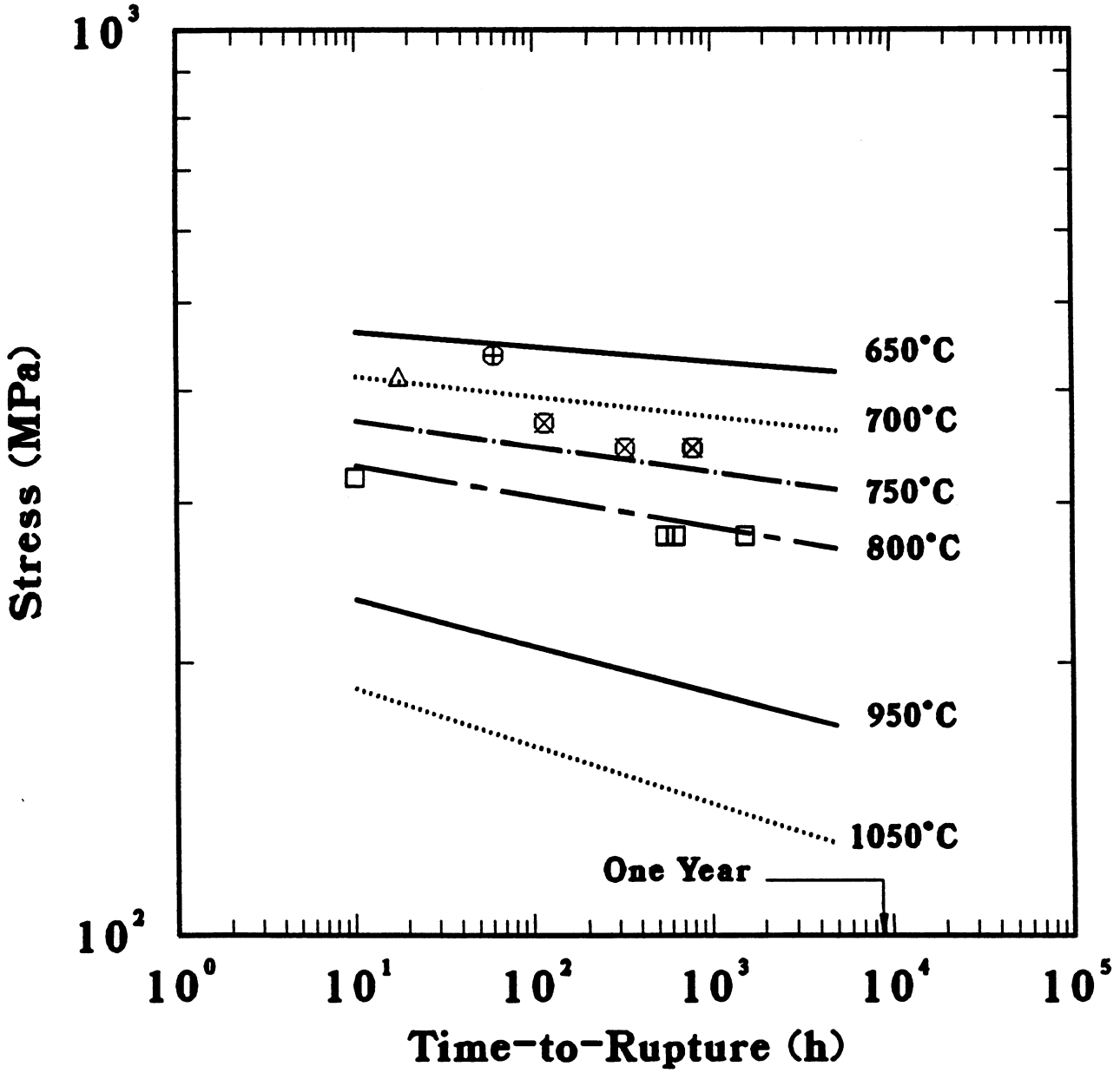

Figure 10.2-3. Creep-rupture stresses of V-15Cr-5Ti at various temperatures. Symbols are data points [11] and solid lines are estimates using MMCM [9].

of the lack of data on these high-temperature processes, the predicted high-temperature ($> 900\,°C$) creep behavior of V-3Ti-1Si is highly uncertain. Also, irradiation may enhance the thermal-creep component, but for lack of any data this enhancement is treated approximately, as is discussed in the following section.

10.2.1.3. Allowable design stresses

The design of structural components under high loads is based on specifications of the ASME Code Case 1592 for Class 1 Components in Elevated-Temperature Service [12]. Different allowable stresses for various stress classifications are assigned by specifying stress-intensity values for time-independent allowable stress (S_m), time-dependent allowable stress (S_t), or general primary membrane allowable stress (S_{mt}) which is taken as the lesser of S_m and S_t. The S_t is the lowest value of 2/3 of the minimum stress to cause rupture after time t, or 80% of minimum stress to cause tertiary creep after time t, or the minimum stress to produce 1% strain at time t. For the V-3Ti-1Si alloy, the creep-behavior data is too limited to base the maximum allowable stress on the 1% strain or on the tertiary-creep criteria. Therefore, the maximum allowable stresses in structural components made of V-3Ti-1Si was set at 2/3 of the minimum stress to cause rupture.

Because the creep-rupture analysis did not include any irradiation effects, an effort was made to allow for irradiation-induced loss of ductility (irradiation hardening and helium embrittlement) while establishing allowable design stresses. To incorporate these effects, a simple creep-rate equation of the form

$$\dot{\epsilon} \simeq K\,\sigma^n \tag{10.2-3}$$

was assumed. Here, $\dot{\epsilon}$ is the creep rate, K is a constant, σ is the applied stress, and n is the creep exponent. Using Equation 10.2-3, the irradiated and unirradiated creep behavior are related through

$$\frac{\epsilon_{irr}}{\epsilon} \simeq \left(\frac{\sigma_{irr}}{\sigma}\right)^n , \tag{10.2-4}$$

or solving for the stress of irradiated material, σ_{irr},

$$\sigma_{irr} \simeq \sigma \left(\frac{\epsilon_{irr}}{\epsilon}\right)^{1/n} . \tag{10.2-5}$$

Here, ϵ_{irr} and ϵ are the creep-rupture strain of irradiated and unirradiated material, respectively. Gold *et al.* [11] reported values for the creep exponent ranging from 2 to

Table 10.2-V.

ELONGATION OF THREE VANADIUM-BASE ALLOYS AS A FUNCTION OF HELIUM CONTENT AT 600 °C [13]

	Elongation (%)		
Helium (appm)	V-3Ti-1Si	V-15Cr-5Ti	VANSTAR-7
0	22	30	35
10	16	12	35
150	14	8	–
300	11	0	–
490	7	–	–

10 for V-3Ti-1Si alloys. For our estimates, a value of 4 is used for the creep exponent. This choice is based on experience with creep exponent values for other b.c.c structured alloys [9].

Braski [13] measured the total elongation of V-3Ti-1Si, V-15Cr-5Ti, and VANSTAR-7 as a function of implanted helium-atom content of up to 500 appm at 600 °C. Table 10.2-V shows the total elongation as a function of helium content for three vanadium-base alloys. The helium embrittlement behavior of V-3Ti-1Si was extrapolated beyond the available 500-appm data. Next, the helium embrittlement data of Table 10.2-V was used to approximate the ratio of ϵ_{irr}/ϵ as a function of helium content (or irradiation time). Equation 10.2-5 was then used to modify the unirradiated stress-to-rupture values calculated previously (Figure 10.2-3) as a function of time and temperature. Figure 10.2-4 shows the calculated creep-rupture stresses as a function of time using this approach.

By taking S_t to be 2/3 the minimum stress to cause creep rupture, the maximum allowable design stress was estimated. Table 10.2-VI shows the values of S_t at 650, 750, and 850 °C for the TITAN-I first wall. It should be emphasized that because of the lack of higher temperature data, the S_t values are all based on helium embrittlement data measured at 600 °C.

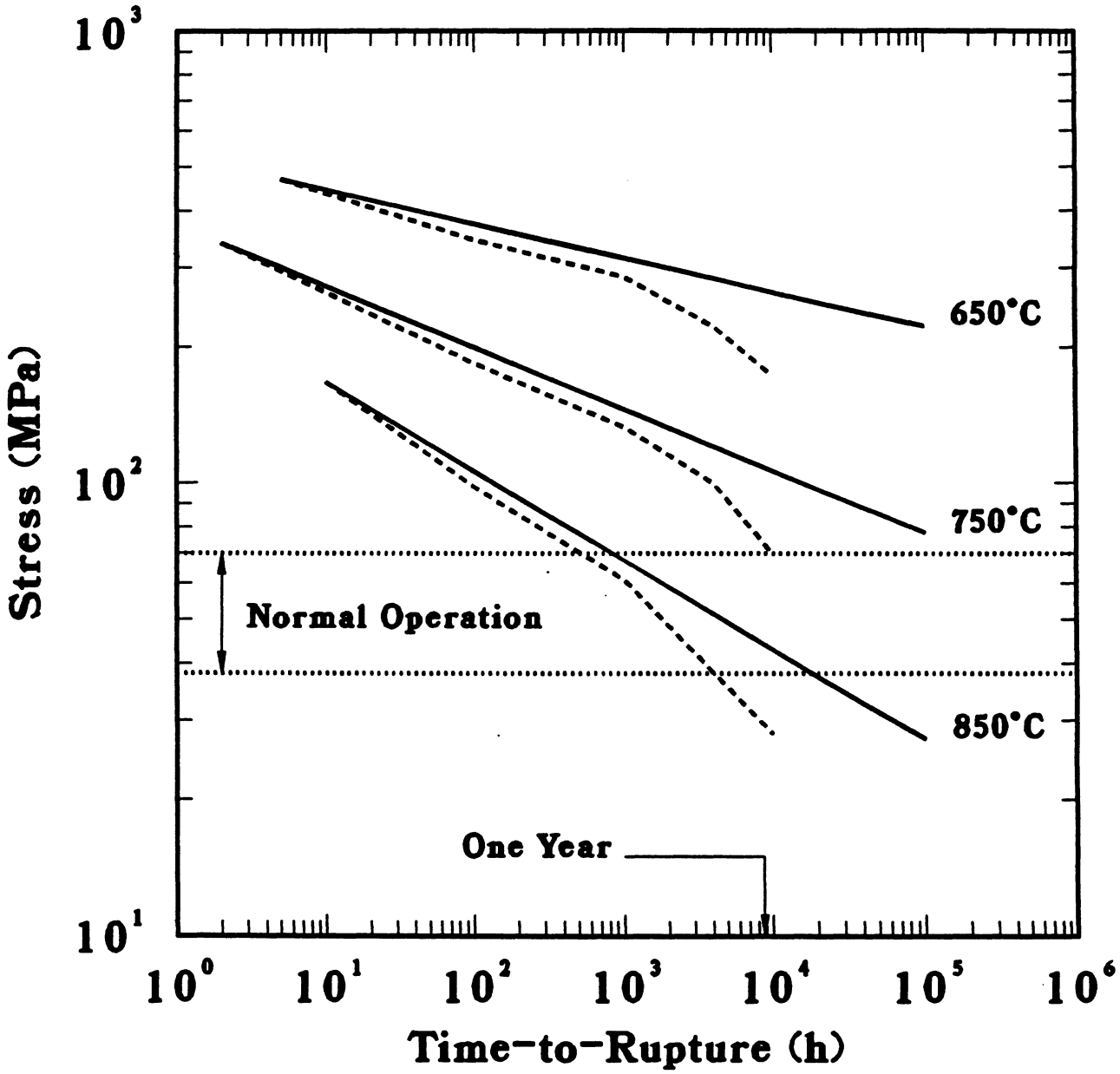

Figure 10.2-4. Creep-rupture stress curves for V-3Ti-1Si at various temperatures estimated by MMCM [9]. Solid lines represent the creep behavior of unirradiated and dashed lines that of irradiated V-3Ti-1Si alloy. Also shown is the expected stress range during the normal operation of the TITAN-I design.

Table 10.2-VI.

MAXIMUM ALLOWABLE DESIGN STRESSES FOR THE TITAN-I FIRST WALL[a]

T (°C)	σ (MPa)
650	115
750	47
850	19

(a) Based on 2/3 of irradiated creep-rupture stresses after one FPY of operation at 18 MW/m^2.

10.2.1.4. Lifetime analysis

Some of the issues associated with the lifetime of metallic structural materials in fusion reactors are: (1) the increase in ductile-to-brittle transition temperature (DBTT) with neutron damage, (2) irradiation-induced dimensional changes such as swelling and creep, (3) mechanical property changes such as tensile strength and toughness (irradiation hardening), and (4) helium and hydrogen embrittlement. A lifetime limit of about 200 dpa ($\sim$ 15 to 20 $MW\,y/m^2$) is generally quoted as the limit for most ferrous alloys. Because of the limited data on vanadium-base alloys, a limit of 15 to 18 $MW\,y/m^2$ was also used for the TITAN-I design (the parametric systems studies analysis of Section 3 has assumed the conservative value of 15 $MW\,y/m^2$ for the lifetime of the first wall). Analysis of the above lifetime-limiting processes are discussed in this section.

As discussed in the Section 10.2.1.1, the change in DBTT of vanadium-base alloys is expected to be negligible at high operating temperatures ($\geq$ 600 °C). This expectation is based on the operating experience with ferritic alloys, which have the same crystal structure (b.c.c.) as that of vanadium-base alloys. Swelling caused by helium production was also addressed in Section 10.2.1.1. Among the three candidate vanadium-base alloys, V-3Ti-1Si exhibits the lowest amount of swelling. A conservative estimate of the total swelling after one FPY at 18 MW/m^2 of neutron wall loading is $\sim$ 0.2%. Thus, neither a change in the DBTT nor irradiation-induced dimensional changes would limit the lifetime of the TITAN-I design below 15 to 18 $MW\,y/m^2$.

Neutron irradiation of metallic alloys can result in the formation and growth of new dislocation networks, resulting in an increased yield strength and decreased ductility (irradiation hardening). Figure 10.2-5 illustrates the irradiation hardening behavior of various metallic alloys. In general, V-20Ti, V-3Ti-1Si, and ferritic alloys exhibit radiation hardening below 500 °C. Above 500 °C, irradiation hardening anneals out and mechanical properties are no longer affected. Although irradiation data of V-3Ti-1Si is limited, irradiation hardening is not considered a major lifetime-limiting phenomena for this alloy, based on the TITAN-I high operating temperature and extensive experience with other b.c.c. ferrous alloys.

The effect of neutron-produced transmutations, mainly hydrogen and helium atoms, has also been addressed in Section 10.2.1.1. Three factors minimize the effects of hydrogen production in vanadium: (1) the high operating temperature ($\sim$ 700 °C) does not allow the formation of stable vanadium hydrides, (2) the diffusion of hydrogen through vanadium is rapid at these temperatures, resulting in low levels of dissolved-hydrogen concentrations, and (3) the maximum amount of hydrogen produced during one FPY is estimated between 5,000 to 6,000 appm, which is roughly the solubility limit of hydrogen in vanadium. Based on these observations, hydrogen production in the vanadium-base-alloy TITAN-I structural material is not considered a lifetime-limiting factor.

The most severe lifetime-limiting effect is believed to be caused by neutron-generated helium atoms inside the bulk material. Helium, unlike hydrogen, does not diffuse out to free surfaces. Helium atoms are trapped inside the matrix at trapping sites, such as dislocations, voids, and precipitates. As more and more helium is generated during operation, the helium bubbles grow and cause changes in the mechanical property of the material. The most pronounced effect is a degradation of ductility generally known as helium embrittlement. The amount of helium generated during operation in the TITAN-I first wall and the accompanying effects on material properties were discussed in detail in Sections 10.2.1.1 and 10.2.1.3. Helium generation on material performance was included in the creep analysis. Based on these calculations, the maximum operating temperatures and stresses were estimated for end-of-life operating conditions.

Because of the incomplete data base on vanadium-base alloys, a lifetime limit of 15 to 18 MW y/m^2 is used for the TITAN-I design, which is similar to the generally quoted value for most ferrous alloys. Analysis of the lifetime-limiting processes for the TITAN-I design indicates that this value is reasonable. However, it should be noted that many effects, particularly the synergism of radiation damage and helium production, can not be modeled because of the lack of data. Furthermore, a more rigorous lifetime analysis would include fatigue and thermal shock responses of the material. The limited data base on

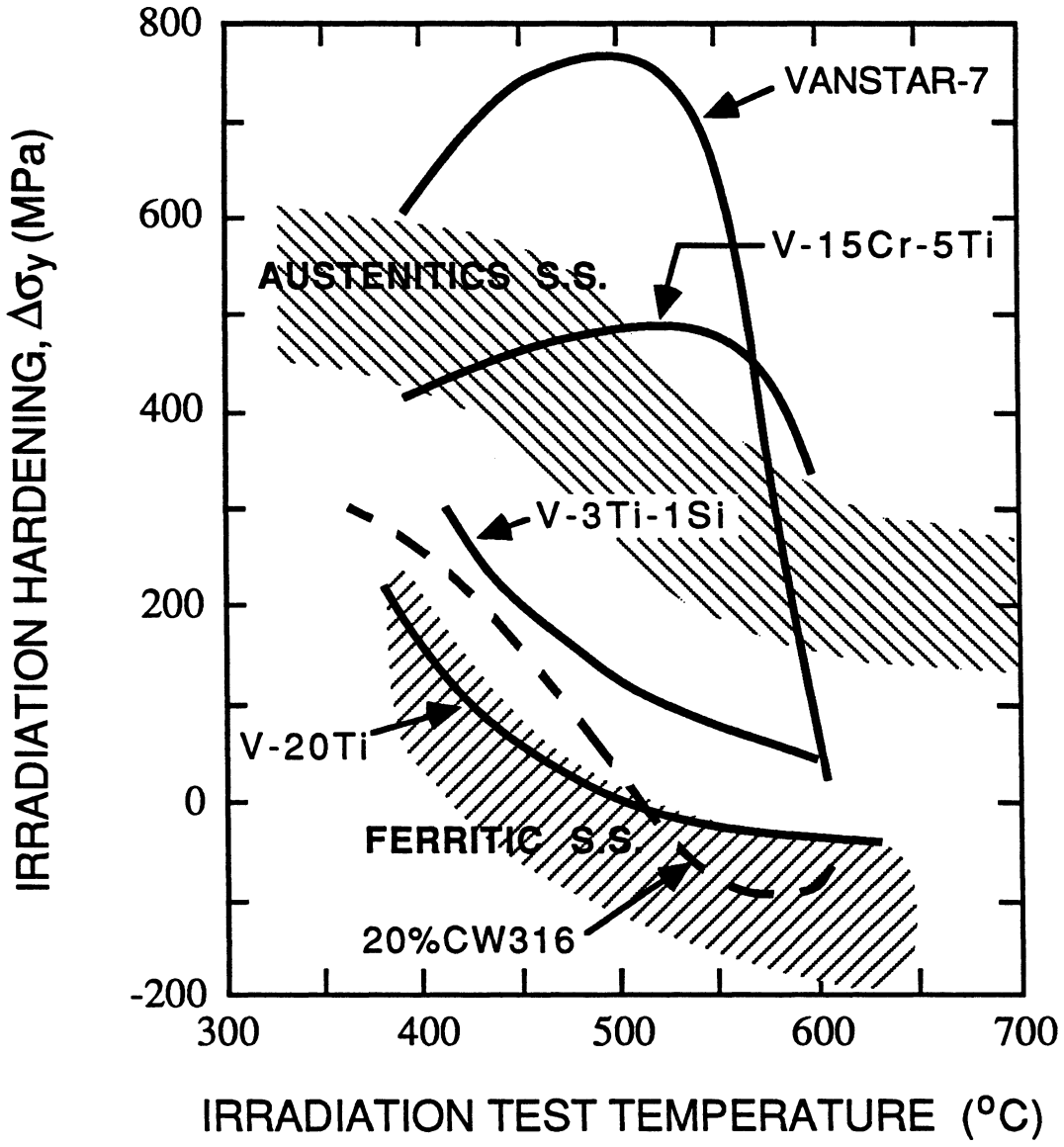

Figure 10.2-5. Irradiation hardening as a function of irradiation test temperature for vanadium alloys compared with similar data for austenitic and ferritic stainless steels [6].

vanadium-base alloys does not warrant such a more detailed analysis; more experimental data on vanadium-base alloys are needed.

10.2.2. Coolant Properties and Compatibility

The primary coolant of the TITAN-I FPC is liquid lithium. Liquid lithium, which also acts as the breeding material, has a low melting temperature, low density, and good thermal characterisitics. Physical properties of lithium are reviewed in Section 10.2.2.1. The compatibility of liquid lithium with the structural materials should be addressed, since an attack by the coolant may lead to unacceptable failure modes of the structure. Attack by pure liquid metals differs from that of other corrosives since there is usually no chemical reaction involved. The rate of attack depends primarily on the solubility of the solid metal in the liquid metal and the solution rate. Chemical reactions become important only when impurities such as oxygen, nitrogen, and carbon are present. In Section 10.2.2.2, these attack mechanisms are discussed to establish the degree of compatibility between liquid lithium and vanadium-base alloys, particularly V-3Ti-1Si. The impact of high velocity coolant is reviewed Section 10.2.2.3.

10.2.2.1. Lithium properties

As an alkali metal, lithium requires careful handling because of its reactivity with water and atmospheric constituents (*e.g.*, oxygen, nitrogen, hydrogen, and carbon dioxide). Because lithium will readily react with water to form gaseous hydrogen and heat, hydrogen explosions are one of the serious threats. Compared to sodium, however, lithium reacts much less vigorously with water [14]. Lithium also has a higher melting point, specific heat, and heat of fusion than sodium. Because of the experience of the fission industry with molten sodium (specifically in liquid-metal fast-breeder reactors), handling large amounts of liquid lithium should not pose a serious technological problem. Safety-related issues of lithium-cooled systems are discussed in Section 13.

The natural isotopic composition of lithium is 7.5% ^{6}Li and 92.5% ^{7}Li. The ^{6}Li enrichment process is classified at the present time. The ^{6}Li isotope is a U. S. government-controlled substance and only research quantities of about 5 to 10 g can be purchased at a time. The cost of ^{6}Li (95 to 96 at.%) is $\sim$ \$1,250 per kg; ^{7}Li (99.9 at.%) is $\sim$ \$500 per kg, while natural lithium costs $\sim$ \$30 per kg (1987 prices). The highest available enrichment of ^{6}Li is 95.2 at.% (94.82 wt.%). These figures were quoted by the Isotope Sales Office of the Oak Ridge National Laboratory (ORNL) [15]. As for the impurity

levels in lithium, the ORNL Isotope Sales Office has made chemical and spectroscopic analyses of batches of ^{6}Li and ^{7}Li. Typical impurity levels are given in Table 10.2-VII, and the chemical analysis results are shown in Table 10.2-VIII. All measurements were taken from lithium batches of April and May of 1987.

Lithium is used in many areas of medicine and electronics. Therefore, a nearly complete set of properties is available. Table 10.2-IX lists some of the physical properties of lithium. Among the interesting features of lithium is that it has about half the density of water and a boiling point of 1347 °C. The low density of lithium minimizes pumping power while the high boiling point makes low-pressure systems possible. The *Materials Handbook for Fusion Energy Systems* [14] reports many relevant properties in the form of plots and analytical equations. Table 10.2-X lists some of these correlations.

10.2.2.2. Lithium attack

Structural materials in contact with liquid metals can experience some form of attack which, depending on the severity, can lead to degradation of properties and ultimately to failure. The major types of liquid-metal attack are as follows:

- Simple solution,
- Liquid-metal penetration,
- Temperature-gradient mass transfer,
- Liquid-metal embrittlement,
- Dissimilar-metal mass transfer,
- Impurity reactions (oxygen, nitrogen, carbon, hydrogen).

Simple solution attack. In simple solution attack, solid metal dissolves in the liquid metal to the extent of its solubility. It can result in uniform thinning of the material or cause intergranular penetration if a single constituent is preferentially leached from the solid. During the late 1950s and early 1960s, forced-circulation-loop tests with vanadium and liquid lithium were conducted as part of the space-power program [16]. Tests were run with unalloyed vanadium for up to 1170 hours. The lithium flow velocity was 4 m/s with a maximum temperature of 870 °C. Reported corrosion rates for vanadium were *nil.* The BCSS [2] interpreted the reported value as $\sim 0.1\,\mu$m/y, based on a reported

Table 10.2-VII.

IMPURITY LEVELS (appm)[(a)] IN ^{7}Li (99.98 at.%) AND ^{6}Li (95.2 at.%)

Metal	Symbol	^{7}Li	^{6}Li	Metal	Symbol	^{7}Li	^{6}Li
Silver	Ag	1	1	Niobium	Nb	10	10
Aluminum	Al	10	10	Nickel	Ni	10	10
Arsenic	As	40	40	Lead	Pb	4	4
Gold	Au	4	4	Palladium	Pd	10	10
Barium	Ba	10	10	Rubidium	Rb	40	40
Cadmium	Cd	6	6	Rhodium	Rh	20	20
Cobalt	Co	20	20	Ruthenium	Ru	40	40
Chromium	Cr	1	1	Antimony	Sb	20	20
Cesium	Cs	40	40	Silicon	Si	20	20
Copper	Cu	20	50	Tin	Sn	20	20
Iron	Fe	20	20	Strontium	Sr	10	10
Gallium	Ga	10	10	Tantalum	Ta	40	40
Germanium	Ge	10	10	Thorium	Th	100	100
Hafnium	Hf	10	10	Titanium	Ti	10	10
Indium	In	40	40	Thallium	Tl	10	10
Iridium	Ir	60	60	Thulium	Tm	4	4
Lutetium	Lu	4	4	Vanadium	V	10	10
Magnesium	Mg	30	100	Tungsten	W	100	100
Manganese	Mn	1	1	Yttrium	Y	6	6
Molybdenum	Mo	4	4	Zirconium	Zr	10	10

(*a*) Maximum levels from spectroscopic analysis [15].

Table 10.2-VIII.

NONMETALLIC IMPURITY LEVELS[a] IN ^{7}Li AND ^{6}Li

Substance	^{7}Li	^{6}Li
Calcium (appm)	67	167
Potassium (appm)	< 40	< 50
Sodium (appm)	88	49
Nitrogen (appm)	174	1561
Carbon (appm)	–	645
Chlorine (wt.%)	0.004	0.002
Heavy metals (wt.%)	0.01	0.018

(*a*) Chemical analysis results [15].

minimum corrosion rates of other alloys [2]. Capsule tests conducted at ORNL [17] and forced-circulation tests at Argonne National Laboratory [18] later confirmed the corrosion resistance of vanadium-base alloys to liquid lithium. Although the solubility of vanadium in lithium was not reported, these results indicate negligible vanadium solubility.

Liquid-metal penetration. The presence of impurities such as oxygen, carbon, and nitrogen in solid metals has been found to influence the compatibility of alloys with liquid alkali metals [19]. Liquid-metal penetration (LMP) has been observed to occur when the solid metal contains more than a certain threshold impurity concentration [19 - 21]. Rapid penetration along grain boundaries can occur. While vanadium was found not to be susceptible to LMP, a 1-mm specimen of tantalum containing 600 appm of oxygen was completely penetrated by lithium after exposure for 0.5 h at 600 °C [21]. This penetration phenomenon has been found in a number of refractory metals exposed to lithium, sodium, potassium, and the sodium-potassium eutectic, NaK [21 - 23].

While in refractory metals the oxygen concentration affects the LMP, in iron the carbon concentration is the most important factor. Iron containing small amounts of

Table 10.2-IX.

PHYSICAL PROPERTIES OF LITHIUM [2,14]

Atomic weight	6.94	
Density (room temperature)	530	kg/m^3
Melting temperature	180.5	°C
Boiling temperature	1347	°C
Heat of fusion	432	kJ/kg
Heat of vaporization	19,595	kJ/kg
Heat capacity		
at 350 °C	4.24	kJ/kg-K
at 500 °C	4.17	kJ/kg-K
at 650 °C	4.16	kJ/kg-K
Thermal conductivity		
at 350 °C	46.8	W/m-K
at 500 °C	49.6	W/m-K
at 650 °C	52.4	W/m-K
Surface tension		
at 350 °C	0.373	N m
at 500 °C	0.350	N m
at 650 °C	0.325	N m
Electrical resistivity		
at 350 °C	0.311	$\mu\Omega$ m
at 500 °C	0.353	$\mu\Omega$ m
at 650 °C	0.395	$\mu\Omega$ m
Viscosity		
at 350 °C	0.41	cP
at 500 °C	0.32	cP
at 650 °C	0.27	cP

Table 10.2-X.

ANALYTICAL EQUATIONS FOR SELECTED Li PROPERTIES [14]

Property	Temperature Range	Expression
Specific heat (kJ/kg-K)	$453 < T < 692\,\mathrm{K}$	$c_P = 4.3014 - 8.382 \times 10^{-4} T$
	$693 < T < 1173\,\mathrm{K}$	$c_P = 4.1876 - 7.330 \times 10^{-5} T$
Enthalpy (MJ/kg)	$463 < T < 923\,\mathrm{K}$	$H_T = 1.1321 + c_P(T - 453.6)$
	$923 < T < 1573\,\mathrm{K}$	$H_T = 1.1227 + 4.19 \times 10^{-3} T$ $-21.66/(T + 273)$
Electrical resistivity ($\mu\Omega\,\mathrm{m}$)	$473 < T < 1673\,\mathrm{K}$	$\rho = 0.1575 + 2.197 \times 10^{-4} T$ $+6.253 \times 10^{-8}\ T^2$ $-2.504 \times 10^{-11} T^3$
Viscosity (cP)	$473 < T < 973\,\mathrm{K}$	$\log \eta = 1.4936 + 109.95/T$ $-0.7368 \log T$
	$973 < T < 1473\,\mathrm{K}$	$\log \eta = 726.07/T - 1.338$
Density (kg/m^3)	$473 < T < 1873\,\mathrm{K}$	$d = 504.6 - 0.101T$
Thermal conductivity (W/m-K)	$473 < T < 1373\,\mathrm{K}$	$k = 34.907 + 0.0191T$
Vapor pressure (atm)	$700 < T < 2000\,\mathrm{K}$	$\log P = 4.8831 - 7877.9/T$
Surface tension (dyn cm)	$473 < T < 1673\,\mathrm{K}$	$\gamma = 0.16(3550 - T) - 95$

carbon was penetrated intergranularly by lithium [24 - 26]. The cause of corrosion was attributed to the reaction of lithium with the carbon in the grain boundaries. Corrosion-resistant niobium and tantalum alloys have been developed through the addition of minor amounts of reactive metals such as Zr and Hf. However, conflicting results are reported in the literature regarding the susceptibility of metals to LMP [24,27,28]. Not only are the mechanisms of the penetration not clear yet, but irradiation is expected to complicate this phenomena further. Fusion reactors that use liquid metals as coolant invariably have a large coolant-structure surface area and, thus, are susceptible to LMP. In conjunction with corrosion, transgranular penetration of vanadium-base alloys by liquid lithium has been investigated during the capsule tests performed at ORNL [17]. It was found that, unlike niobium and tantalum, vanadium did not suffer from any severe penetration rate regardless of whether oxygen was present or not [2].

Temperature-gradient mass transfer. The low solubility of structural materials in the coolants makes simple solution of most metals negligible. However, when a temperature gradient exists, such as in a coolant loop, the solid metal approaches saturation in the hotter zone only to crystallize out in the cooler regions because of the decrease in solubility. This effect sets up temperature-gradient mass-transfer mechanism that can ultimately result in tube plugging in the cold leg of a coolant loop.

Accumulation of deposits in heat exchangers can adversely affect their hydraulic performance by reducing the flow area. Furthermore, the heat-transfer resistance can increase because of the inferior thermal conductivity of the deposited scale compared to that of the base metal. An annual reduction of nearly 10% in the overall heat-transfer coefficient of the intermediate heat exchanger (IHX) is estimated from loop-corrosion data in sodium-stainless-steel systems of liquid-metal breeder reactors [29].

Radioactive constituents can become immobilized in the corrosion products and be deposited on the cooler surfaces of the loop, such as the IHX. This can lead to radioactivity levels sufficiently high to impair routine maintenance of components in the cold leg of a primary loop. The fission industry has, therefore, introduced a maximum mass-transfer limit range for sodium-steel systems of 5 to 20 μm/y corresponding to flow restriction and 0.5 μm/y for the radioactive mass transport. Applying these limits to liquid-lithium-cooled vanadium-base alloys may be overly conservative, and detailed investigation is required to establish similar guidelines for fusion applications.

Because of the low corrosion rates of vanadium-base alloys ($< 0.1\ \mu$m/y at 860 °C [16]), the transport of structural material from high-temperature regions and consequent deposition at the cold leg of the primary loop does not seem to be a major concern, even

by fission-industry guidelines. However, an additional complication may arise from the presence of strongly varying magnetic fields which can impact the deposition of ferromagnetic substances. Such an effect has not yet been analyzed in sufficient detail to be incorporated in the fusion reactor studies.

Liquid-metal embrittlement. Liquid-metal embrittlement is caused by a reduction in bond strength of the atoms in a solid by chemisorption of a liquid atom at the tip of a crack or at the end of a pileup of dislocations near a surface obstacle. Attachment of an impurity atom reduces the stress required for cleavage. Thus, normally ductile materials may fail in a brittle manner by cleavage or by rapid intergranular crack propagation [30]. Ammon [19] reported that vanadium-base alloys are not susceptible to liquid-metal embrittlement by lithium.

Dissimilar-metal mass transfer. Since vanadium is an expensive material, it would be advantageous to use steels as the structural material of the primary-loop piping outside the FPC where the structural material is not subjected to extreme radiation and heat loads. When dissimilar metals are in contact with the same liquid metal, one of the metals may be transferred through the liquid metal to alloy with the other metal. Removal of the soluble metal from solution by this method ensures that saturation is never attained. This can lead to unacceptably high levels of corrosion even when the solubility of a metal in the liquid metal is very low. An example of this rapid attack is the rapid dissolution of SS-304 stainless steel by molten lithium in an iron container [31,32]. However, vanadium-steel bimetallic-loop tests have not reported a dissimilar-metal transfer problem [33,34].

Impurity reactions. Another effect of having dissimilar metals in contact with the same liquid metal is the transfer of nonmetallic constituents between the two alloys. This process is generally referred to as the bimetallic impurity pickup, which is believed to be a major concern in systems that use vanadium-base alloys as the primary structural material, and a ferrous alloy for the remainder of the loop. Steels may contain large amounts of nonmetallic additions such as carbon, nitrogen, and oxygen. These additions reside in steel, mostly in the form of interstitials, each with characteristic diffusion coefficients. The formation of lithium compounds (*e.g.,* Li_3N, Li_2C_2, Li_2O) can effectively leach these nonmetallic elements from the steel. Since carbides and nitrides of vanadium are thermodynamically more stable than those of lithium, the lithium will give up the carbon and nitrogen leached from the steel to the vanadium-base alloy. The lithium

oxide, Li_2O, is more stable than the oxides of vanadium at all temperatures, therefore transfer of oxygen from the steel to the vanadium does not occur.

To explain impurity reactions, DeVan and Klueh [35] have conducted an extensive analysis of the thermodynamics of interstitial interactions with a number of refractory-metal and lithium systems. The impurity reactions were analyzed in terms of equilibrium distribution coefficients, which are the ratio of the impurity-element concentrations in the solid metal to those in the liquid metal as a function of temperature. Distribution coefficients less than unity result in a tendency for interstitials to be transferred from the solid to the liquid metal, causing a reduction in strength of the alloy. Distribution coefficients larger than unity indicate a net transfer of impurities from the liquid to the solid, which may lead to embrittlement of the metal. For a vanadium-lithium system, the distribution coefficients of nitrogen and carbon are well above unity for the temperature range of interest (500-1200 °C), while the distribution coefficient of oxygen and hydrogen is below unity.

Oxygen. Because in a vanadium-lithium system the oxygen equilibrium distribution coefficient is much less than unity ($< 10^{-4}$), oxygen will be lost to lithium. Oxygen added as a solution hardener to a vanadium-base alloy could be depleted by liquid lithium, leading to a reduction of strength. The rate of loss of oxygen would depend primarily on the temperature gradient across the metal. Investigation by Schmidt and Warner [36] and Powers and Doyle [37] show that the diffusion coefficient of oxygen in vanadium, D_O^V (cm^2/s), can be estimated by the following equation:

$$D_O^V = (0.0246 \pm 0.0031) \exp\left(-\frac{29,495 \pm 110}{RT}\right), \qquad (10.2\text{-}6)$$

where R is the gas constant (1.986 cal/K mol) and T is temperature (K).

In contrast to the vanadium-lithium system, the oxygen equilibrium distribution coefficient of a sodium-steel system is greater than unity; oxygen will be picked up from sodium by steel, leading to the formation of soluble iron oxides.

Nitrogen. Nitrogen has a distribution coefficient above unity and, therefore, will be picked up by vanadium from liquid lithium. The nitrogen-pickup rate is determined by various factors such as solubility, vanadium-nitrogen phase reaction, surface layer, and temperature. The solubility limits of nitrogen in vanadium are well known and are given in Table 10.2-XI. The diffusion coefficient of nitrogen in vanadium, D_N^V (cm^2/s), was reported by Schmidt and Warner [36] as follows:

$$D_N^V = (0.0417 \pm 0.0034) \exp\left(-\frac{35,459 \pm 111}{RT}\right). \qquad (10.2\text{-}7)$$

Table 10.2-XI.

SOLUBILITY EQUATIONS FOR VANADIUM-NITROGEN SYSTEM [19]

Solid Solubility Limit (at.%)	Temperature Range (K)
$C_N = 50.0\ \exp(-5,500/RT)$	$548 < T < 848$
$C_N = 33.0\ \exp(-3,700/RT)$	$873 < T < 1473$
$C_N = 31.5\ \exp(-3,800/RT)$	$773 < T < 1773$

Experiments performed by Gulbransen and Andrews [38] showed that the rate of weight gain of vanadium exposed to nitrogen gas between 600 and 900 °C was insensitive to the nitrogen pressure. This indicates the formation of a nitride layer on the surface. An activation energy of 31.4 kcal/mol for the formation of vanadium nitride and a migration energy of 35.5 kcal/mol for nitrogen through vanadium was reported. The small difference between the nitride-formation and nitrogen-migration energies indicates a preference to form a nitride layer rather than simple diffusion of nitrogen through vanadium. The rate of weight gain was found to follow a parabolic behavior [38] which is indicative of a saturation process. Saturation of the surface layer with nitrogen can lead to the formation of a barrier and consequently a reduction of nitrogen pickup. Subsequent investigators [39] confirmed these findings and reported the formation of V_3N and VN. Above 800 °C, the parabolic behavior of the rate of weight gain was also observed.

Recently Adelhelm *et al.* [33] studied the corrosion behavior of the vanadium-base alloy V-3Ti-1Si in a pumped lithium-stainless-steel loop at 533 to 550 °C for up to 2056 hours. They measured the nitrogen and carbon pickup of V-3Ti-1Si as a function of time. The nitrogen uptake was correlated to a parabolic pickup behavior as

$$C_N^{up} = 0.024 + 2.2 \times 10^{-3}\, t^{0.59}, \tag{10.2-8}$$

where C_N^{up} is the nitrogen uptake in wt.% and t is the exposure time in hours. Metallographic investigations revealed a very thin (2-5 μm), dark-gray layer in exposed coupons of V-3Ti-1Si specimen which had undergone a marked titanium enrichment and a strong vanadium loss. Across this dense surface layer, the titanium concentration increased from $\sim$ 3 to 11 wt.% and the vanadium concentration decreased from $\sim$ 90 to $\sim$ 75 wt.%.

The layer was identified as a vanadium-titanium-nitride compound, $(V,Ti)_xN$, with a stoichiometric parameter, x, between 1.55 and 1.67. An interesting observation was that the maximum impurity reactions were measured at an intermediate time and not after the longest exposure time.

This unusual behavior was easily explained by examining the nitrogen content of the lithium. It had been reported earlier by Olson *et al.* [40] that the nitrogen content of the liquid lithium influences the corrosion rates in lithium-stainless-steel systems. For the V-3Ti-1Si-lithium system, Adelhelm *et al.* [33] found that the lowest corrosion rate occurred for a nitrogen concentration of 30 wppm during the 2056-hour test and not for those tests with nitrogen concentrations of 8 wppm for 362 hours or 64 wppm for 1073 hours. This observation indicates that a protective nitride layer forms at an optimum nitrogen concentration of about 30 wppm. Furthermore, examination of the nitride layers at these three different nitrogen concentrations reveals that the nitrogen content influenced both the thickness and the degree of porosity of the layer. At a nitrogen content of 8 wppm, the layer showed the highest degree of porosity, while at 30 wppm the layer had the highest density. The very compact layer without any porosity at high nitrogen content, therefore, acts as a good corrosion-resistant protection barrier. The measured corrosion rates for the V-3Ti-1Si-lithium loop ranged between 10^{-3} and 10^{-2} g/m^2 h (or 1.5-15 μm/y) depending on the nitrogen content, with the highest corrosion rate at the lowest nitrogen content of 8 wppm.

Structural identification of the nitride layer was not performed by Adelhelm *et al.* [33]. However, Verkhogllyadova *et al.* [39] identified hexagonal cubic-packed (h.c.p.) V_3N and face-centered cubic (f.c.c.) VN phases in experiments with vanadium exposed to nitrogen gas at 101.3 kPa for up to 4 hours in the temperature range of 500 to 1500 °C. In general, radiation-damage resistance of h.c.p. structured materials is not as good as that of f.c.c. structures because of the geometric anisotropy in h.c.p. crystals (crystal is longer in one direction, leading to anisotropic dimensional changes). Therefore, in an intense radiation environment, as expected in the first wall of a fusion device, the structural integrity of the protective layer is questionable. However, since the layer forms during operation, a "self-healing" mechanism would be repairing the damaged nitride layers continuously.

The corrosion behavior of vanadium alloys in flowing lithium as a function of nitrogen content was also investigated by Chopra *et al.* [34]. Vanadium-alloy specimens were exposed to lithium at 427, 482, and 528 °C. Lithium was circulated at 1 lit/min with runs of 1500 to 2500 hours. The dissolution rates of the various vanadium alloys exposed to lithium at 482 °C decreased in the following order: pure V, V-3Ti-1Si, V-5Ti-(12 to 15Cr), V-(10 to 15Cr)-3Fe-1Zr, and V-(15 to 20Ti)-7.5Cr. They reported

that only the alloys containing 15 to 20 Ti developed a protective nitride scale. Contrary to Adelhelm's findings, the nitrogen pickup rate reported by Chopra *et al.* did not show a parabolic behavior. The effect of carbon on the dissolution rate of vanadium alloys was also investigated by Chopra *et al.* [34]. All vanadium alloys picked up carbon and nitrogen and lost oxygen in lithium. They concluded that concentrations of 20 to 50-wppm nitrogen and 8 to 12-wppm carbon in lithium are above acceptable limits for vanadium-alloy-lithium systems. Table 10.2-VIII lists typical nitrogen contents of ^{6}Li and ^{7}Li. These nitrogen contents are well above the levels used in the Adelhelm and Chopra experiments.

The above discussion indicates that the behavior of vanadium-base alloys in liquid lithium depends strongly on the chemistry of the lithium. Variations in the amount of the dissolved nitrogen can affect the formation rate and stability of the vanadium-nitride layer. Therefore, control of liquid-lithium chemistry is crucial for bimetallic loops. More experimental data on this subject are required.

Carbon. The solubility of carbon in vanadium appears to be very low at temperatures less than 1200 °C, based on the phase diagram for the vanadium-carbon system [41]. However, the equilibrium distribution coefficient of carbon between lithium and vanadium is about 10^4 at 800 °C and increases to 10^8 at 400 °C [5]. This large distribution coefficient indicates that carbon is readily absorbed from liquid lithium by vanadium. Thus, carbon pickup will always be an issue when vanadium is used as a structural material. The diffusion of carbon in vanadium, D_C^V (cm^2/s), has been reported [36] as

$$D_C^V = (0.0088 \pm 0.0018) \exp\left(-\frac{27,792 \pm 180}{RT}\right) . \qquad (10.2\text{-}9)$$

Adelhelm *et al.* [33] measured the carbon uptake of V-3Ti-1Si exposed to liquid lithium at 550 °C containing a few wppm of carbon. Carbon contents were calculated based on solubility data and also the data from titanium gettering. While the nitrogen concentration in vanadium was found to have increased by a factor of 10, the carbon concentration only increased by a factor of 1.5. The carbon uptake showed a linear relationship for both the hot (550 °C) and cold (533 °C) legs of the test loops. The estimated pickup rates were given as:

$$c_c = 0.0424 + 7.31 \times 10^{-6} t , \qquad (10.2\text{-}10)$$

for the hot leg, and

$$c_c = 0.0428 + 6.64 \times 10^{-6} t , \qquad (10.2\text{-}11)$$

for the cold leg, where c_c is the carbon concentration of the vanadium foils (in wt.%), and t is the exposure time in hours. The low carbon pickup rate results from either: (1) a $(V,Ti)_xN$ layer formed and served as a physical barrier to carbon, or (2) the use of austenitic stabilized steel minimized the supply of carbon.

Hydrogen. The vanadium-hydrogen (V-H) system has been studied to some extent in recent years. Veleckis and Edwards [42] investigated the range of 246 to 554 °C and developed a semiempirical equation for the P-C-T isotherms of a high purity vanadium-hydrogen system:

$$\sqrt{P} = K \frac{r}{s-r} \exp\left(\frac{1}{RT}\sum_{i=0}^{4} A_i r^i\right) , \qquad (10.2\text{-}12)$$

where P is the hydrogen pressure in atmospheres, r is the hydrogen-metal atom ratio, and K, s, and A_i are parameters given in Table 10.2-XII. Measurements of the solubility of H_2 and D_2 in vanadium over the temperature range 400 to 800 °C by Mareche *et al.* [43] agree with those reported by Veleckis and Edwards [42]. Mareche *et al.* also reported no isotope effect for D_2 in vanadium. Thus D_2 and H_2 exhibit the same solubility as a function of pressure and temperature.

The diffusion coefficients of hydrogen (D_H^V) and deuterium (D_D^V) were measured over the temperature range of 110 to 930 °C by Cantelli *et al.* [44] and found to be

$$D_H^V = (4.4 \pm 1.5) \exp\left(-\frac{0.059 \pm 0.007}{kT}\right) , \qquad (10.2\text{-}13)$$

$$D_D^V = (3.1 \pm 0.8) \exp\left(-\frac{0.073 \pm 0.006}{kT}\right) , \qquad (10.2\text{-}14)$$

where D_H^V and D_D^V are in cm^2/s and k is the Boltzmann constant.

Hydrogen embrittlement is one of many forms of hydrogen attack on a metals. In general, refractory metals are embrittled by hydrogen, primarily by hydride-phase formation. However, vanadium, niobium, tantalum, and their alloys do not form stable hydrides, unlike titanium and zirconium which suffer severe hydrogen embrittlement [45]. Loomis *et al.* [4] report that the maximum solubility level of hydrogen in vanadium alloys is about 5000 appm. Once the hydrogen content exceeds terminal solid solubility, damage may proceed by hydride-precipitate formation. Three sources of hydrogen in the first-wall structure are possible: (1) neutron reactions with vanadium, (2) plasma-driven permeation, and (3) tritium in the liquid lithium. The latter source of hydrogen (from lithium) is not a concern, since the equilibrium distribution coefficient of hydrogen between vanadium and lithium is well below unity ($\sim 10^{-2}$ to 10^{-3} for a temperature range

Table 10.2-XII.

PARAMETERS OF EQUATION 10.2-12 [42]

Parameter	Value
K	801
s	0.779
A_o	-6.93×10^3
A_1	-6.50×10^3
A_2	5.09×10^3
A_3	-1.51×10^3
A_4	-9.57×10^3

of 900 to 400 °C). The formation of lithium hydride, therefore, is preferential over the formation of vanadium hydrides. Experiments [45] have also shown that in vanadium alloys containing 5 to 20 Ti, ductility is restored to values of uncharged samples when the temperature is raised above 250 °C. Therefore, hydrogen embrittlement of vanadium through hydride formation is believed not to be a problem at TITAN-I operating temperatures.

10.2.2.3. Effects of high-velocity coolant

In the TITAN-I design, the liquid-lithium coolant flows at a high velocity of 21 m/s in the first-wall channels. The effects of velocity on corrosion rates are complex and depend on the characteristics of the metal and the environment. Velocity affects corrosion through two distinct mechanisms: (1) agitation of reaction constituents can increase reaction rates, and (2) the increased momentum of fluid particles can lead to an increase in wear (*i.e.*, erosion). Increased reaction rates are generally found in aqueous solutions, where the concentration of cations and anions play a large role in corrosion rates. In general, liquid metals do not interact chemically with solid surfaces and, therefore, the

effects of velocity on corrosion rates of vanadium alloys in a liquid-lithium environment fall mostly into the second category.

Wear by erosion can be caused by intense pressure or shock waves traveling in the fluid. Constant impingement of high-velocity particles on metallic surfaces gradually leads to strain hardening of the material. Strain-hardened surfaces are less ductile than the base material. This situation can result in the formation of micro-cracks in the surface layer when the metal is exposed to varying stresses during operation. Rapid flow of the coolant can also cause erosive shear of the surface. When maximum surface elongation has been attained, transgranular micro-cracks occur. After formation, micro-cracks may grow and propagate, resulting in an overall loss of surface strength and consequent removal by the flowing medium.

The surface strain-hardening rate is determined by an erosion "incubation time" which tends to become longer with increasing base-metal hardness. Surface treatment, such as sulfur-nitriding, leads to hardening of the metal surfaces and improves erosion resistivity by "interesting" proportions [46]. The presence of nitrogen in liquid lithium can result in the formation of a complex vanadium-titanium-nitride layer in V-3Ti-1Si, as discussed before. This formation will result in an increased surface hardness which is beneficial for erosion resistance.

A literature search regarding erosion by liquid lithium showed that this issue has not been investigated in any detail, specifically for vanadium alloys. Most of the research regarding erosion deals with water-steel systems, particularly distinguishing between particle-free or particle-containing water or slurry. Some of the findings regarding the effects of velocity of a water-metal system can be applied to many other fluid-metal systems [46 - 51]. These findings are summarized below.

Wear as a function of time. For long periods of exposure, the weight of a metal worn away is approximately a linear function of time. Velocity is an essential parameter as is the angle of impact of the fluid against the wall. For ordinary E-26/2 steel ($\sim 0.20\%$ C) at room temperature, erosion after a time t (in hours) may be expressed as follows:

$$e_m = 9 \times 10^{-13} v^5 \sin^2 \alpha \,, \qquad (10.2\text{-}15)$$

where e_m is the erosion depth in mm, v is the fluid velocity in m/s, and α is the impact angle. For example, if $v = 40\,\mathrm{m/s}$ and the average impact angle is about 10°, then the erosion rate would be about 0.02 mm/y.

Equation 10.2-15 is specifically measured for the E-26/2 steel exposed to room-temperature water. Experiments with steels containing 0.3% to 25% chromium or between 0.3% and 80% cobalt resulted in a much lower erosion rate given by:

$$e_m = \frac{2 \times 10^{-13} v^5 \sin^2 \alpha}{(Cr + Co)}, \qquad (10.2\text{-}16)$$

where Cr and Co are, respectively, the chromium and cobalt content in the steel in percent. Equation 10.2-16 shows that the addition of chromium and cobalt has not changed the dependence of the erosion rate on the velocity or the impact angle, but rather has led to a drastic reduction in the coefficient of the erosion rate. Under the same conditions of $v = 40\,\text{m/s}$ and a 10° impact angle, the erosion rate is now only about 0.007 mm/y for steels containing 0.3% Cr and 0.3% Co, versus 0.2 mm/y for the E-26/2 steel.

Threshold velocity for erosion. Equations 10.2-15 and 10.2-16 show that the erosion rate strongly depends on the fluid velocity. However, for most materials a threshold velocity exists, below which no measurable erosion rate is detected. This threshold velocity depends mostly on the strength (hardness) of the material in contact with the liquid. Threshold velocities are determined experimentally by performing jet-impact experiments where the sample is subjected to the impact of a high-velocity water jet for varying periods of time and impact angles. Threshold velocities are generally quoted for impact angles of 90° (perpendicular impact). For steels containing 12% chromium, the threshold velocity has been measured to be between 100 and 120 m/s. Because of high threshold velocities, the loss of weight for tangential flow (coolant flowing parallel to the material) can be negligible compared to perpendicular coolant impact. Experiments show that the ratio between tangential and perpendicular erosion rates is about 10^{-4}. This ratio was determined by examining the erosion rate on two different locations along a tube with a 90° bend. To reduce the effects of high-velocity fluids, therefore, sudden changes in flow patterns caused by sharp bends or extraction-contractions should be avoided.

Erosion of hard surfaces. Exposure of vanadium alloys to liquid lithium invariably results in hardening of the surface because of interstitial pickup by the vanadium alloy. These impurities form carbides and nitrides which produce a ceramic-type surface layer in contact with the fluid [33]. Therefore, it is necessary to investigate the effects of high-velocity fluids on erosion of brittle materials. Researchers have been concerned with

Table 10.2-XIII.

THRESHOLD VELOCITIES OF SEVERAL BRITTLE MATERIALS [50]

Material	Velocity[(a)] (m/s)
Zinc sulfide	125
Soda-lime glass	150
Germanium	150
Sapphire	350
Silicon nitride	500

(*a*) Minimum velocity of a 0.8-mm jet to cause fracture in the sample.

a range of infrared-transmitting materials (*e.g.*, zinc-sulfide, germanium, sapphire) and other ceramics such as Al_2O_3 and soda-lime-silicate glass. Results of erosion-corrosion threshold velocities with 90° jet-impact experiments of several brittle materials are given in Table 10.2-XIII. These threshold velocities reflect the minimum velocity of a jet to cause stress fractures. It is assumed that after fracture the material becomes highly susceptible to erosion by the high-velocity fluid.

These findings suggest that relatively thin coatings of micron thickness and high modulus of elasticity could be beneficial in protecting substrate solids from damage by high-velocity fluid impact. Thin coatings can lead to a sizeable reduction of substrate stresses and hard coatings improve the threshold conditions for damage. Ball-indentation experiments on carbon-coated germanium have shown that a coating of 1 to 3 mm can increase the critical load for ring-crack formation by as much as 100% to 200%, respectively. To investigate the effect of temperature on the velocity threshold for erosion of brittle material, Hockey *et al.* [51] have investigated the erosion rate of Al_2O_3 and soda-lime-silicate glass as a function of temperature between 25 and 1000 °C, using SiC particles of 3 to 5 mm and 30 mm in size. Particle velocities up to 125 m/s and impact angles ranging from 15° to 90° were used. It was concluded that temperature has little effect on the erosion rates of silicon nitride, polycrystalline aluminum oxide, and soda-lime-silicate glass.

In addition to the use of coatings, surface modification by ion implantation of titanium, zirconium, or yttrium has proven to be highly beneficial against erosion. For example, abrasion by fast-moving hard particles (sand particles in fuel oil) was reduced by a factor of 10 after titanium was implanted into the steel surface. A similar effect could be present in V-3Ti-1Si in which the Ti close to the surface may act as such a hardener.

Using the results of water-steel jet-impact experiments, the effects of high-velocity fluids on the erosion rate of metallic materials can be summarized as follows:

- Erosion rate is a linear function of time, strongly depends on the fluid velocity (v^5), and scales as the square of the *sin* of the impact angle;
- Hardening of the surface reduces the erosion rate significantly;
- The threshold for reduction of fracture stress of most ceramics is above a fluid-impact velocity of about 120 m/s;
- The incubation time for erosion of strengthened steel (12% Cr) for fluid velocities below 100-120 m/s is long. For all practical purposes the erosion rate due to low velocity fluids (< 100 m/s) may be negligible;
- Tangential erosion rates are lower by a factor of 10^{-4} than those of perpendicular fluid impact;
- Hardened surfaces improve the erosion resistance of the base material appreciably. Thus, ceramic coatings or nitrogen-rich semi-ceramic surface layers can significantly reduce erosion concerns;
- The number of sharp bends and contractions-expansions should be kept to a minimum to reduce large impact angles.

A limited number of experiments were conducted in the late 1960s to study the effects of high-velocity liquid lithium. The corrosion resistance of Nb-1Zr in lithium flowing at 50 m/s was evaluated for potential application in a magnetohydrodynamic space-power system [52]. The layer of material removed after 500 hours of exposure at 1073 to 1145 °C was measured to be 7.5-μm thick which corresponds to a corrosion rate of about 0.1 mm/y. Also, the compatibility of TZM with potassium vapor flowing at a velocity of 180 m/s was determined in a 3000-h turbine test [53]. The TZM turbine blades showed negligible corrosion after exposure to the 750 °C potassium vapor. Although the first experiment

used a niobium alloy with lithium and the second one used TZM with potassium, these findings suggest that high-velocity liquid metals should not lead to unexpected erosion processes.

Based on the experience of high-velocity water on erosion rates of metals and ceramics and on a limited experimental data base on high-velocity liquid lithium on Nb-1Zr, it does not seem that the 20 to 25-m/s velocity of the liquid lithium in the first-wall- and divertor-coolant channels of TITAN-I design would result in unacceptable erosion corrosion rates. It should be noted that further study is required to expand the database for lithium-vanadium systems.

10.2.2.4. Ferrous alloys

As discussed above, using a second material for the remainder of the coolant loop introduces the problem of bimetallic interstitial pickup. The vanadium alloy used as the primary structural material will pick up nitrogen and carbon depleted from any steel in contact with the same liquid lithium. Degradation of the mechanical properties will occur in both the V-3Ti-1Si and the steel.

Ferritic and austenitic steels have been investigated as potential structural materials for liquid-lithium systems [54 - 57]. The corrosion rates of austenitic and ferritic steels are compared in Figure 10.2-6 showing that the corrosion of ferritics can be an order of magnitude less than that of austenitics. In these experiments [55], the surface of 316-SS was found to be depleted of both nickel and chromium. The preferential leaching of these elements is believed to be the major cause of the high corrosion rates seen in austenitic stainless steels. The surface of austenitics exposed to high-temperature lithium was found to be highly porous [54]. Below 520 °C, porosity is minimal and deposits become the predominant surface feature.

A general characteristic of liquid-metal-corrosion test loops is that the weight loss is maximum at the point of the highest temperature. However, Tortorelli and DeVan [54] report that for HT-9, the coldest specimen (350 °C) had the largest weight loss. The steady-state weight-loss rate of ferritic steel HT-9 above 1000 hours of exposure to flowing lithium was determined to be 0.4 mg/m^2-h at 350 °C and 1.0 mg/m^2-h at 500 °C [55]. Chopra *et al.* [56] reported a slight drop in corrosion rate for 316-SS and a drastic rise in corrosion rate for HT-9, with increasing temperature.

Most recent forced-loop experiments performed by Bell *et al.* [58] on HT-9 samples have not shown any clear dependence between temperature and corrosion rates. For low

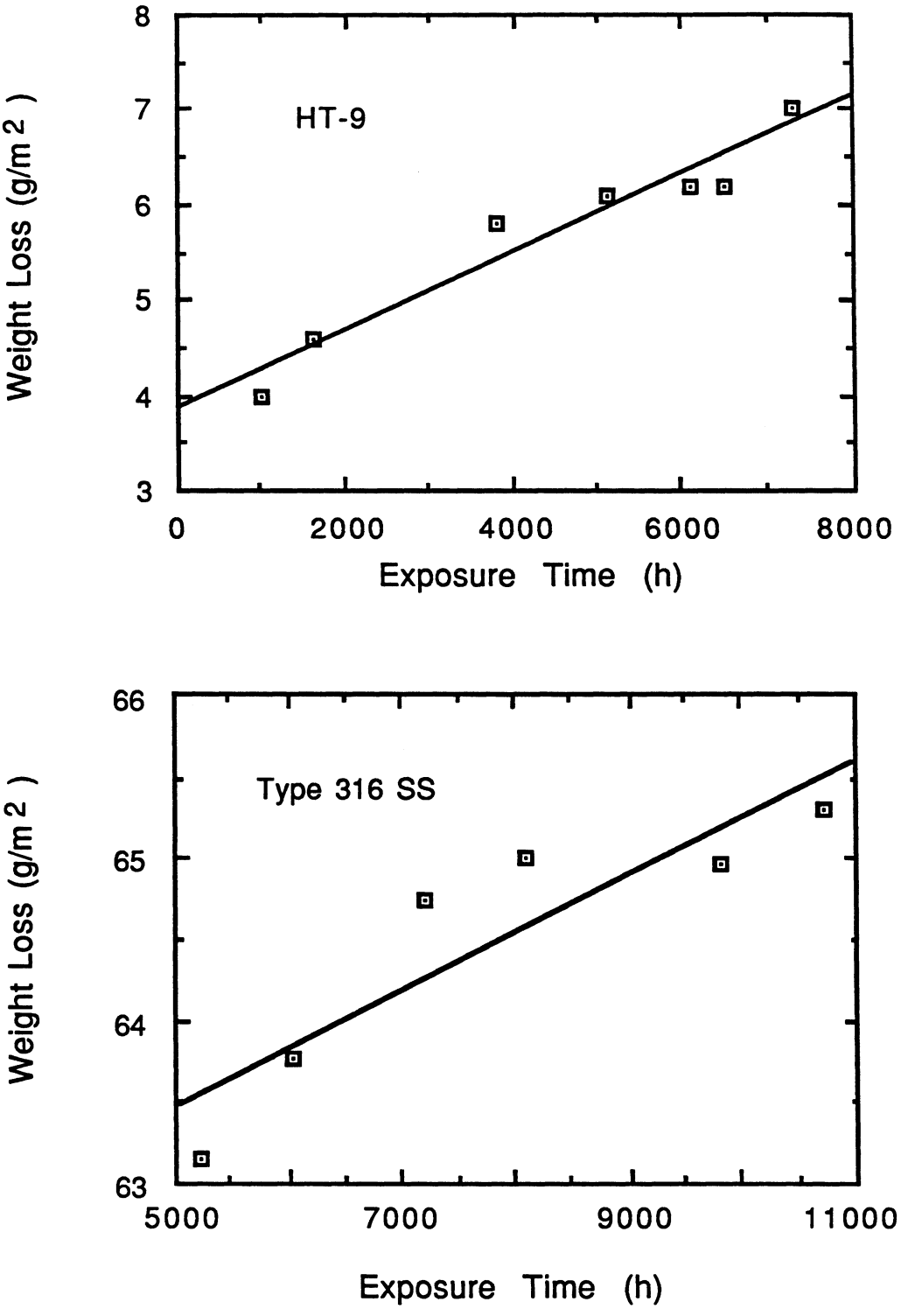

Figure 10.2-6. Weight loss as a function of the exposure time for HT-9 and 316-SS exposed to convective lithium at 500 °C [54].

exposure times of about 300 h, the dissolution rate of HT-9 was measured to be fairly temperature insensitive with a weight-loss rate of about 2 mg/m^2-h. After exposure times of 3000 h, the weight-loss rate was measured between 0.15 and 0.3 mg/m^2-h, respectively, for 500 and 350 °C. These latest findings [58] confirm the results from Tortorelli and De Van [54] of a decrease in corrosion rate of ferritics with increasing temperatures.

Although the above experiments did not report parabolic corrosion rates, Borgstedt *et al.* [57] estimated the corrosion rate of 304-SS by a parabolic equation as:

$$\Delta W = 6.2 \times 10^{-2} t^{0.60}, \qquad (10.2\text{-}17)$$

where ΔW is the weight-loss rate in g/m^2-h, and the time t is in hours. The test conditions resulting in Equation 10.2-17 were 551 °C with liquid lithium flowing at 7 cm/s.

These measured corrosion rates of HT-9 all fall below the mass-transfer limit of 5 μm/y ($\sim$ 5 mg/m^2 h) specified for nuclear power plants. The radioactive-mass-transport limit of 0.5 μm/y ($\sim$ 0.5 mg/m^2 h) is also satisfied for long-term exposure ($>$ 1000 h) of HT-9 to flowing lithium at temperatures up to 600 °C. Austenitic steel, on the other hand, barely falls below the mass transfer limit of 5 μm/y and does not satisfy the radioactive transfer limit of 0.5 μm/y. As pointed out before, these limits were derived from light-water-reactor experience with water-steel systems, which may be too conservative for a liquid-metal-cooled fusion reactor. Additional study of the redeposition of radioactive corrosion products and the redistribution of radioactive source terms is necessary. Furthermore, it may be possible to reduce the corrosion rate of austenitic steels by special techniques.

Inhibition of steel corrosion. Several methods for minimizing the corrosion rate of austenitic-steel alloys in liquid lithium have been investigated [59,60]. In particular, the emphasis was to reduce the nonmetallic impurity levels (*e.g.*, nitrogen and carbon) to minimize the mass transfer, and to eliminate the localized grain-boundary attack. Reduction of nonmetallic impurity levels was achieved by using conventional getters such as titanium wool or soluble chemical getters such as calcium [61]. The addition of corrosion inhibitors (*e.g.*, aluminum, calcium, barium, magnesium) to liquid lithium was tried as part of the space-nuclear-power program during the late 1950s [62]. However, the high mass-transfer rates were not affected by any of the corrosion inhibitors because of the high operating temperature ($>$ 800 °C). Recent experiments at lower temperatures show a factor of 5 reduction in corrosion of 316-SS when 5-wt.% aluminum was added to flowing lithium [63].

A third approach to corrosion inhibition has been the use of corrosion-resistant diffusion coatings. Diffusion coatings are produced by exposing the alloy to a chemical com-

pound of the desired coating material, which then dissociates and diffuses inward upon heating and forms an adhesive surface layer. Nickel-bearing alloys showed an increased resistance to corrosion by high-temperature lithium (700 °C) when diffusion-coated with molybdenum, molybdenum-titanium, and aluminum [64]. Diffusion-coated alloys are now commercially available for use in liquid sodium for breeder-reactor applications [65]. Recently, Burrow *et al.* [66] tested these commercially available diffusion-coated alloys in liquid lithium. They used a proprietary powder-pack process to coat samples of austenitic, ferritic, and high-nickel structural alloys with a 40- to 60-μm-thick aluminized diffusion coating. Both coated and non-coated specimens were tested in flowing lithium at 400 °C for 2000 h with an axial temperature differential of about 30 °C. The flow rate was kept constant at 2 cm^3/s. These tests showed that all aluminized materials demonstrated excellent compatibility with liquid lithium. While a minimal weight loss (1 g/m^2) and unaltered profiles for iron, chromium, and aluminum substantiated the stability of aluminized ferritics, no real benefit could be identified from these preliminary screening tests. Aluminized, high-nickel alloys, however, showed a drastic reduction in weight loss compared to the non-coated samples. Additional lithium studies are required before a definitive statement regarding the corrosion-inhibiting processes can be made.

10.2.3. Insulator Material

The mechanical integrity of insulating materials and retention of properties during exposure to radiation environments has always been a design concern. Electrically insulated components, such as magnets, need to be shielded to ensure acceptable performance. The amount of shielding material required will undoubtedly affect reactor dimensions. Another application of electric insulator materials is to mitigate magnetohydrodynamic (MHD) pressure drops. When a liquid metal is used as a coolant, the motion of the conducting fluid induces eddy currents which flow in the coolant and the structure. Interaction of these eddy currents with the magnetic field exerts a body force on the liquid metal and results in MHD pressure drops. Electrical insulation between the structure and the coolant reduces eddy-current flow in the structure and thereby reduces the MHD pressure drop.

The electrical insulators are also used as current breaks in electrically conducting components. Depending on their location, these breaks can be exposed to high levels of radiation and can play a significant role in plasma equilibrium and stability. Arcing between structure gaps or breaks is another concern that can be mitigated by the use of proper insulating material. A major consequence of arcing is localized melting and the subsequent release of high-Z material into the plasma chamber.

Insulating material requirements can be specific, depending on the location and function of the individual subsystems. However, the following properties are generally required from insulating materials exposed to radiation environments:

- Dimensional stability,
- Retention of mechanical properties,
- Compatibility with structural and coolant materials,
- Adequate electrical resistivity,
- Resistance to radiation-induced conductivity,
- Ease of fabrication.

In the TITAN-I reactor, no insulating material is in direct contact with coolant. Therefore, coolant compatibility is not a major issue in selecting an insulating material. The selection criteria is based primarily on satisfying minimum irradiation-induced swelling, retention of strength, and minimum radiation-induced conductivity.

10.2.3.1. Candidate insulating materials

Organic insulating materials generally do not meet high-temperature requirements and suffer from rapid degradation of their resistivity when exposed to ionizing radiation. Recently, however, Plansee [67] has succeeded in developing a polyamide insulator, SINTIMID, that is stable up to 290 °C for prolonged use and up to 400 °C for short exposure times. In preliminary radiation experiments, SINTIMID has shown to be highly resistant to radiation damage.

Ceramic insulating materials, on the other hand, possess high melting or decomposition temperatures ($> 2000\,^{\circ}\mathrm{C}$). Ceramics that have been investigated for fusion applications can generally be divided into graphites, carbides, nitrides, and oxides.

Graphites. Graphites suffer from large radiation-damage-induced strains because of the layered structure of the lattice. Isotropic graphites have been manufactured which show low radiation swelling at moderate fluence and good retention of thermal and mechanical properties [68]. At high fluence ($> 2 \times 10^{26}\,\mathrm{n/m^2}$), however, disintegration along grain boundaries occurs which is caused by cracking [69]. Graphites also suffer from rapid chemical sputtering when exposed to plasmas.

Carbides. Silicon carbide (SiC), a high-strength, high-thermal-conductivity ceramic, is the most widely studied carbide. At 800 K, the Young's modulus is about 400 Gpa and the yield strength is about 350 MPa. The thermal conductivity of SiC is about 37 W/m-K for unirradiated material and the thermal-expansion coefficient is 4.9×10^{-6} /K between 300 and 800 K. Because of its cubic structure, SiC swells isotropically under neutron irradiation. Silicon carbide shows relatively high dimensional stability with minimum swelling of about 1.2% at 1000 °C [70]. Swelling saturates at fluence between 10^{24} and 10^{25} n/m^2, depending on the temperature [71].

The most drastic effect of fast-neutron irradiation of SiC is the reduction of thermal conductivity. At 552 °C, SiC irradiated to a fluence of 2.7×10^{25} n/m^2 ($E_n > 0.18$ MeV) showed a reduction in the thermal conductivity by as much as 87% [70]. Other experiments at higher fluences showed an 80% reduction in thermal conductivity after irradiation to 2×10^{26} n/m^2 at 540 and 740 °C [72]. Recent experiments at room temperature indicate an increase in thermal conductivity of SiC from 50 to 270 W/m-K with the addition of 2 at.% BeO [73]. The addition of BeO had little or no effect on the thermal-expansion coefficient and theoretical density.

Silicon carbide is often considered as a structural material because of its strength, irradiation stability, resistance to creep and thermal stress, commercial availability, fabricability, and tritium retention. Although SiC has excellent resistance to growth and swelling in a wide range of temperatures and neutron doses, large amounts of transmutation gases have been shown to adversely affect the mechanical properties of SiC [74].

Nitrides. Nitride ceramics are the least studied among insulating materials for fusion applications. This is mostly because of their instability at high temperatures. Nitrides that are stable at high temperatures ($\geq$ 300 °C) include: AlN, BN, and Si_3N_4. Most nitrides have hexagonal crystal structures and show anisotropic growth and swelling leading to high radiation-induced strains. Most nitrides are stable in contact with vanadium, except Si_3N_4 which readily forms VN. Among the ceramics, nitrides show some of the best electrical resistivities, with BN having the lowest electrical conductivity ($10^{-14}/\Omega$-cm at 500 °C).

Another consideration regarding the use of graphites, carbides, or nitrides as insulating materials in contact with refractory alloys is the high affinity of most refractories to carbon and nitrogen. At elevated temperatures, carbon can be picked up by structural materials, resulting in carburization of the refractory metal and consequent loss of ductility. Furthermore, carbides suffer from a high level of hydrogen and helium generation rates. The hydrogen produced can bind with carbon to form volatile hydrocarbons

such as methane (CH_4). Helium will generally migrate to grain boundaries where it is trapped inside grain-boundary bubbles. This trapping is one of the major causes of crack formation and propagation along grain boundaries in irradiated graphites.

Oxides. Among the many oxide ceramics (*e.g.*, BeO, MgO, Al_2O_3, $MgAl_2O_4$, Y_2O_3, $Y_3Al_5O_{12}$, Si_2ON_2, and $Si_4Al_4O_2N_6$) considered for fusion applications, Al_2O_3 (alumina) is the most highly developed refractory ceramic, exhibiting good structural and electrical properties in a radiation-free environment. Alumina has a hexagonal cubic structure, resulting in anisotropic swelling and growth under neutron irradiation [75]. Therefore, neutron irradiation results in a relatively rapid degradation of properties [76].

Cubic-structured alloys of alumina, such as $MgAl_2O_4$ (spinel) and $AlN(Al_2O_3)_{1.8}$ (ALON), have shown the most resistance to radiation-induced swelling, and retained thermal conductivity and mechanical properties [77,78]. For example, the following insulators experience a 50% to 90% reduction in thermal conductivity after exposure to a fast-neutron fluence of $2.8 \times 10^{29}\,n/m^2$: BeO, MgO, Al_2O_3, $MgAl_2O_4$, Y_2O_3, $Y_3Al_5O_{12}$, Si_2ON_2, and $Si_4Al_4O_2N_6$) [70]. Spinel is one of the few ceramics that experience a relatively small drop of 8% in thermal conductivity after exposure to the same fluence [77].

Another favorable characteristic of spinel is its mechanical behavior upon exposure to radiation. Table 10.2-XIV shows the changes in the strength of polycrystalline spinel after fast-neutron irradiation to $2 \times 10^{26}\,n/m^2$ at 680 and 815 K [77]. This increase in the strength is attributed to the suppression of crack nucleation or propagation by the damaged microstructure. The fracture-toughness and hardness of single-crystal spinel showed little or no change after the same exposure levels at 925 and 1100 K [76]. These results indicate that spinel will retain its resistance to crack propagation under high-dose irradiation conditions.

Although spinel is not a high-strength, high-thermal-conductivity ceramic, its good behavior under irradiation makes it one of the more promising refractory ceramics for fusion reactor applications and it is chosen as the insulator material for the TITAN designs. Table 10.2-XV lists selected properties of spinel.

10.2.3.2. Swelling of spinel

Atomic-displacement damage can lead to the formation of voids in materials exposed to nuclear radiation. These voids are generally unstable at high temperatures because of thermal dissociation. In addition, transmutation reactions induced by neutrons introduce

Table 10.2-XIV.

TENSILE STRENGTH OF IRRADIATED[(a)] SPINEL [77]

Irradiation Temperature (°C)	Strength (MPa) Controlled	Irradiated	% Change
407	129	178	38
542	129	173	34

(*a*) Polycrystalline spinel irradiated to 10^{26} n/m^2.

soluble and non-soluble foreign atoms. Non-soluble elements such as helium are readily trapped in voids, resulting in the stabilization of otherwise unstable void embryos. At low temperatures (below room temperature) the voids can pack a high number of helium atoms and indirectly lead to a low swelling rate. At higher temperatures, helium atoms can become de-trapped and diffuse out of the matrix, also resulting in a low swelling rate. In the intermediate temperature range, however, mechanical equilibrium conditions between the surface tension and helium content of bubbles reduces the amount of helium per bubble to low values. Furthermore, the available thermal energy is not enough to de-trap a sufficient number of helium atoms. Thus, at intermediate temperatures, which can coincide with operating temperatures of most energy-producing systems, most materials suffer a swelling peak, as seen is Figure 10.2-7.

While pure materials generally experience high levels of swelling, mixing or alloying with different materials can drastically reduce swelling levels. One such example is spinel, which is a mixture of MgO with Al_2O_3 (alumina). Spinel is more swelling resistant than either alumina or MgO. For a damage dose of 10 dpa, alumina swells up to about 4% [81,82] between 650 and 830 °C, MgO swells up to 3.0% [81] at 167 °C, while spinel shows virtually no swelling at these temperatures [81]. Figure 10.2-8 shows the drastically different swelling rates between alumina and spinel after neutron irradiation [76 - 84].

Swelling can have significant effects on insulator performance. Nonuniform swelling can lead to a variation in thermal conductivity across the insulator. In the presence of a temperature gradient, a swelling gradient can develop across the material since swelling

Table 10.2-XV.

SELECTED SPINEL PROPERTIES

Density	3540	kg/m^3
Crystal structure	cubic	
Decomposition temperature	2135	°C
Coefficient of thermal expansion		
at 600 °C	8×10^{-6}	/K
at 1000 °C	9×10^{-6}	/K
Thermal conductivity		
at 23 °C	20	W/m-K
at 600 °C	8.1	W/m-K
at 1000 °C	6	W/m-K
Electrical resistivity		
at 100 °C	$> 10^{16}$	Ω m
at 200 °C	10^{15}	Ω m
at 600 °C	10^{9}	Ω m
Young's modulus (1000 °C)	206	GPa
Flexural strength (1000 °C)	250	MPa
Typical impurities [79]		
Si	400	wppm
Ca	100	wppm
Na	80	wppm
B	35	wppm
Fe	20	wppm
Grain size	10-100	μm
Porosity (polycrystalline spinel)	6%	

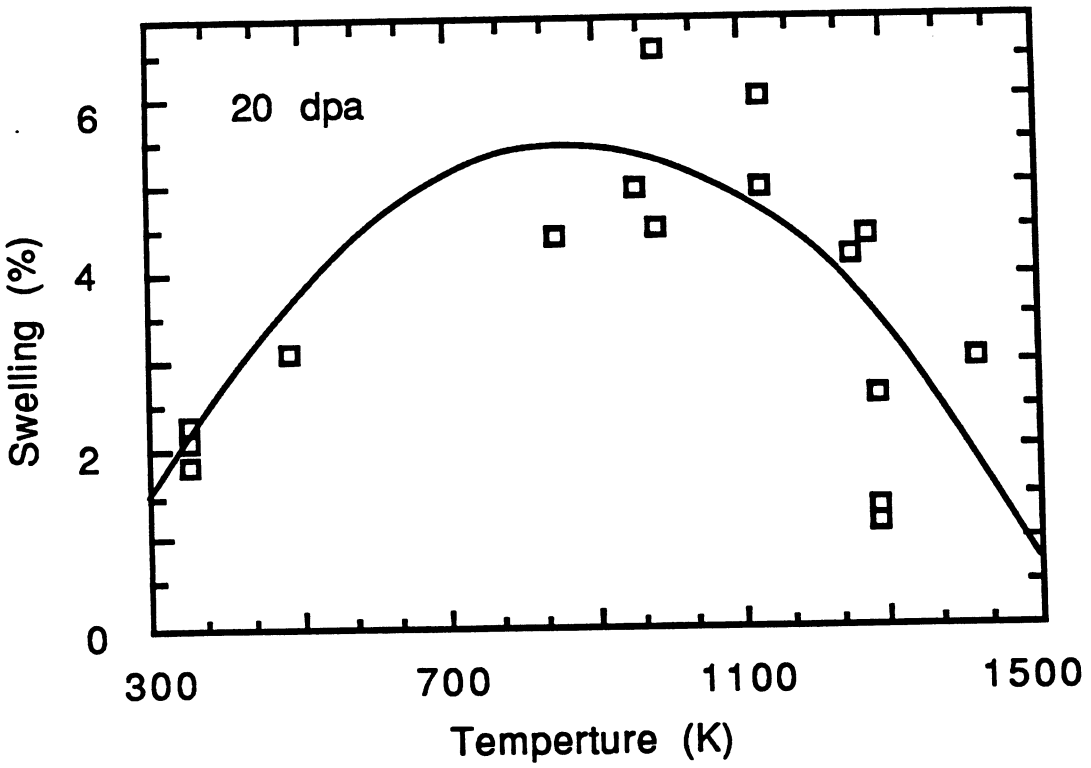

Figure 10.2-7. Swelling of polycrystalline alumina as a function of temperature after a damage dose of 20 dpa [80].

is temperature dependent. The swelling gradient in turn compounds the effects of the temperature gradient, resulting in unacceptable thermal stresses. Stress concentrations around surface or lattice defects can result in crack formation. Cracks that propagate to the surface will allow impurity gases to penetrate the ceramic. The insulating property of the material can in this way be dominated by filler gases (higher conductivity), rather than the bulk insulating material itself.

Because of the degradation of mechanical and physical properties, swelling of insulating materials is of great concern. Generally, swelling is the life-limiting criteria for a load-bearing insulator. Volume changes of alumina and spinel induced by irradiation with 14-MeV neutrons at 50 °C were measured by Tanimura and Clinard [75]. It was shown that the volume change of Al_2O_3 is anisotropic and is larger than that of spinel by about a factor of five. Above 900 K the swelling of spinel is less than 10% of that of Al_2O_3 [85,86]. Table 10.2-XVI shows some of the experimental data on swelling of spinel. These experimental data on swelling as a function of temperature and damage

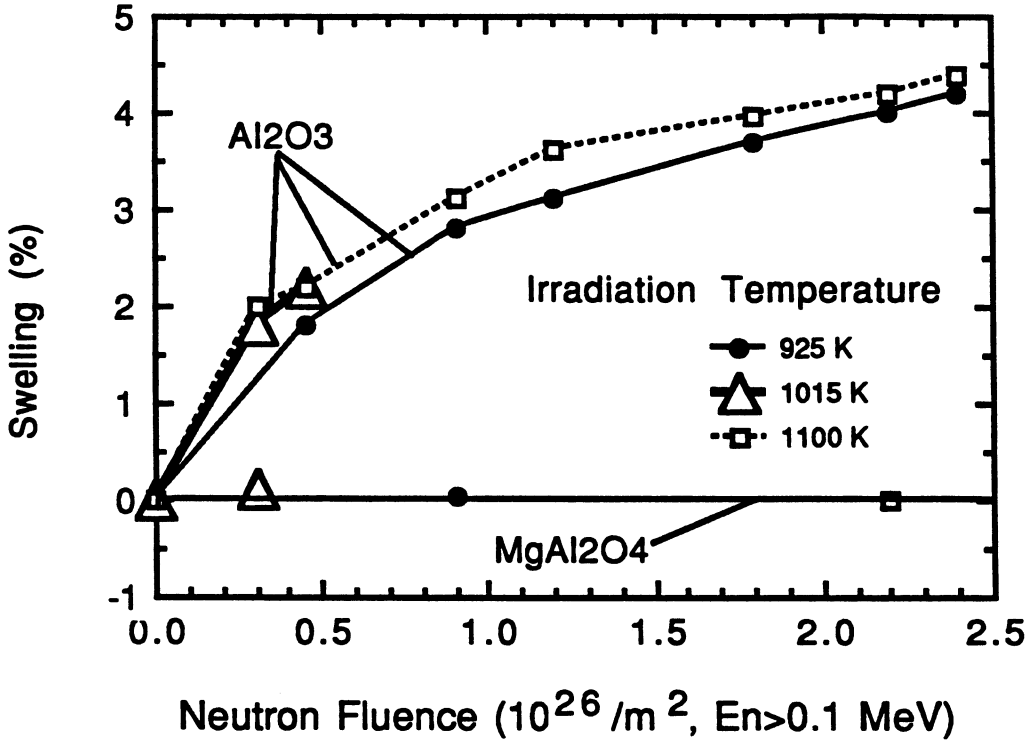

Figure 10.2-8. Swelling of single-crystal alumina and spinel after neutron irradiation at high temperatures [84].

dose, however, are not sufficient to extrapolate empirical design equations. Therefore, a phenomenological swelling equation based on the limited swelling data was developed to establish a lifetime criteria for spinel for the TITAN-I design.

Most ceramics exhibit a bell-shaped swelling curve as a function of temperature, with a swelling peak in the range of 0.2 to $0.5\,T_m$ (melting point of the material in K). Such swelling curves are available for CaF_2, ZrO_2-Y_2O_3, alumina, and SiC [81]. A similar temperature-dependent, bell-shaped swelling behavior for spinel can also be seen in Table 10.2-XVI. The approximate swelling equation as a function of temperature and dpa was found to be

$$\frac{\Delta V}{V} \simeq 3.46 \times 10^{-2}\,\delta \exp\left[-\left(\frac{T-220}{122}\right)^2\right], \qquad (10.2\text{-}18)$$

where $\Delta V/V$ is the swelling rate in %, δ is the damage dose in dpa, and T is the irradiation temperature (°C). Coghlan *et al.* [87] have recently estimated the dpa for spinel to be $\sim 1.17 \times 10^{-25}$ dpa/(n/m^2).

Table 10.2-XVI.

SWELLING OF NEUTRON-IRRADIATED SPINEL ($MgAl_2O_4$)

Temperature (K)	$\Delta V/V$ (%)	Fluence (n/m^2)[(a)]	Reference
323	0.03 ± 0.01	3.2×10^{26}	[87]
407	0.08 ± 0.01	2.1×10^{30}	[81]
680	-0.19 ± 0.01	2.2×10^{30}	[77]
815	-0.35 ± 0.01	2.2×10^{30}	[76]
925	± 0.01	2.3×10^{28}	[81]

(a) Fast-neutron fluence ($E_n > 0.1\,\text{MeV}$).

For TITAN-I at $18\,MW/m^2$ of neutron wall loading, spinel located at the first wall or divertor will experience a total damage dose of ~ 180 dpa after one FPY of operation. Figure 10.2-9 shows the swelling of spinel at the first wall of TITAN-I as a function of temperature and exposure time, as estimated by Equation 10.2-18. This swelling curve shows that operating spinel below 150 °C or above 350 °C ensures low swelling rates and operation in these temperature ranges is favored.

10.2.3.3. Dielectric-breakdown strength and radiation-induced conductivity

Dielectric-breakdown strength (DBS) of ceramic insulators is defined as the maximum potential gradient in the dielectric without the occurrence of an electric breakdown. High temperatures degrade the DBS since excess thermal energy leads to an increase in drift currents and additional heating, eventually avalanching into a breakdown current. Although no data are available for the DBS of spinel, the DBS has been measured for alumina. Since spinel consists of 66% alumina and $\sim 33\%$ MgO, it is assumed that the DBS of spinel is about the same as that of alumina. Below 200 °C, the DBS for alumina is about 12 kV/mm and it reduces to, respectively, about 8 and 2.5 kV/mm at 350 and 700 °C. Since high temperatures degrade DBS, it is desirable to operate insulating materials at low temperatures.

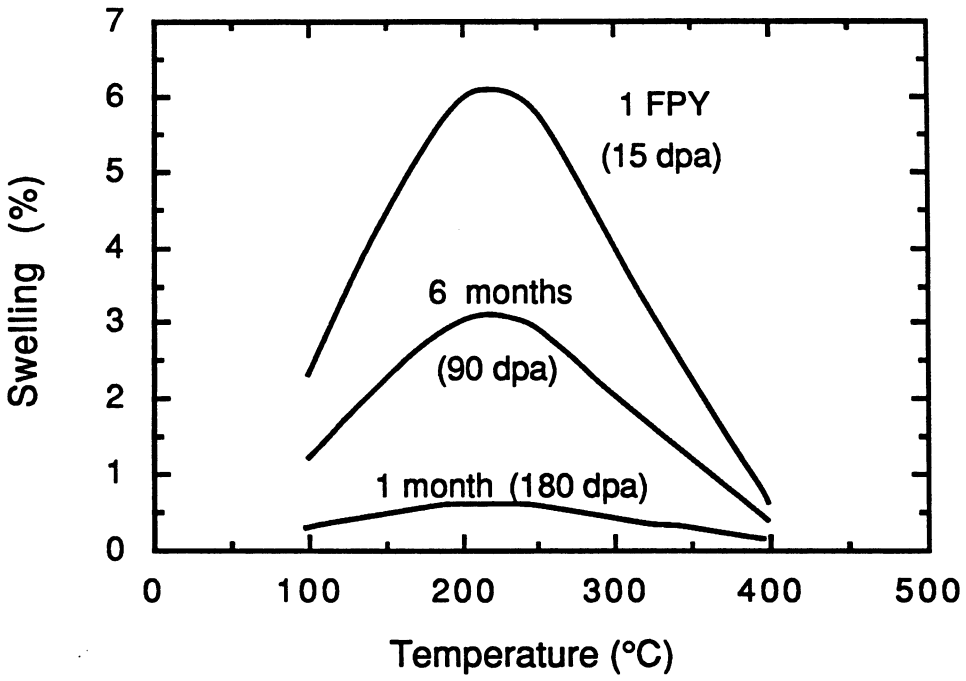

Figure 10.2-9. Swelling of spinel as a function of damage dose and temperature.

Ionizing radiation, mostly by γ-rays, also leads to an increase in electrical conductivity. The γ-ray photons interact with electrons which increases the concentration of conduction-charge carriers. This phenomenon is a flux-dependent effect (instantaneous) and is commonly known as radiation-induced conductivity (RIC). Klaffky [88] measured the RIC of alumina, both doped and un-doped with Cr_2O_3, as a function of ionizing dose rate between 300 and 1250 K in a radiation field of a 1.5-MeV electron beam. He showed that the conductivity of single-crystal Al_2O_3 increased as a function of dose rate, up to 10^{-4} mho/m for un-doped material at 6.6×10^2 Gy/s (1 Gy = 100 rads).

Doping, as well as neutron irradiation, significantly reduces conductivity at a given temperature. Un-doped alumina is characterized by the presence of shallow electron traps, while doped or neutron-irradiated material contains deep traps. The temperature dependence of the conductivity is complex, showing a minimum conductivity around 440 °C for all doped specimens. The conductivity falls as the temperature is increased from room temperature because of the release of electrons from shallow traps. For doped alumina, there is a characteristic temperature at which the shallow traps are depleted and conductivity reaches its minimum value. As the temperature is increased beyond this point, the thermal energy provided to electrons residing in deep traps is sufficient to cause an increase in conductivity at higher temperatures.

Recently, Pells *et al.* [89] measured the conductivity of spinel exposed to ionizing radiations of 7.5 Gy/s (X-rays) between 20 and 800 °C. While unirradiated spinel has a conductivity of about 10^{-13} mho/m, the irradiated spinel conductivity was measured around 10^{-8} mho/m at 200 °C. The conductivity of the irradiated spinel is not very sensitive to temperature and ranges between 10^{-8} to 10^{-7} mho/m between 20 and 800 °C. These data are used [89] to estimate the dependence of the conductivity of spinel on the fluence, $\dot{\gamma}$, as

$$\sigma_{RIC}^{sp} \sim 1.33 \times 10^{-9} \dot{\gamma}\,, \tag{10.2-19}$$

where σ_{RIC}^{sp} is the spinel RIC in mho/m and $\dot{\gamma}$ is the dose rate (Gy/s). For the 18-MW/m^2-neutron-wall-loading TITAN-I design, $\dot{\gamma}$ at the first wall is $\sim 2.7 \times 10^4$ Gy/s. This increases the conductivity of spinel at the first wall to $\sim 3.5 \times 10^{-5}$ mho/m. Klaffky [90] showed that alumina doped with less than 0.03 wt.% Cr_2O_3 experiences a reduction of conductivity by more than one order of magnitude. Similar doping techniques can be developed for spinel, but have not yet been investigated.

Radiation-produced defects also contribute to RIC. These defects increase the number of electron-scattering sites and the number of deep electron traps, resulting in an enhancement of overall conductivity. This effect is time dependent and, thus, a function of fluence. A single-crystal alumina irradiated to 3×10^{24} n/m^2 at 150 °C was shown to have an RIC even lower than that of the Cr_2O_3-doped alumina by Klaffky [88]. Neutron-irradiated samples showed the lowest radiation-induced conductivity.

Based on the above observations, spinel has been chosen as the primary electrical-insulator material for the TITAN-I design. Most ceramic insulating materials studied in the past are "off-the-shelf" insulators used commonly in nonirradiation environments. Although spinel appears to possess adequate properties for severe radiation environments, nonconventional insulating materials are being developed with far superior characteristics. One such relatively new insulator is $AlN(A_2O_3)_{1.8}$ (aluminum oxynitride spinel), a ceramic referred to as ALON which is being developed for infrared-window applications [91]. Several specimens of polycrystalline ALON were irradiated with 0.8- and 1-MeV electrons between 300 and 1100 K [78]. No defects were observed at any temperature through either thick or thin sections. The lack of any bulk irradiation effect was attributed to the difficulty of forming dislocations in ALON. From these preliminary investigations it appears that ALON is radiation-damage resistant. Future investigations into the radiation behavior of ALON are currently underway [78].

10.2.4. Summary

From the three candidate vanadium-base alloys, V-3Ti-1Si was chosen as the primary structural material for TITAN-I. The choice was primarily based on the irradiation behavior of this alloy. The V-3Ti-1Si alloy outperforms V-15Cr-5Ti and VANSTAR as far as helium embrittlement, irradiation hardening, and swelling are concerned after exposure to a damage dose of 40 dpa by fast neutrons. However, V-3Ti-1Si has the lowest thermal-creep resistance when compared to the other two alloys.

The minimum-commitment method was used to extrapolate the creep-rupture data and establish the creep behavior during normal and off-normal operating conditions. From the limited creep data, it appears that V-3Ti-1Si will be able to operate satisfactorily at elevated temperatures (700 °C). To include the effects of the irradiation hardening, helium embrittlement data was used to estimate the maximum allowable design stress based on a 2/3 creep-rupture-stress criteria. Additional creep-rupture experiments are needed to develop more precise creep-rupture models for V-3Ti-1Si.

Compatibility of the vanadium-base alloys with lithium coolant was investigated. Recent test results were used to establish the anticipated degree of lithium attack on the V-3Ti-1Si alloy. Various lithium-attack processes were examined, and particular attention was given to the interaction between vanadium and nonmetallic impurities such as oxygen, nitrogen, carbon, and hydrogen. The limited available data do indicate the possibility of a self-limiting corrosion rate on V-3Ti-1Si because of the formation of complex vanadium-titanium-nitride surface layers. The effects of a bimetallic-loop containing liquid lithium was also investigated. Low-carbon, titanium-stabilized ferritic steel exhibits good resistance against lithium corrosion.

The effects of high-velocity lithium on erosion was estimated using water-steel data. From a very limited set of data on erosion of refractory metals by a high-velocity liquid lithium and from the water-steel experience, it seems that lithium velocity of 20 to 25 m/s should not introduce unacceptable erosion rates.

Spinel ($MgAl_2O_4$) has been chosen as the primary electrical-insulating material for the TITAN-I design based on its excellent resistance to radiation-induced swelling and retention (or increase) of strength. A phenomenological swelling equation was developed as a function of temperature and damage dose. The swelling data were incorporated into a phenomenological swelling equation which shows that spinel located close to the first wall should not experience more than a maximum of about 5% swelling if operated below 150 °C or above 300 °C. High operating temperatures may ensure a low swelling rate but

could bring about dielectric breakdown of the insulator. Therefore, low-temperature operation ($< 150\,°C$) is suggested.

Radiation-induced conductivity (RIC) is a complex function of temperature, ionizing radiation dose, and neutron damage. Experiments performed on samples of single-crystal alumina and polycrystalline spinel indicate adequate resistance to RIC in a fusion environment. Radiation-induced conductivity of doped alumina has been investigated and it has been shown that doping can drastically reduce RIC. It is anticipated that doped spinel will show similar positive effects.

Development of new ceramic insulating materials capable of withstanding intense radiation environments is in the early stages. The relatively new insulator, ALON, has shown to be unusually radiation-damage resistant.

10.3. NEUTRONICS

The neutronics design of the blanket and shield for the TITAN reactors is unique because of the high neutron wall loading ($18\,MW/m^2$). The resulting shorter lifetime (in reactor years) of various components makes the annual replacement mass (and cost) of the blanket and shield components an important factor in the neutronics optimization. Note that even though the lifetime of various components is shorter, these components are usually smaller and, therefore, the annual replacement mass is somewhat insensitive to the neutron wall loading. The other unique aspect of the TITAN reactors is the use of normal-conducting coils in the toroidal-field, divertor, and ohmic-heating (OH) magnets. The use of normal-conducting coils will greatly reduce the shielding requirements for these components from radiation damage and will maintain the compactness of the design.

Over the TITAN-I reactor lifetime (30 FPY), the neutron-fluence limit of the magnets is $4 \times 10^{26}\,n/m^2$ (for $E_n \geq 0.1\,MeV$), or even higher [92], and is set by the spinel insulator lifetime (Section 10.2.3). The neutron-fluence limit for a superconductor magnet is only about $1 \times 10^{23}\,n/m^2$ (for $E_n \geq 0.1\,MeV$) [93]. This 3 to 4 orders of magnitude difference in the neutron-fluence limit allows a 0.6- to 0.8-m reduction in the shielding space between the plasma and the magnet system for the TITAN-I design.

This section describes the neutronics aspects of the TITAN-I fusion power core (FPC). A detailed survey of the performances of various blanket and shield combinations (*e.g.*, thickness and composition) was performed and reported in Section 10.3.1. The final neutronics design of the FPC is given in Section 10.3.2. Waste-disposal ratings of the TITAN-I design are discussed separately in Section 13.7.

10.3.1. Neutronics Optimization

Tritium breeding, blanket energy multiplication, afterheat, radiation damage to the structural materials and the OH magnets, annual replacement mass (and cost) of blanket and shield, and the waste-disposal ratings are some of the important parameters that were considered for the neutronics optimization of the TITAN-I design. Neutronics calculations were performed to investigate each of the above parameters based on a 1-D blanket and shield model in a cylindrical geometry, with the center of the poloidal cross section of the plasma located on the centerline of the cylinder. The parameters of the final design were verified by a set of 3-D calculations. The neutron and gamma-ray transport code, ANISN [94], is used with the cross-section library ENDF/B-V-based MATXS5 which was processed with the NJOY system at Los Alamos National Laboratory [95].

The neutronics model used in the optimization study consists of a 1-cm first wall, a 1-cm gap, a 75-cm blanket and shield zone, and a 1-cm gap followed by the OH magnet. The first wall is composed of 40% vanadium alloy, 38.5% lithium, and 21.5% void (in this section, the composition of the FPC components are in volume fraction). The blanket consists of vanadium alloy and lithium with varying volume fractions. The shield is made of 10% lithium and 90% vanadium. The OH magnet consists of 70% copper, 10% insulator (spinel), 10% structure (304-SS), and 10% coolant (helium). For the purpose of estimating the lifetime of various components, a 200-dpa damage limit has been used.

Table 10.3-I summarizes the results of neutronics calculations for several combinations of blanket and shield thicknesses, varying amounts of structure in the blanket, and with different levels of ^{6}Li enrichment in the lithium coolant. The next subsections review the results of this table and the approach to the optimization of various neutronics parameters.

10.3.1.1. Tritium breeding

Adequate tritium breeding is a fundamental requirements for a DT fusion reactor. A tritium-breeding ratio (TBR) of no less than 1.20, based on a 1-D full-coverage calculation, was used as the goal of the neutronics study. Table 10.3-I shows that adequate TBR is obtainable in most blanket arrangements, except when the blanket thickness is less than 40 cm and the blanket contains more than 60% vanadium. The enrichment level of ^{6}Li in the lithium coolant can be used to control the TBR in these blanket systems. At a higher ^{6}Li enrichment, the contribution of tritium breeding from ^{7}Li will decrease, as is shown in Table 10.3-I.

Table 10.3-I.

NEUTRONICS PERFORMANCE OF SEVERAL SELF-COOLED LITHIUM BLANKET SYSTEMS

Blanket System	^{6}Li Enrichment (%)	Tritium-Breeding Ratio[a]	M[b]	Energy Leakage (% M)	Max. dpa at Shield[c]	Max. Fluence at Magnet (n/m^2)[c]
10% V blanket	7.4	1.413 (34.)	1.12	6.6	373	2.1×10^{27}
60-cm blanket	40.	1.358 (22.)	1.13	4.3	271	1.1×10^{27}
15-cm shield	75.	1.211 (10.)	1.15	3.5	235	9.6×10^{26}
	7.4	1.205 (21.)	1.17	2.9	306	5.8×10^{26}
30% V blanket	20.	1.278 (17.)	1.16	2.3	272	5.4×10^{26}
50-cm blanket	30.	1.293 (15.)	1.15	2.0	248	5.0×10^{26}
25-cm shield	40.	1.284 (13.)	1.15	1.8	233	4.8×10^{26}
	75.	1.222 (5.5)	1.16	1.4	201	4.1×10^{26}
60% V blanket	15.	1.077 (8.7)	1.18	1.1	360	2.6×10^{26}
37-cm blanket	30.	1.159 (6.6)	1.16	0.92	304	2.2×10^{26}
38-cm shield						
60% V blanket						
40-cm blanket	75.	1.205 (2.3)	1.16	0.63	199	1.8×10^{26}
35-cm shield						

(*a*) The values given in parentheses are fractional contributions (in %) to TBRs from ^{7}Li(n,n′α) reactions; the rest are from ^{6}Li(n,α).

(*b*) Blanket energy multiplication, M, is defined as ratio of total nuclear energy deposited in the first wall, blanket, and shield to the incident DT neutron energy.

(*c*) For 30-FPY operation at 18 MW/m^2 of neutron wall loading.

10.3.1.2. Blanket energy multiplication

The blanket energy multiplication of fusion neutrons in the systems of Table 10.3-I ranges from 1.12 to 1.18, depending on the amount of vanadium structure (10% to 60%) in the blanket. In principle, the energy released by the exothermic capture of neutrons by the structural elements exceeds the energy produced by the absorption of neutrons by ^{6}Li to produce tritium. The capture of excess neutrons in the blanket to enhance blanket energy multiplication is common in recent reactor studies. Beryllium has been used in some designs to provide a large quantity of excess neutrons.

Manganese in manganese stainless steel (*e.g.,* Fe14Mn2Cr2Ni) has shown to be effective in increasing the blanket energy multiplication by about 0.4. However, about 45% of this excess energy is actually produced by the decay of ^{56}Mn nuclide, resulting from the absorption of neutrons in manganese. After shutdown of the reactor, the large level of ^{56}Mn afterheat would impose a potential safety problem, particularly for high-power-density systems such as the TITAN-I design; therefore, manganese stainless steel is not recommended as a shield material.

The final TITAN-I design uses a vanadium shield. Furthermore, a ^{6}Li-rich (30% enrichment) blanket coolant is used in order to further reduce the level of afterheat, to minimize the neutron flux at the shield and magnet, and to suppress the production of long-lived radionuclides and radiation damage to these components. At this level of ^{6}Li enrichment, the blanket energy multiplication ($\sim$ 1.16, Table 10.3-I) tends to be somewhat independent of the blanket and shield composition.

10.3.1.3. Afterheat

The level of afterheat in the vanadium-alloy structural material of the blanket and shield is affected by ^{6}Li enrichment. Table 10.3-II shows a comparison of estimated levels of afterheat at different times for two extreme enrichment levels in a blanket composed of 20% vanadium. For a highly enriched ^{6}Li coolant, a factor of eight reduction in the level of afterheat at shutdown can be achieved which lasts for about one hour. The afterheat level at shutdown in dominated by ^{52}V which is produced by ^{51}V(n,γ) reactions. The large population of low-energy neutrons in the depleted ^{6}Li system enhances the production of ^{52}V in the vanadium alloy. Fortunately, the half-life of ^{52}V is only 3.75 minutes, which significantly reduces the afterheat at longer times after shutdown. It was also found that the afterheat can be reduced by about 30% if vanadium alloy in the blanket is decreased from 20% to 10%.

Table 10.3-II.

COMPARISON OF AFTERHEAT LEVELS FOR DIFFERENT ^{6}LI ENRICHMENT

	Afterheat/Reactor Thermal Power[a]	
Time After Shutdown	2% ^{6}Li	75% ^{6}Li
At shutdown	3.3%	0.43%
5 minutes	1.5%	0.29%
1 hour	0.13%	0.13%
1 day	0.09%	0.09%
10 days	0.025%	0.025%

(*a*) For a blanket composed of 20% V in a 2700-MWt reactor.

10.3.1.4. Atomic displacement and annual replacement mass

Table 10.3-I shows the maximum atomic displacement in the shield, accumulated over 30 FPY at 18 MW/m^2 of neutron wall loading, for different blanket compositions and ^{6}Li enrichments in lithium. The atomic displacement in the shield decreases drastically as the ^{6}Li enrichment increases; the atomic displacement can be reduced by more than 50% when a highly enriched (75%) coolant is used instead of natural lithium (7.42%). This reduction is also seen for the fast-neutron fluence ($E_n \geq 0.1$ MeV) at the OH magnet.

The radiation-damage limit for the structural alloy in the TITAN-I design was set at 200 dpa. The average annual replacement mass of vanadium (first wall, blanket, and shield) is illustrated in Figure 10.3-1 as a function of allowable fast-neutron fluence at the magnet for several blanket compositions and thicknesses. This figure shows that for a given fluence at the magnet: (1) ^{6}Li enrichment tends to reduce the replacement mass, (2) a blanket with smaller amount of structure gives a lower replacement mass since lithium also attenuates the neutron flux, and (3) a thicker blanket and shield yield less replacement mass.

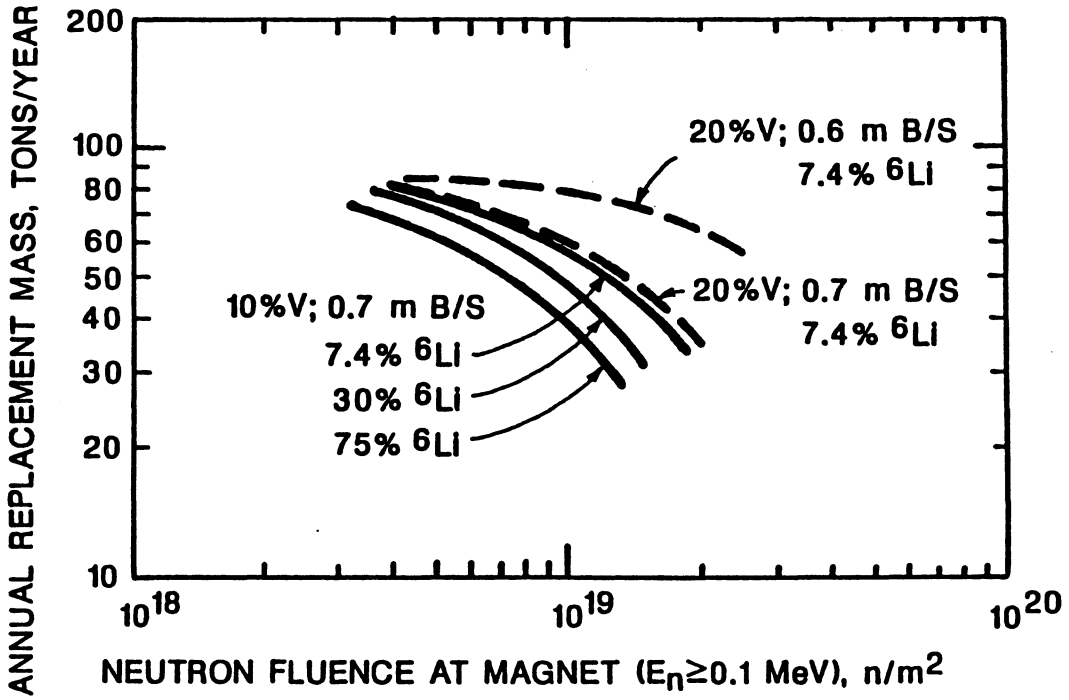

Figure 10.3-1. Averaged annual replacement mass of vanadium alloy in the TITAN-I blanket and shield as a function of 30-FPY integrated fast-neutron fluence at the OH magnet.

10.3.1.5. Waste-disposal ratings

One of the objectives of the TITAN study has been to meet the 10CFR61 [96] Class C waste-disposal criteria for low-level waste qualified for shallow-land burial. This objective has guided the material selection and neutronics optimization. Suppression of the low-energy neutron population by increasing the ^{6}Li enrichment in the coolant was found to be effective in reducing the production rate of long-lived radionuclides.

The alloying elements for vanadium alloy (V-3Ti-1Si) do not produce significant quantities of long-lived radionuclides. However, the impurity elements will affect the waste classification of the disposed TITAN-I components and, therefore, should be controlled. Niobium is the most important among the elements shown as impurities in the vanadium alloy [2]. The amount of the long-lived radionuclide from niobium, ^{94}Nb, was found to depend strongly on the ^{6}Li enrichment. The production rate of ^{94}Nb can be reduced by a factor of nine if a 60% enriched lithium is used instead of natural lithium composition. Detailed evaluation of radioactive-waste-disposal ratings of the TITAN-I design is given in Section 13.7.

10.3.2. Reference Design

Based on the neutronics optimization considerations of Section 10.3.1, the reference design of the TITAN-I reactor is determined, and is illustrated in Figure 10.3-2.

The structural material is the vanadium alloy, V-3Ti-1Si. The lithium coolant is enriched to 30% ^{6}Li which is a compromise between neutronics performance and enrichment cost (Section 10.2.2.1). The first-wall region is 1-cm thick and consists of 40% structure, 37.5% lithium, and 22.5% void. The composition and size of the first wall is dictated by thermal-hydraulic considerations. The first wall is followed by a 1-cm gap and by the TITAN-I integrated blanket coil (IBC) which is 28-cm wide and consists of 18% structure, 72% lithium, and 10% void. The IBC is followed by a 1-cm gap and a hot shield. The width of the IBC section is chosen such that the shield lifetime is 4 FPY (five reactor years), based on the damage rate at the front of the shield. The hot shield is 45-cm wide and is made of two zones. The first zone is 30-cm thick and composed of 30% structure and 70% lithium; the second zone is 15-cm thick with 90% structure and 10% lithium. The coolant channels in the hot shield have a rectangular cross section so that there is no void. If the cost of vanadium alloy proves to be very high, the shield material may be replaced by an appropriate "modified" low-activation stainless steel without imposing large penalties on tritium breeding, nuclear heating, afterheat, and magnet-shielding issues.

The neutronics performance of the reference design with a vanadium-alloy shield is given in Table 10.3-III, as calculated by a 1-D analysis. The TBR is 1.33, of which 1.084 is from the ^{6}Li(n,α)T reaction, and 0.247 from the ^{7}Li(n,n'α)T reaction. The total nuclear heating is 16.05 MeV per DT neutron (11.11 MeV from neutron nuclear heating and 4.94 from γ-rays), resulting in a blanket energy multiplication of 1.14. The maximum fast-neutron fluence at the OH magnet after 30 FPY of operation at 18 MW/m^2 of neutron wall loading was found to be 7×10^{26} n/m^2 (for $E_n \geq 0.1$ MeV), which is substantially lower than the estimated lifetime limit of 2×10^{27} n/m^2 for the spinel insulator.

A set of more accurate, 3-D neutronics calculations was performed with the Monte-Carlo code, MCNP [97], taking into account the toroidal geometry and the divertor modules. Figure 10.3-3 shows the plan view of the 3-D MCNP model for the TITAN-I reactor which includes half of the 13° segment for the divertor module in the toroidal direction. The elevation view of the model, also illustrated in Figure 10.3-3, shows the opening of the divertor in the outboard region. The divertor coils are located 5 cm from the first wall and protected by a two-zone divertor shield, which is made of 10% lithium and 90% vanadium alloy. The first zone is 15-cm thick and is replaced after one FPY

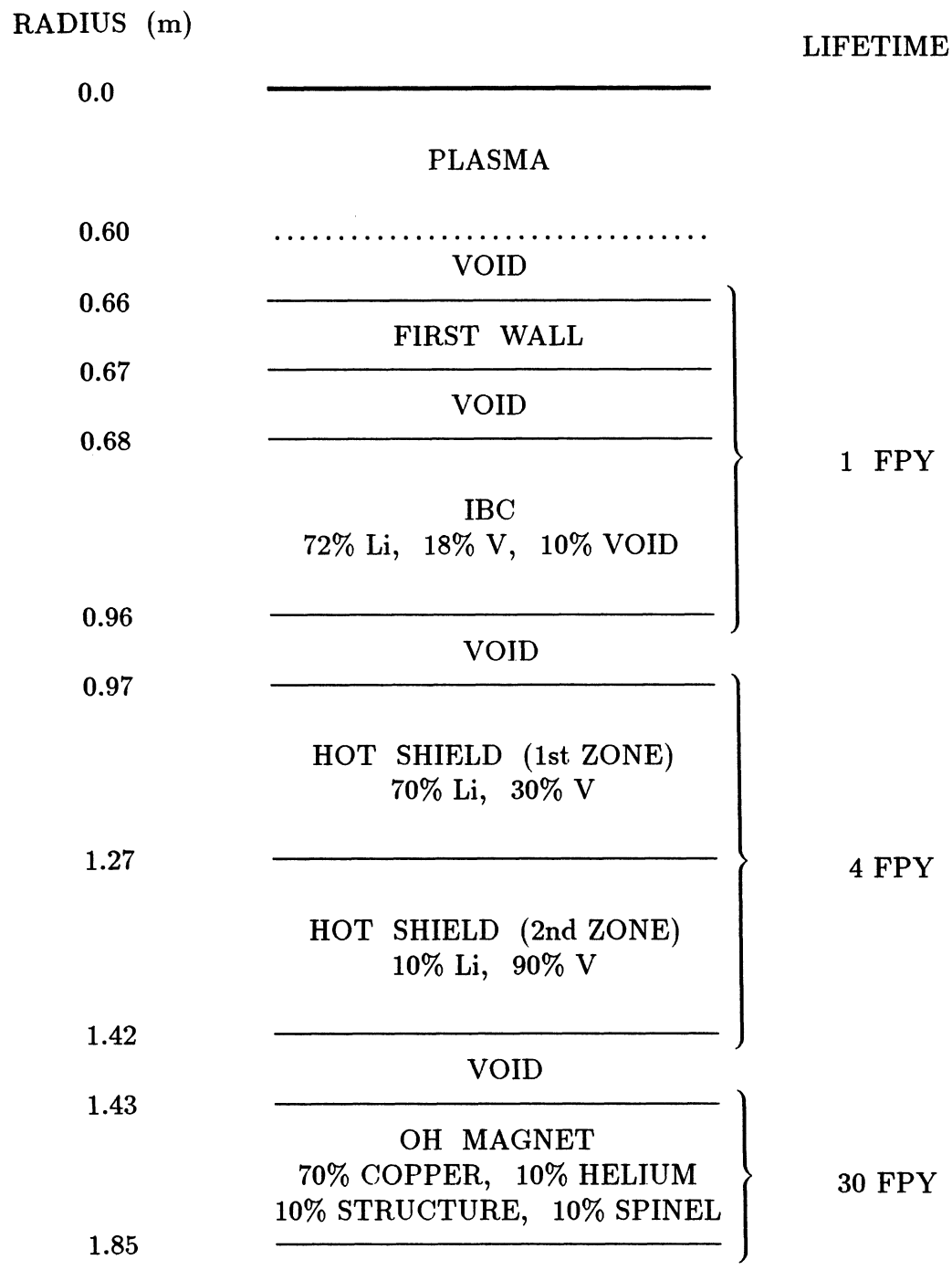

Figure 10.3-2. Schematic of the blanket and shield for the TITAN-I reference design.

Table 10.3-III.

NUCLEAR PERFORMANCE OF THE TITAN-I REFERENCE DESIGN[a]

^{6}Li enrichment	30%
Tritium-breeding ratio:	
^{6}Li (n,α)	1.084
^{7}Li (n,n'α)	0.247
TOTAL	1.33
Blanket energy multiplication, M	1.14

Nuclear heating (MeV per DT neutron):

Component	Neutron	Gamma-Ray	Sum
First wall	0.341	0.183	0.524
Blanket	7.382	2.603	9.985
Shield (1st zone)	3.148	1.595	4.743
Shield (2nd zone)	0.235	0.560	0.795
TOTAL	11.106	4.941	16.047
OH coils	0.038	0.438	0.476

(*a*) From 1-D ANISN calculations.

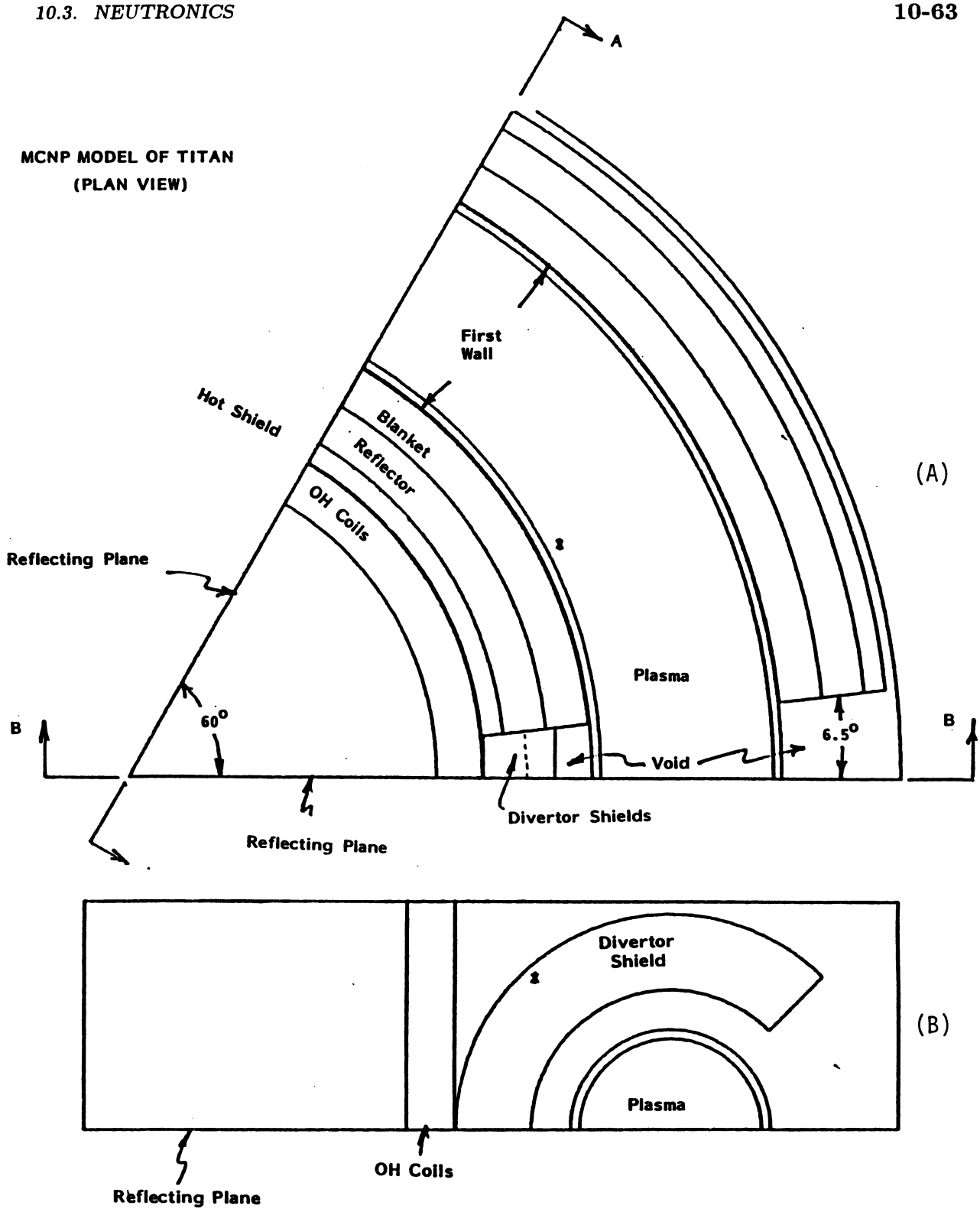

Figure 10.3-3. Plan view (A) and elevation view (B) of the 3-D MCNP model for the TITAN-I FPC.

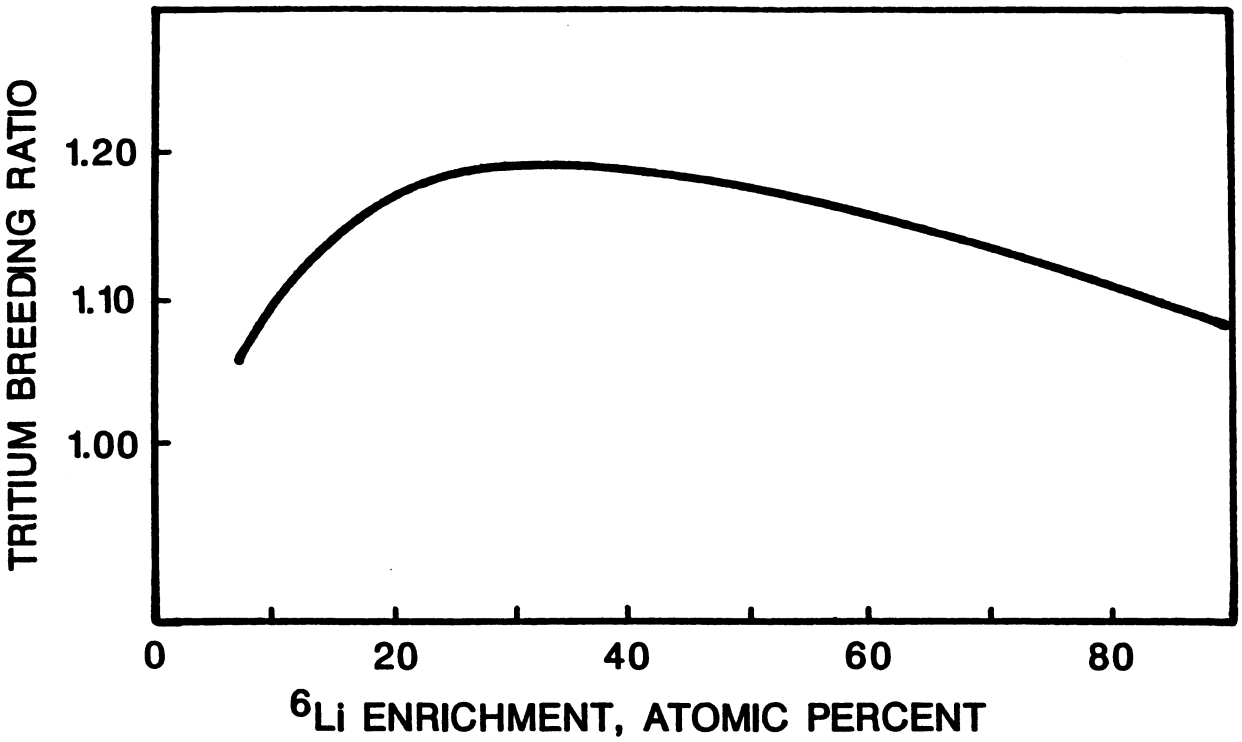

Figure 10.3-4. Tritium-breeding ratio from MCNP calculations for the TITAN-I design as a function of ^{6}Li enrichment in lithium.

of operation, while the second region is 35-cm thick and is replaced after 4 FPY. The maximum fast-neutron fluence at the OH magnet in the inboard region, calculated from the 3-D model, was found to be 1.6×10^{27} n/m^2; this fluence is well below the assumed lifetime limit for the spinel insulator. A detailed description of the neutronics performance of the divertor module is given in Section 11.7.

The TBRs found for the 3-D models are summarized in Table 10.3-IV and depicted in Figure 10.3-4 as a function of ^{6}Li enrichment in lithium. The net TBR was found to be 1.18 for the reference design, where the ^{6}Li enrichment is 30%; about 0.96 of the tritium breeding is contributed by the ^{6}Li(n,α)T reaction.

The ^{6}Li enrichment of 30% was selected for the reference design because of the improved afterheat, good magnet protection performance, and acceptable enrichment cost. Future optimization of the TITAN-I design may be possible by considering different low-activation reflector materials to reduce cost and by more detailed trade-off studies between ^{6}Li enrichment, cost, annual replacement mass, and waste-disposal concerns.

Table 10.3-IV.

TRITIUM-BREEDING RATIOS IN THE TITAN-I DESIGN CALCULATED BY MCNP

Region	From ^{6}Li	From ^{7}Li	TOTAL TBR
CASE 1 – 30% ^{6}Li[a]			
First wall	0.0106	0.0068	0.017
Blanket	0.5355	0.1735	0.709
Hot shield (1st zone)	0.3764	0.0404	0.417
Hot shield (2nd zone)	0.0186	0.0005	0.019
Divertor shields	0.0216	0.0011	0.023
TOTAL	0.962	0.222	1.184
CASE 2 – 90% ^{6}Li			
First wall	0.0150	0.0010	0.016
Blanket	0.6306	0.0245	0.655
Hot shield (1st zone)	0.3626	0.0058	0.368
Hot shield (2nd zone)	0.0176	0.0001	0.018
Divertor shields	0.0295	0.0001	0.030
TOTAL	1.055	0.032	1.087
CASE 3 – Natural Li			
First wall	0.0067	0.0091	0.016
Blanket	0.3800	0.2380	0.618
Hot shield (1st zone)	0.3420	0.0580	0.400
Hot shield (2nd zone)	0.0144	0.0007	0.015
Divertor shields	0.0105	0.0013	0.012
TOTAL	0.754	0.307	1.061

(*a*) Reference TITAN-I design.

10.4. THERMAL AND STRUCTURAL DESIGN

The thermal-hydraulic design is intimately coupled to the power conversion scheme, the safety design of the reactor, the configuration, and the neutronics aspects of the first wall and blanket. Power-cycle efficiency is affected by the coolant inlet and exit temperatures. Safety-design requirements dictate that the structural temperature, temperature gradient, coolant pressure, and pressure drop be low enough that the design limits on temperature, pumping power, and material stress are not exceeded. The thermal-hydraulic design should also facilitate the removal of decay afterheat under accident conditions and be favorable to blanket energy multiplication and tritium breeding.

A high thermal conductivity and a high heat capacity are among the desirable properties of a coolant. Liquid metals are generally excellent coolants in this regard, because of their high thermal conductivity and the high boiling point, as compared to water. Therefore, the FPC thermal energy can be removed at a much higher temperature, resulting in a higher thermal-energy conversion efficiency. The removal of thermal energy at high temperatures is also possible with gas coolants such as helium. However, high operating pressure and large pumping power are necessary because of low density and low specific-heat capacity of gas coolants.

The TITAN-I FPC is cooled by liquid lithium. Several other studies have also considered liquid lithium as coolant for fusion reactors [98 - 100]. The eutectic mixture of lithium and lead, LiPb, has been proposed [101] and used in reactor studies such as MARS [102] and CRFPR [103]; but fusion neutrons produce polonium radionuclide from the lead. One of the issues for liquid-metal coolants in fusion reactors is the MHD-induced pressure drop, a consequence of the high electrical conductivity of the coolant. In an RFP fusion reactor such as TITAN, the toroidal magnetic field at the first wall is quite small, thus the MHD pressure drop can be kept low by aligning the coolant channels with the poloidal field.

This section summarizes the thermal-hydraulic design of the TITAN-I FPC, including the thermal analysis of the first wall, blanket, and shield (Sections 10.4.2 and 10.4.3), the MHD-induced pressure drops, and the required pumping powers (Section 10.4.4). The thermal-hydraulic design window for lithium-cooled, high-power-density RFP reactors is discussed in Section 10.4.5, and a detailed thermal and structural analysis of the first wall and blanket using finite-element techniques is given in Section 10.4.6. The coolant-circulation pumps are reviewed in Section 10.4.7, and the impact of high-velocity coolant on the erosion of the first wall is discussed in Section 10.4.8.

10.4.1. Coolant-Channel Configuration

The geometry, size, and configuration of the coolant channels are important parameters in thermal-hydraulic design. Orientation of the coolant channels with respect to the magnetic field greatly affects the MHD pressure drop. Channel geometry and size affect the coolant velocity and heat transfer. In the RFP confinement concept, the dominant magnetic field at the plasma edge (or first wall) is the poloidal field. The coolant channels in the first wall and blanket are, therefore, aligned with the poloidal field in order to minimize the induced MHD effects.

Table 10.4-I summarizes the heat load on the TITAN-I FPC components. The first wall is exposed to a radiation heat flux of about 4.6 MW/m^2 in the TITAN-I design, while in the blanket and hot shield the heat load is mainly from the volumetric nuclear heating. Tubular coolant channels with circular cross section are suitable for the first wall, since a circular tube has the best heat-transfer capability (highest Nusselt number) and highest strength. In addition, tubes are easy to manufacture with small tolerances on size and wall thickness. The requirements of heat-transfer capability and material strength for the blanket-coolant channels are less stringent because of the much smaller heat load and low coolant velocity.

Figures 10.4-1 and 10.4-2 show the elevation view and horizontal (midplane) cross section of the coolant channels used in the TITAN-I FPC. The first wall is a bank of circular coolant tubes. To adjust for the shorter toroidal length on the inboard as compared to the outboard side, the first-wall tubes slightly overlap on the inboard side of the torus, as is shown in Figure 10.4-2. Therefore, two sets of coolant tubes are used with one set having a slightly larger poloidal diameter. The inside diameter and wall thickness of the first-wall coolant tubes are, respectively, 8 and 1.25 mm. The inside diameter of the first-wall tubes reflects a compromise between the total number of coolant tubes and the heat-transfer coefficient; reducing the diameter increases the heat-transfer coefficient, but it also increases the number of tubes and may result in a lower reliability (more likelihood of tube failure). The tube wall thickness of 1.25 mm includes a 0.25-mm allowance for erosion even though the sputtering erosion of the first wall is estimated to be negligible (Section 5).

The blanket- and shield-coolant channels are designed with the consideration of heat transfer, blanket energy multiplication, tritium breeding, and shielding requirements. The TITAN-I blanket is configured as an integrated blanket coil (IBC) [104] and serves as the toroidal-field coil and part of the oscillating-field current-drive coils. The heat-transfer requirements of the blanket and shield are not as stringent as for the first-wall-

Table 10.4-I.

HEAT LOAD (MW) ON TITAN-I FPC COMPONENTS

Power to First Wall	
Surface heating	462.2
Nuclear heating	
Structure	115.9
Coolant	118.1
Pumping power[a]	37.7
Total	735.9
Power to IBC	
Nuclear heating	
Structure	373.3
Coolant	870.1
OFCD joule heating[b]	17.0
TF-IBC joule heating	25.6
Pumping power[a]	6.0
Total[c]	1292.0
Power to Hot Shield	
Nuclear heating	
Structure	458.9
Coolant	247.3
Pumping power[a]	3.0
Total	709.2

(*a*) A pump efficiency of 90% is assumed.

(*b*) Joule heating in the IBC, which is also the toroidal-field driver coil of the OFCD system, and from eddy currents (1 MW).

(*c*) Excluding 168.8 MW which is deposited in the divertor IBC.

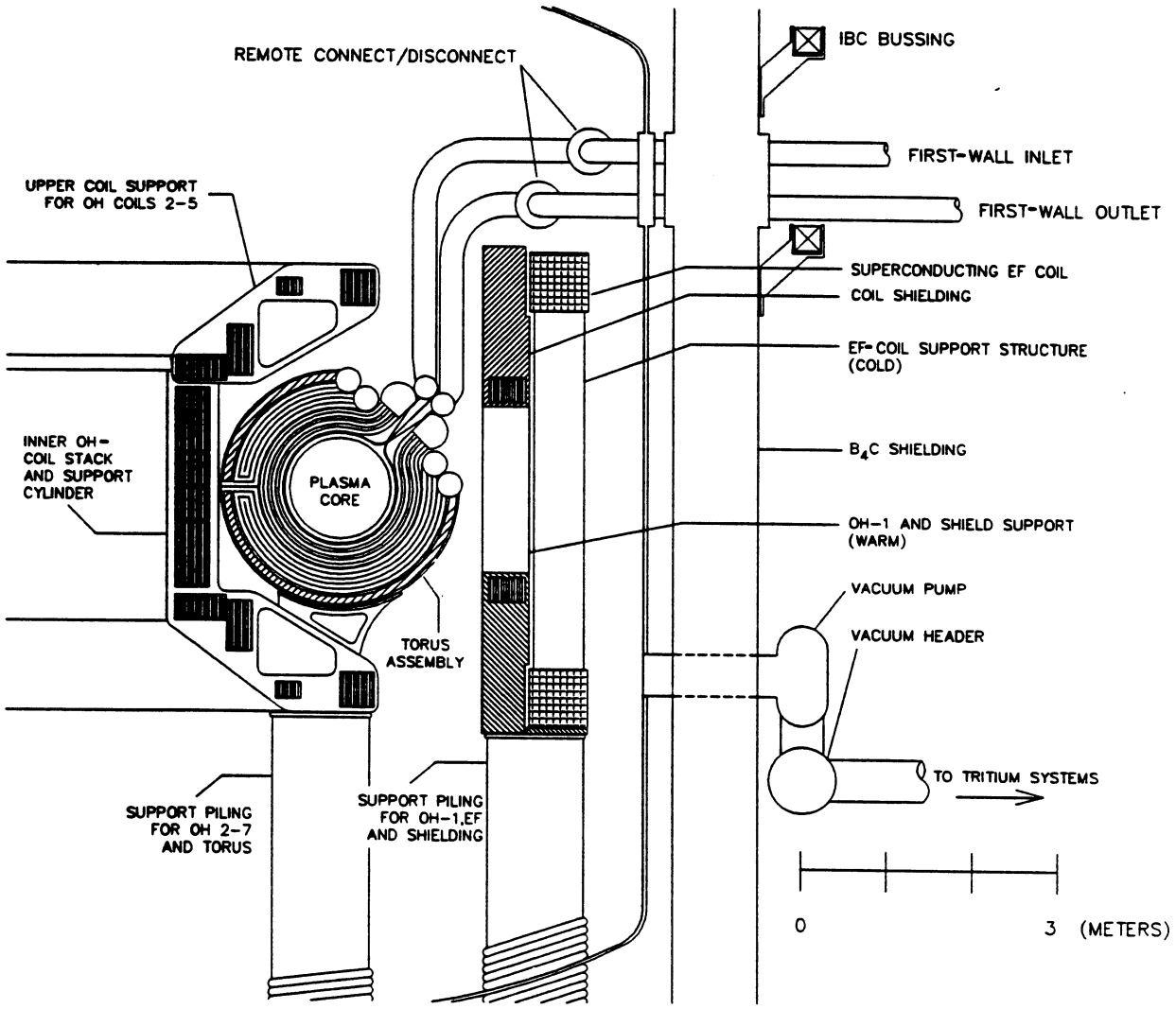

Figure 10.4-1. Elevation view of the TITAN-I first-wall and blanket-coolant channels.

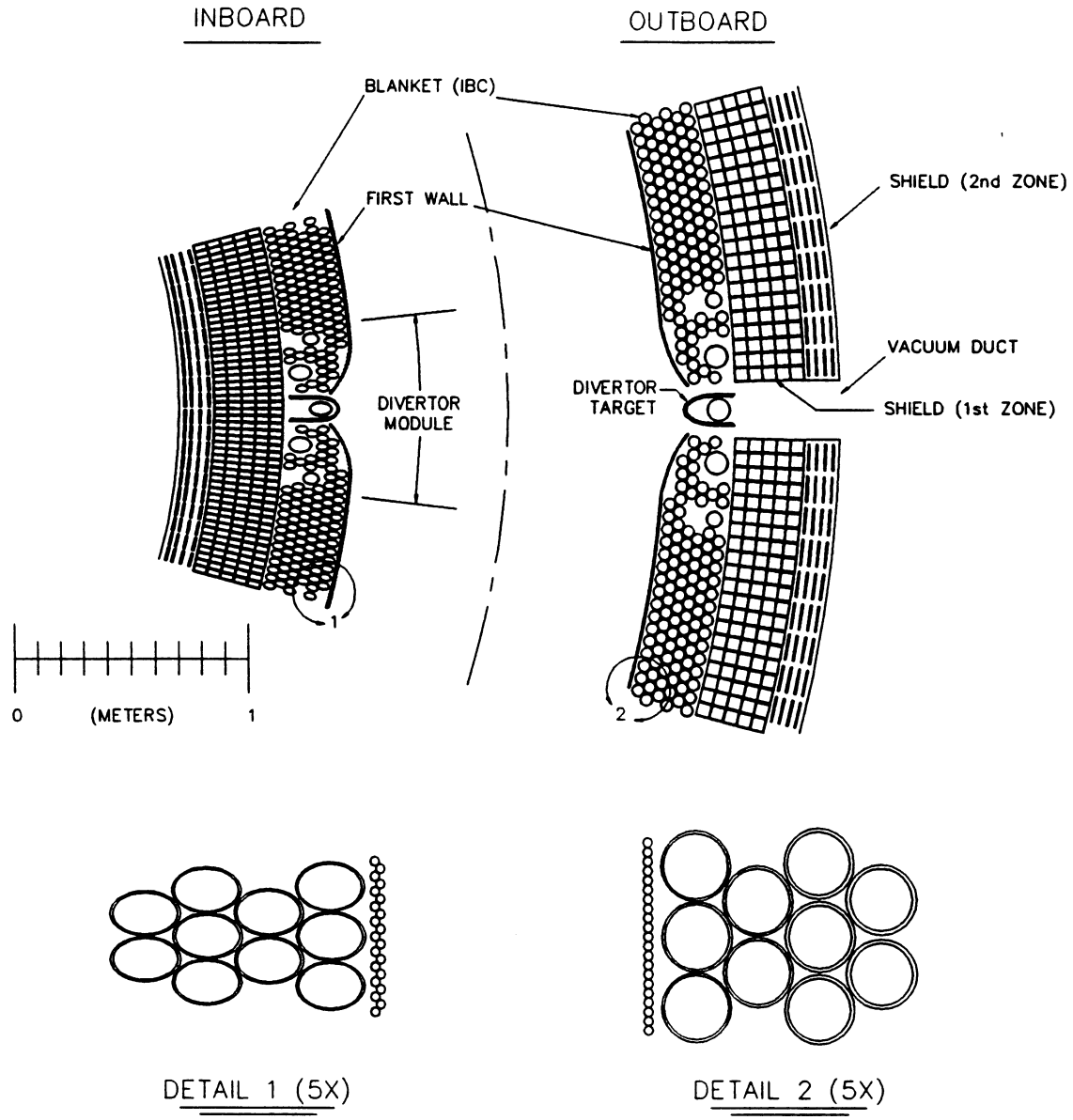

Figure 10.4-2. Horizental, midplane cross section of the TITAN-I fusion power core through blanket and divertor regions.

coolant channels, and there is a greater margin for varying the size, shape, and wall thickness of the coolant channels. The final design of the blanket and shield is based on design iterations among thermal-hydraulic design, structural analysis, neutronics, and IBC electrical engineering aspects.

The overall thickness of the blanket and shield is 75 cm. The IBC zone is 28-cm wide, is located 1 cm behind the first wall, and consists of 6 rows of tubular coolant channels. Each coolant channel has an inside diameter of 4.75 cm and a wall thickness of 2.5 mm. The primary reason for using tubular coolant channels for the IBC zone, which results in more voids, is to reduce the number of load-bearing welded joints near the plasma. The IBC-coolant channels have varying cross sections (Figure 10.4-2) in order to minimize the void fraction of this zone. The resulting IBC zone consists of 18% structure, 72% lithium, and 10% void by volume.

The hot shield is located 1 cm behind the IBC, is 45-cm thick, and has two zones. The first zone is 30-cm thick and consists of 5 rows of square coolant channels with outer dimensions of 6 cm and a wall thickness of 5 mm. The inside corners are rounded and have the radius-to-wall thickness ratio of unity. The structure volume fraction is 30%, the coolant volume fraction is 70%, and there is no void. The second zone of the hot shield is 15-cm thick and consists of 4 rows of rectangular channels with thick walls to increase the structure volume fraction in this zone. The structure volume fraction is 90% and the coolant volume fraction is 10%. The channels have outer dimensions of 11.25 cm by 3.75 cm and a wall thickness of 16.25 mm.

Figure 10.4-3 shows a detailed cross section of the TITAN-I FPC including the manifolds, inlet and outlet headers, coolant channels, and the coolant flow directions. The coolant flow in both first wall and blanket are single pass in the poloidal direction. In the hot shield however, the poloidal flow circuit is double pass, as is illustrated in Figure 10.4-3. Lithium flows in through the first three square channels of the hot shield, makes a 180° turn at the inboard side, and exits through the last two square channels and the rectangular channels of the hot shield. Because of this double-pass flow pattern, the hot shield can be constructed as two separate units. During the annual maintenance, the top half of the shield will be removed so that the torus assembly (including the first wall, IBC, and divertor modules) can be replaced. The estimated lifetime of the shield is 4 FPY and, therefore, this portion can be reinstalled after the completion of the annual maintenance.

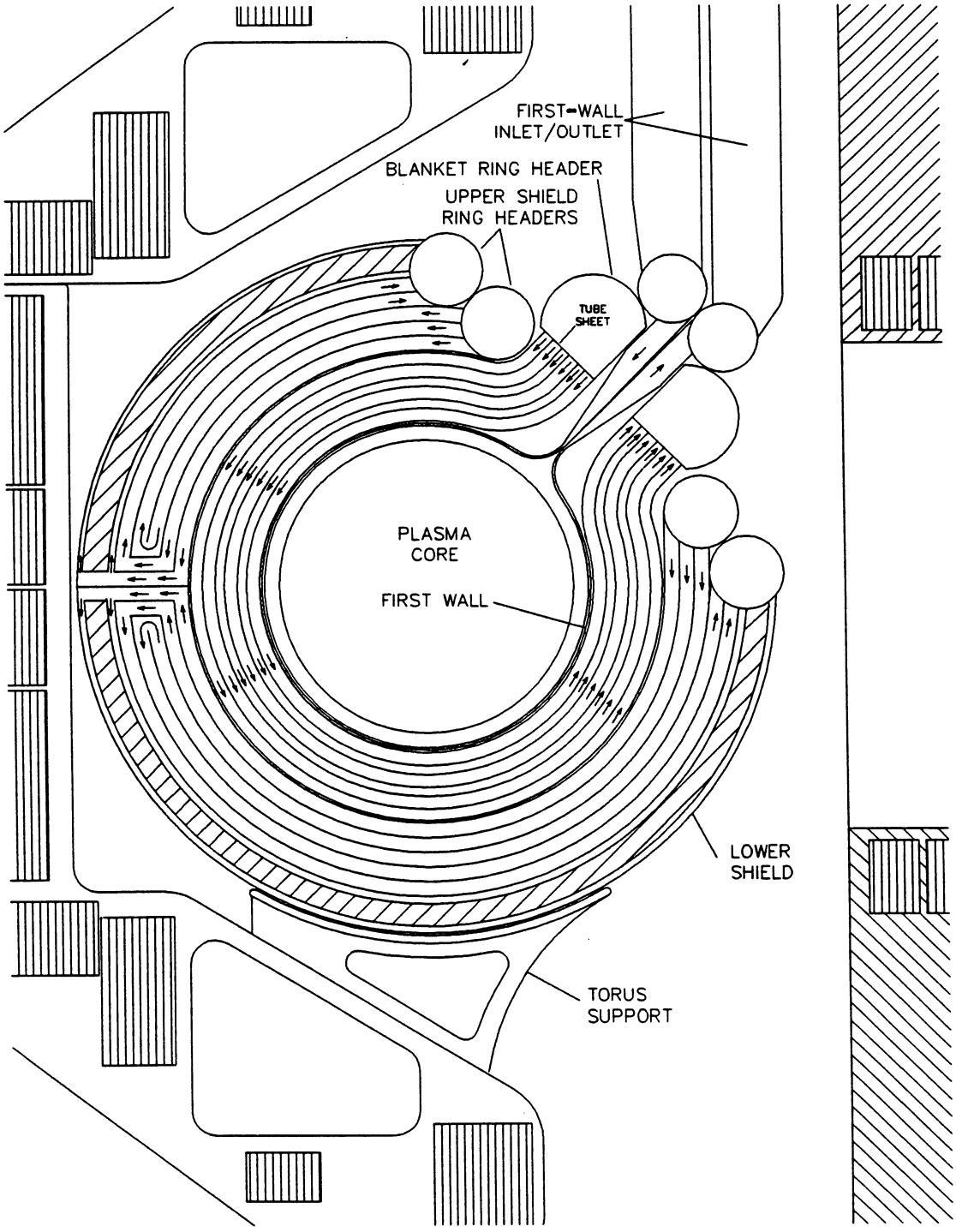

Figure 10.4-3. Elevation view of the TITAN-I first-wall and blanket-coolant channels showing the manifolds, headers, and coolant flow direction.

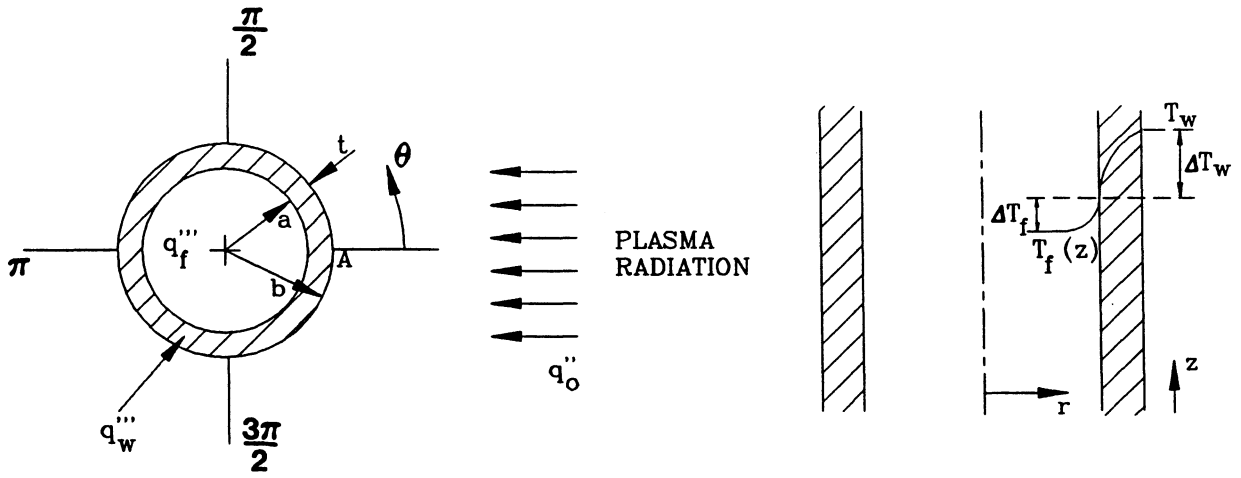

Figure 10.4-4. The thermal-analysis model of the first-wall-coolant tubes.

10.4.2. Thermal Analysis of the First Wall

Analytical estimates of the thermal performance of the first-wall tubes have been made in order to define the thermal-hydraulic design window. These analyses were then verified by finite-element analysis (Section 10.4.6). Figure 10.4-4 shows the notation for the dimensions, heat fluxes, volumetric heating rates, and temperature drops in the first-wall-coolant tubes. The inner radius of the tube is denoted by a, the outer radius by b, and the wall thickness by $t = b - a$. The heat load comprises radiation heat flux (q''_o) and volumetric nuclear heating in the wall (q'''_w) and coolant (q'''_f). The radiation heat flux on the plasma-facing surface of a first-wall-coolant tube is represented by a cosine distribution, with a maximum at $\theta = 0$ denoted as point A in Figure 10.4-4.

The heat conduction along the axis of the tube can be neglected in the analysis since the temperature gradient in the axial direction is much smaller than that along the radial or circumferential (θ) directions. Furthermore, because of the large aspect ratio of the TITAN-I design, the surface heat flux and volumetric heating rates do not vary appreciably along the axis of the coolant tube. The ratio of peak-to-average neutron wall loading (and volumetric heating rate) is estimated to be $\sim 8\%$ (Section 3) and the variation in the surface heat flux is expected to be smaller. The wall temperature can,

therefore, be expressed as

$$T_w(\theta, z) = T_f(z) + \Delta T_f(\theta) + \Delta T_w(\theta) , \qquad (10.4\text{-}1)$$

where T_w is the wall temperature, ΔT_f is the film temperature drop, and ΔT_w is the temperature drop across the wall. The coolant temperature at point z along the tube axis, $T_f(z)$, can be calculated from energy balance equation to be

$$T_f(z) = T_{in} + \frac{(2/\pi)\, b\, q''_o + a^2\, q'''_f + (b^2 - a^2)\, q'''_w}{a^2\, U\, \rho_f\, c_p}\, z , \qquad (10.4\text{-}2)$$

where T_{in} is the inlet temperature of the coolant, L is tube length, U is the mean coolant velocity, and ρ_f and c_p are, respectively, the density and specific heat capacity of the coolant.

One of the main constraints on the thermal-hydraulic design is the maximum temperature of the structure. Examination of Equation 10.4-1 shows that the maximum wall temperature occurs at the coolant exit point

$$T_{w,Max} = T_{ex} + (\Delta T_f + \Delta T_w)_{Max} , \qquad (10.4\text{-}3)$$

where T_{ex} is the coolant exit temperature, $T_{ex} = T_f(z = L)$, and L is the length of the tube.

A complete 2-D solution of the temperature field in the tube wall and in the fluid would adequately describe the temperature distribution, but such an approach is not useful for parametric surveys of the thermal-hydraulic design window. Because of the strong variation of the heat flux on the first-wall tubes and the resulting circumferentially varying Nusselt number, a 2-D analysis of the coolant temperature distribution has been performed for laminar flow; for the turbulent-flow regime, an empirical correlation for the Nusselt number with a correction for nonuniform surface heat flux is used. The first-wall tubes are thin, however, and the temperature drop across the tube wall, ΔT_w, can be estimated accurately by assuming that the heat conduction is local and one dimensional in the radial direction.

At any radial position r and any circumferential angle θ around the first-wall tube, the temperature profile is

$$T(r) = T_{wi} + \frac{q'''_w\, b^2}{2k_w} \ln\left(\frac{r}{a}\right) - \frac{q'''_w}{4k_w}(r^2 - a^2) + \frac{q''_o\, cos(\theta)\, b}{k_w} \ln\left(\frac{r}{a}\right) , \qquad (10.4\text{-}4)$$

where T_{wi} is the temperature at the inner surface of the wall and k_w is the thermal conductivity of the wall material. The maximum wall temperature drop, therefore, occurs at point A ($\theta = 0$) of Figure 10.4-4, where the heat flux is maximum:

$$\Delta T_{w,Max} = \frac{q'''_w b^2}{2k_w} \ln\left(\frac{b}{a}\right) - \frac{q'''_w}{4k_w}(b^2 - a^2) + \frac{q''_o b}{k_w} \ln\left(\frac{b}{a}\right) . \quad (10.4\text{-}5)$$

10.4.2.1. Laminar heat transfer in the first-wall tubes

For a laminar coolant flow in the first-wall tubes, the film temperature drop is calculated from the 2-D solution of the convection equation

$$\frac{\partial^2 T}{\partial r^2} + \frac{1}{r}\frac{\partial T}{\partial r} + \frac{1}{r^2}\frac{\partial^2 T}{\partial \theta^2} = \frac{u(r)}{\alpha}\frac{dT}{dz} , \quad (10.4\text{-}6)$$

where $\alpha = k_f/(\rho_f c_p)$ is the thermal diffusivity of the coolant and $u(r)$ is the fully developed, laminar velocity profile of the coolant. To account for the flattening of the velocity profile caused by the perpendicular magnetic field, a power velocity profile for $u(r)$ is assumed

$$u(r) = U\left(\frac{m+2}{m}\right)\left[1 - \left(\frac{r}{a}\right)^m\right] , \quad (10.4\text{-}7)$$

where U is the mean coolant velocity

$$U = \frac{2}{a^2}\int_0^a r\, u(r)\, dr . \quad (10.4\text{-}8)$$

The exponent m would be large for a flat velocity profile and $m = 2$ for a parabolic profile.

The boundary and symmetry conditions for Equation 10.4-6 are

$$k_f \left.\frac{\partial T}{\partial r}\right|_{r=a} = q''(\theta)$$

$$\left.\frac{\partial T}{\partial \theta}\right|_{\theta=0} = \left.\frac{\partial T}{\partial \theta}\right|_{\theta=\pi} = 0 \quad (10.4\text{-}9)$$

and the surface heat flux, $q''(\theta)$, is given by

$$q''(\theta) = \begin{cases} q''_{NH} + q''_o(\theta) & 3\pi/2 \le \theta \le \pi/2 \\ q''_{NH} & \pi/2 \le \theta \le 3\pi/2 \end{cases} \quad (10.4\text{-}10)$$

where q''_{NH} is the average heat flux at the interface between the tube wall and the coolant (from nuclear heating in the tube wall):

$$q''_{NH} = \frac{(b^2 - a^2)\, q'''_w}{2a} . \qquad (10.4\text{-}11)$$

Equation 10.4-6 can be solved by the method of separation of variables [105], and the film temperature drop, ΔT_f, is found to be

$$\Delta T_f(\theta) = f(m)\frac{a}{\pi k_f}\int_0^{2\pi} q''(\omega)d\omega - \frac{a}{\pi k_f}\int_0^{2\pi} q''(\omega)\,\ln\left[2sin\left(\frac{\theta-\omega}{2}\right)\right] d\omega , \qquad (10.4\text{-}12)$$

where

$$f(m) = \frac{(m+2)^2 - 4}{4m(m+2)} - \frac{(m+2)^2}{m^2}\left[\frac{m}{8(m+4)} - \frac{m+2}{(m+1)(m+2)^3}\right] . \qquad (10.4\text{-}13)$$

Using Equation 10.4-12, the Nusselt number, $Nu(\theta)$, can be determined:

$$Nu(\theta) = \frac{2a\, q''(\theta)}{k_f\, \Delta T_f(\theta)} , \qquad (10.4\text{-}14)$$

which shows that the Nusselt number varies along the circumference of the tube. For a parabolic velocity profile ($m = 2$) and a uniform heat flux, Equations 10.4-12 and 10.4-14 result in $Nu = 48/11 = 4.36$. When the velocity profile is flat ($m \to \infty$) and the heat flux is uniform, $Nu = 8$, which is the well-known result for the slug flow.

When the surface heat flux is not uniform, the Nusselt number and film temperature drop vary along the circumference of the tube. Figure 10.4-5 shows this variation, as computed from Equations 10.4-12 and 10.4-14 for the case of $q''_o = 4.6\,\mathrm{MW/m^2}$ and $q''_{NH} = 0.12\,\mathrm{MW/m^2}$. The Nusselt number is positive for θ from 0 to about 90° as the surface temperature equalizes with the average coolant temperature. In the vicinity of $\theta = 90°$, the Nusselt number is infinite, reflecting that ΔT_f is zero at this point. The Nusselt number then become negative because the average coolant temperature is higher than the wall temperature.

The maximum film temperature drop occurs at $\theta = 0$ (point A in Figure 10.4-4), where $Nu \simeq 3.0$ instead of the average value of 7.1, as has been calculated for uniform heat flux and transverse Hartmann number greater than 100 [106]. This lower value of the Nusselt number should be used in determining the film temperature drop; otherwise the maximum wall temperature would be seriously underestimated, considering that the maximum heat flux also occurs at this point.

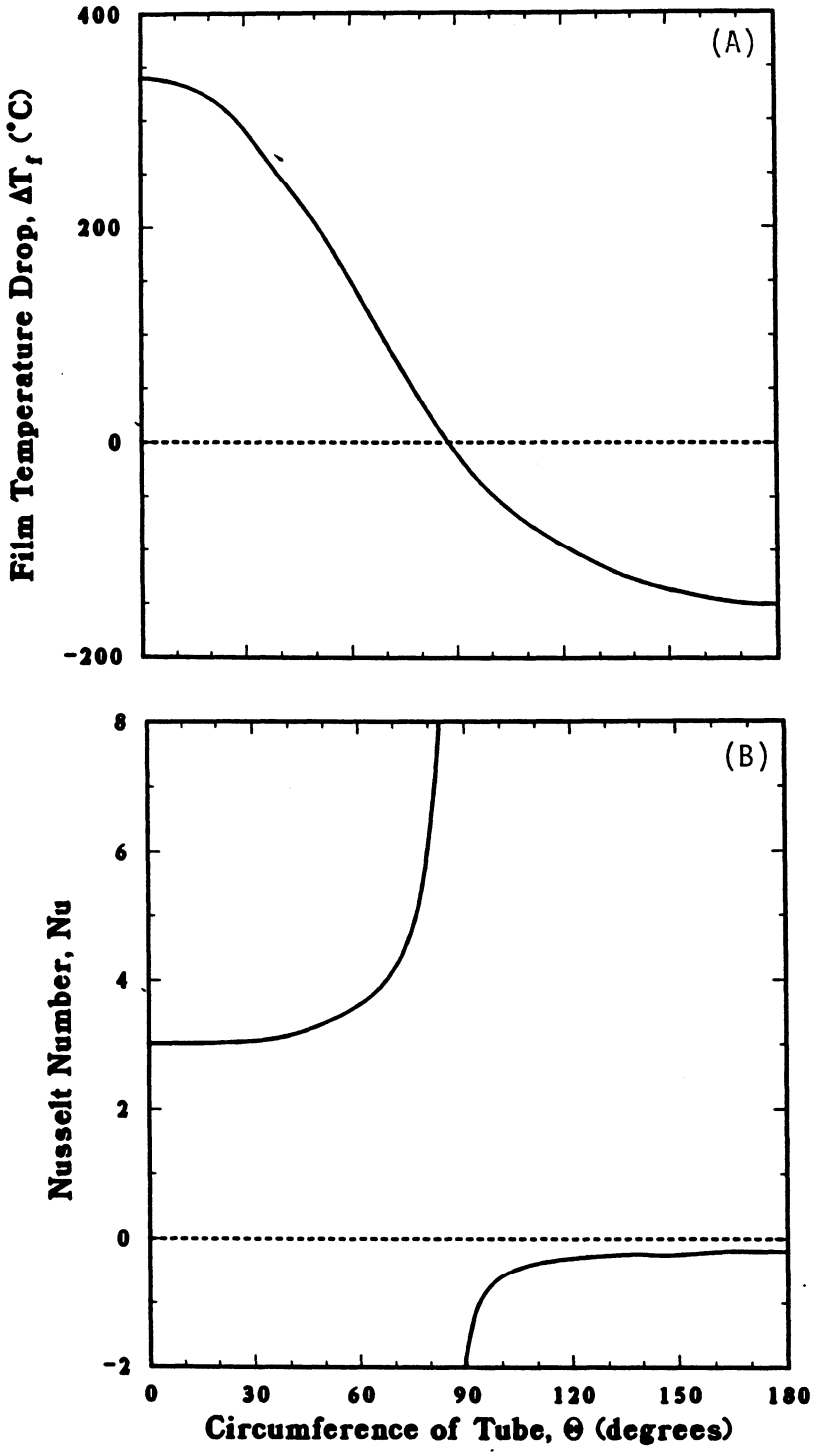

Figure 10.4-5. Variation of the Nusselt number (A) and the film temperature drop (B) around the circumference of the coolant tube for $q''_o = 4.6\,\mathrm{MW/m^2}$ and $q''_{NH} = 0.12\,\mathrm{MW/m^2}$.

The effect of the nonuniform surface heat flux can be reduced or eliminated by utilizing the swirl flow of the coolant in the tube [107] which can be produced by helical vanes laying inside the tube. The curvature of the tube also introduces secondary flow patterns similar to swirl flow [108]. However, the effect of the magnetic field on the swirl flow has not been investigated and, therefore, the swirl-flow patterns have not been used for the TITAN-I design.

10.4.2.2. Turbulent heat transfer in the first-wall tubes

For a given size for the first-wall tubes, the maximum wall temperature constraint would result in a maximum limit on the surface heat flux. A higher surface heat flux can be accommodated by using a turbulent coolant flow, which is accompanied by a higher Nusselt number. The magnetic field, generally, tends to suppress turbulence in the flow of an electrically conducting fluid, and the onset of turbulence would occur at higher Reynolds numbers (for non-MHD pipe flow, onset of turbulence occurs at Reynolds numbers in excess of 2300). The Reynolds number is defined as $Re = \rho_f U\, d_h/\eta_f$, where d_h is the hydraulic diameter of the channel and η_f is the viscosity of the coolant.

Experimental data on MHD turbulent flow are limited. Some experimental data in the presence of a transverse magnetic field are reported [109 - 111] with Hartmann numbers ranging up to 1300. Experimental data in the presence of longitudinal magnetic field are also reported [112,113], but the Hartmann number was low (up to about 150). The onset of turbulence was detected from pressure fluctuations and skin friction data, and it has been shown that the onset of turbulence is delayed by both the transverse and longitudinal fields, with the effect of the transverse field being stronger. The transition Reynolds number, Re_t, corresponding to the onset of the turbulence, was proposed to be directly proportional to the Hartmann number as [114]

$$Re_t \geq \begin{cases} C_1 Ha_\perp & \text{for perpendicular field} \\ \\ C_2 Ha_\parallel & \text{for parallel field}\,, \end{cases} \tag{10.4-15}$$

where $Ha_\perp$ and $Ha_\parallel$ are, respectively, the transverse and longitudinal Hartmann numbers and C_1 and C_2 are constants. Hoffman [114] suggested $C_1 = 500$ and $C_2 = 60$. The data from Gardner and Lykoudis [109], which extends to $Ha_\perp = 1300$, result in $C_1 \leq 250$, while the data from Globe [112] suggest $C_2 \simeq 40$. Lykoudis [115] suggested a value of 236 for C_1 and Branover *et al.* [116] suggested a value of 155 for circular tubes and square ducts.

An interesting aspect of Equation 10.4-15 is that the turbulent velocity, v_t, is independent of the channel size and is solely determined by the magnetic field strength and the coolant properties

$$v_t \geq \begin{cases} C_1 B_\perp (\sqrt{\sigma_f \eta_f}/\rho_f) \\ \\ C_2 B_\parallel (\sqrt{\sigma_f \eta_f}/\rho_f)\,, \end{cases} \tag{10.4-16}$$

where $B_\perp$ and $B_\parallel$ are, respectively, the perpendicular and parallel magnetic field and σ_f is the electrical conductivity of the coolant. Using the conservative values of $C_1 = 500$ and $C_2 = 60$ [114], a poloidal flow velocity of about 20 m/s is estimated for the liquid-lithium flow in the first wall of the TITAN-I design.

Few studies are available on the turbulent-flow heat transfer in liquid metals in the presence of a magnetic field. Kovner *et al.* [117] performed experiments on the effect of a longitudinal magnetic field on turbulent heat transfer in liquid-galium flow in a tube. The following empirical correlation for Nusselt number was then proposed

$$Nu = 6.5 + \frac{0.005 Pe}{1 + 1890(Ha_\parallel/Re)^{1.7}}\,, \tag{10.4-17}$$

where $Pe = Re\,Pr$ is the Peclét number and $Pr = \eta_f c_p/k_f$ is the Prandtl number. Equation 10.4-17 reduces to that for ordinary turbulent flow for $Ha_\parallel = 0$. This equation also predicts the expected effects of the magnetic field: the Nusselt number increases with increasing field strength, while for a given Re, the Nusselt number approaches the value for laminar flow as $Ha_\parallel$ increases. Conversely, for a given $Ha_\parallel$, the Nusselt number approaches its value for standard liquid-metal correlations without magnetic field as Re is increased. Even though Equation 10.4-17 is based on experimental data up to $Ha_\parallel = 550$, it is expected to hold beyond this range.

The experimental data from Gardner and Lykoudis [118], with transverse magnetic field and Hartmann number ranging up to $Ha_\perp = 1300$, show similar dependence. Krasilnikov [119] performed a numerical study on turbulent-flow heat transfer in a channel between two parallel plates in the presence of a transverse magnetic field. His results also show similar effects of the magnetic field on turbulent-flow heat transfer. Branover *et al.* [116] reported experimental evidence to suggest that under certain conditions the magnetic field may increase turbulence intensity in an anisotropic fashion and, as a result, the total thermal diffusivity will be greatly increased.

For the TITAN-I design, Equation 10.4-17 is used. Figure 10.4-6 shows the variation of the Nusselt number with Peclét number for $B = 0$, $Ha_\parallel = 1000$, and $Ha_\parallel = 3040$ (the

expected $Ha_{||}$ in TITAN-I first wall). The range of the experimental data is also shown. It is seen that the flow remains laminar up to large values of Peclét number as the Hartmann number is increased.

The nonuniform circumferential heat flux on the first-wall tubes will reduce the turbulent Nusselt number at the point of highest heat flux, as has been shown before for the case of laminar flow (Section 10.4.2.1). Until further data become available, the Nu given by Equation 10.4-17 is reduced by a factor of 2 for the TITAN-I design to account for this nonuniform circumferential heat flux.

10.4.3. Thermal Analyses of the Blanket and Shield

Thermal analyses of the blanket and shield are simpler than for the first wall. No radiation heat flux exists and the volumetric heating rates in individual coolant channels can be taken as uniform because the gradient of the volumetric heating across each channel is small. Therefore, the surface heat flux incident on the coolant will be uniform, and the Nusselt number can be assumed to be constant.

The TITAN-I IBC is made of tubular channels while the hot shield consists of rectangular coolant channels to minimize the void fraction. Since the volumetric heating rate decreases away from the first wall, thermal analysis for each row of coolant channels is performed separately. However, the analysis is similar for all types of coolant channels.

An outline of the thermal analysis for both the tubular blanket channels (similar to those of Figure 10.4-4) and for square channels (Figure 10.4-7) is given below. From the desired coolant inlet (T_{in}) and outlet (T_{ex}) temperatures, the average coolant velocity is obtained by energy balance.

$$U = \frac{(b^2 - a^2)\, q'''_w + a^2\, q'''_f}{a^2\, \rho_f\, c_p\, (T_{ex} - T_{in})}\, L\,, \tag{10.4-18}$$

where L is the length of the channel and $b = a + t$. The maximum wall temperature, as for the first wall, occurs at the exit point of the coolant:

$$T_{w,Max} = T_{ex} + \Delta T_f + \Delta T_w\,. \tag{10.4-19}$$

The film temperature drop, ΔT_f, is given by

$$\Delta T_f = \frac{(b^2 - a^2)\, q'''_w}{Nu\; k_f}\,. \tag{10.4-20}$$

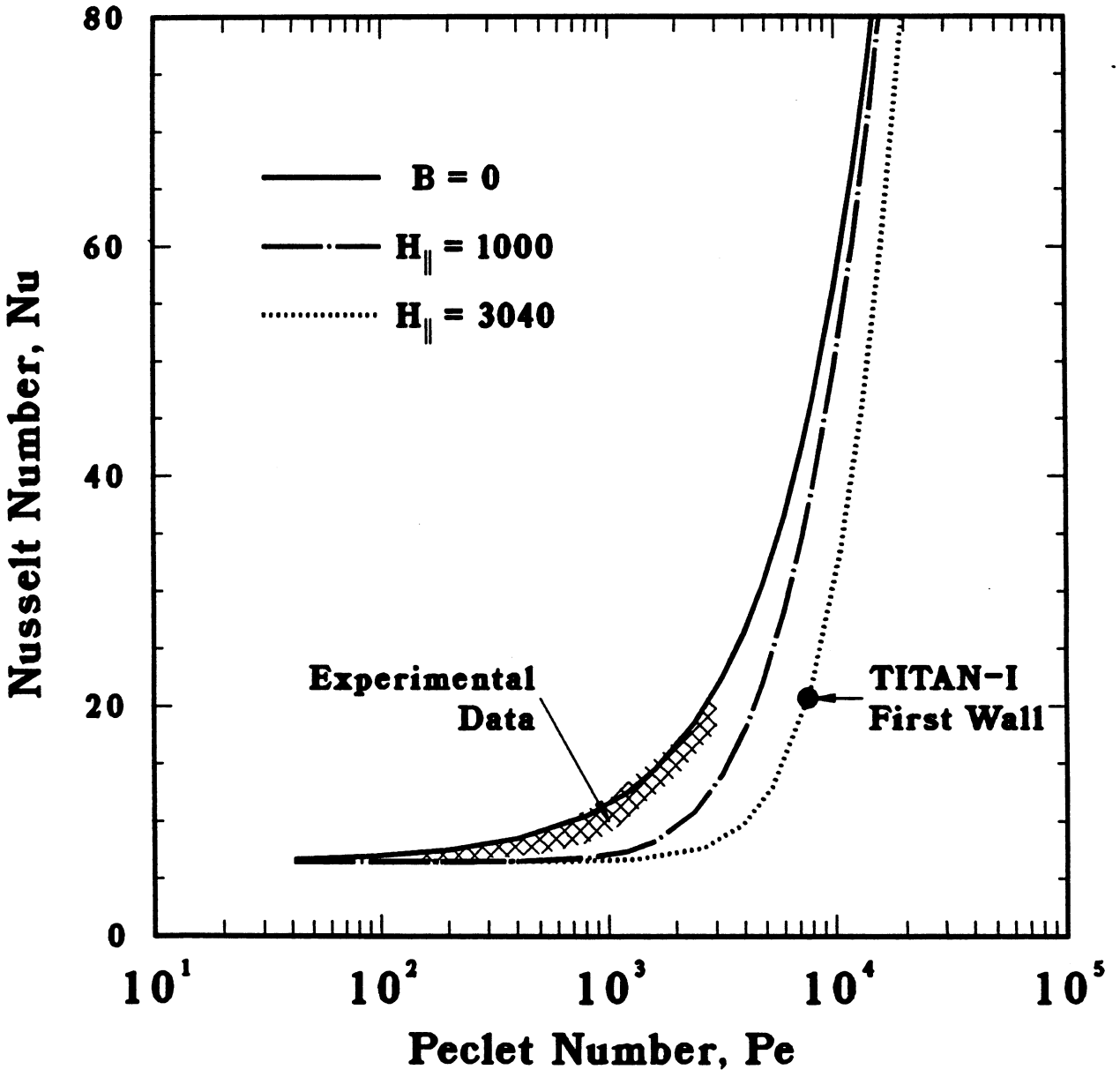

Figure 10.4-6. Variation of the Nusselt number, Nu, with the Peclét number, Pe, for turbulent flow as predicted by Equation 10.4-17. The range of experimental data as well as the operating point of the TITAN-I first wall are also shown. The Nusselt number from this graph should be halved to account for nonuniform heat flux on the TITAN-I first wall.

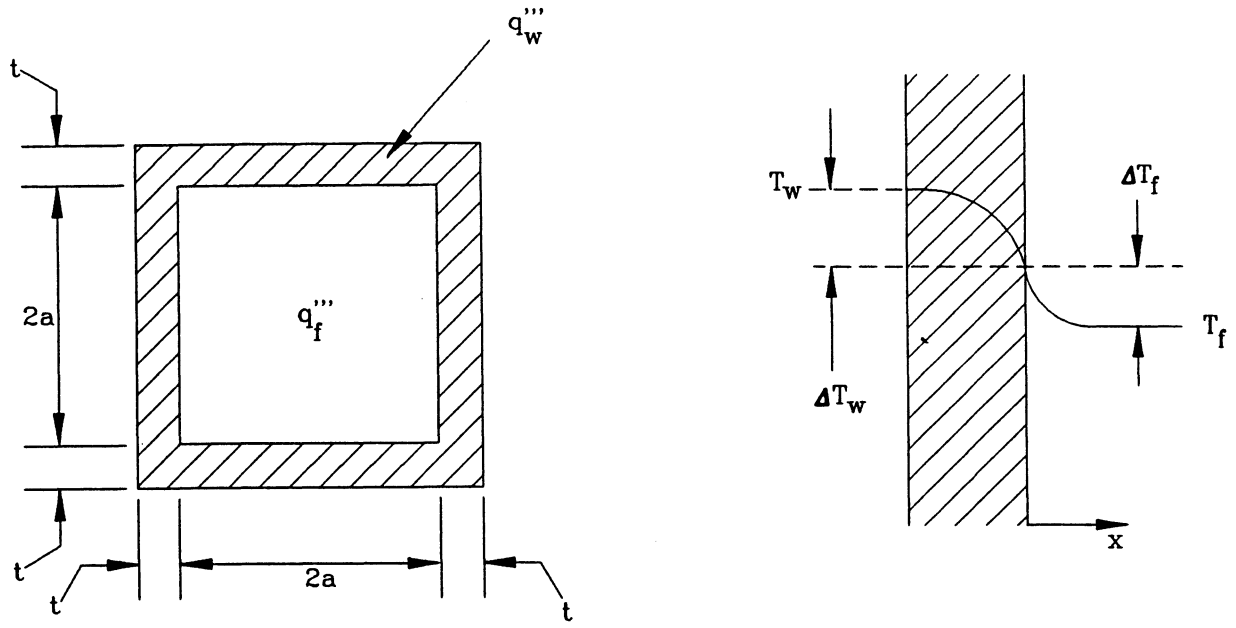

Figure 10.4-7. The thermal-analysis model of the hot-shield-coolant channels.

Similar expressions for U and ΔT_f can be written for rectangular shield channels. The flow is always laminar in the blanket and shield channels, and the Nusselt number for laminar flow in a square channel with constant heat flux is 3.6 in the absence of the magnetic field. In the presence of the magnetic field with perpendicular Hartmann number greater than 100, the average Nusselt number would be close to 5.5.

The temperature drop across the wall, ΔT_w, can be estimated from a 1-D heat-conduction analysis of the wall. The temperature profile would be parabolic, and the wall temperature drop would be

$$\Delta T_w = \frac{(b-a)^2 q'''_w}{2k_w} . \qquad (10.4\text{-}21)$$

At the corners, ΔT_w will be slightly higher than that given by Equation 10.4-21, but the difference would not be significant for thin walls.

10.4.4. Pressure Drop and Material Stress

A liquid metal flowing in the presence of a perpendicular magnetic field encounters a combination of pressure drops caused by the magnetic body force and friction,

$$\Delta p = \Delta p_f + \Delta p_{MHD} . \qquad (10.4\text{-}22)$$

In a straight channel, the friction pressure drop, Δp_f, is given by

$$\Delta p_f = f \frac{\rho_f U^2 L}{2 d_h}, \tag{10.4-23}$$

where U is the mean flow velocity of the coolant, L is the length of the channel, ρ_f is the density of the liquid metal, and d_h is the hydraulic diameter of the channel. The parameter f is the friction factor: for laminar flow, $f = 64/Re$; for turbulent flow, f is given as a function of Re and the surface roughness in the Moody friction-factor chart [120]. Semi-empirical equations are also available for friction pressure drop at bends, contractions, expansions, *etc.*

For a uniform straight channel in the presence of a constant, transverse magnetic field ($B_\perp$), the associated MHD pressure drop is given by [121]

$$\Delta p_{MHD} = \sigma_f U B_\perp^2 a \frac{\phi}{1+\phi} L. \tag{10.4-24}$$

For a rectangular channel, a is half the length of the inner side of the channel parallel to the magnetic field; for a circular tube, a is the inside radius. The wall-to-coolant electrical-conductance ratio, ϕ, is

$$\phi = \frac{\sigma_w t}{a \sigma_f}, \tag{10.4-25}$$

where t is the channel wall thickness and σ_w and σ_f are, respectively, the electrical conductivities of the wall material and coolant.

It is difficult to derive an analytical relationship for the MHD pressure drop in a bend, a contraction, or a channel with a varying cross section or in a varying magnetic field. Semi-empirical equations are, however, available for these cases. The MHD pressure-drop equations which appear to be best suited for the TITAN-I design are discussed below [99]. At a contraction or along the length of a channel, where the magnetic field is varying, the MHD pressure drop is estimated as

$$\Delta p = 0.2 \sigma_f U B_\perp^2 a \sqrt{\phi}. \tag{10.4-26}$$

For flow through a bend, if both legs of the bend are normal to the magnetic field, then the MHD pressure drop is zero. If one leg of the bend is normal and the other leg is parallel, the MHD pressure drop is

$$\Delta p = \sigma_f U B_\perp^2 a \sqrt{\phi}. \tag{10.4-27}$$

In order to complete the thermal-hydraulic design, pressure and thermal stresses in the coolant channels were estimated by 1-D equations (along r) for a thick-walled tube [122,123]. The radial pressure stress, σ_r^p, the hoop stress, σ_θ^p, and the equivalent pressure stress, σ_{eq}^p, are given by

$$\begin{aligned}
\sigma_r^p(r) &= \frac{a^2 p_i}{b^2 - a^2}\left(1 - \frac{b^2}{r^2}\right), \\
\sigma_\theta^p(r) &= \frac{a^2 p_i}{b^2 - a^2}\left(1 + \frac{b^2}{r^2}\right), \\
\sigma_{eq}^p(r) &= \sqrt{\frac{1}{2}\left[(\sigma_r^p - \sigma_\theta^p)^2 + (\sigma_r^p)^2 + (\sigma_\theta^p)^2\right]},
\end{aligned} \tag{10.4-28}$$

where p_i is the coolant pressure and the external pressure to the tube is assumed to be zero. The radial, σ_r^T, circumferential, σ_θ^T, and equivalent, σ_{eq}^T, thermal stresses are given by

$$\begin{aligned}
\sigma_r^T(r) &= \frac{\alpha E}{r^2}\left[\frac{r^2 - a^2}{b^2 - a^2}\int_a^b rT(r)dr - \int_a^r rT(r)dr\right], \\
\sigma_\theta^T(r) &= \frac{\alpha E}{r^2}\left[\frac{r^2 + a^2}{b^2 - a^2}\int_a^b rT(r)dr + \int_a^r rT(r)dr - r^2 T(r)\right], \\
\sigma_{eq}^T(r) &= \sqrt{\frac{1}{2}\left[(\sigma_r^T - \sigma_\theta^T)^2 + (\sigma_r^T)^2 + (\sigma_\theta^T)^2\right]},
\end{aligned} \tag{10.4-29}$$

where α is the coefficient of linear expansion and E is the Young's modulus of the tube material. Equation 10.4-4 with $\theta = 0$ is used for the temperature profile in the above equations.

For rectangular coolant channels of the shield, the thermal stress is estimated by

$$\sigma^T \simeq \frac{\alpha E\, \Delta T_w}{2(1 - \nu)}, \tag{10.4-30}$$

where ν is Poisson ratio of the wall material. It is more difficult to estimate the pressure stress in square or rectangular channels because of bending and corner effects. A rough estimate can be obtained from

$$\sigma^p \simeq \frac{a}{t} p_i . \tag{10.4-31}$$

The effect of bends and corners depends on the ratio of the side length to the wall thickness, a/t. A two-dimensional analysis of the pressure stress in square channels was

performed by using the finite-element code, ANSYS, and the results are reported in Section 10.4.6. The finite-element analysis has given the maximum stress in the coolant channel wall as a function of a/t. For the parametric survey of the thermal-hydraulic design window, the size of each square or rectangular coolant channel is chosen such that for a given coolant pressure, the ratio a/t is smaller than the maximum value that is predicted by finite-element analysis.

10.4.5. Thermal-Hydraulic Design Window

10.4.5.1. Design considerations

The first wall of the TITAN-I design intercepts an average radiation heat flux of $4.6\,MW/m^2$. In order to remove such a high heat flux, the first wall consists of small-diameter, circular tubes. Other thermal-hydraulic design features of TITAN-I are the separation of the first-wall and blanket-coolant circuits and the use of MHD turbulent-flow heat transfer to remove the high surface heat flux at the first wall. Figure 10.4-8 is a flowchart of the computer code used to perform the design calculations [124].

The objective of the calculations is to obtain a thermal-hydraulic design window based on the maximum allowable temperature and pressure stresses in the structure and pumping power. The maximum allowable temperature of the structure corresponds to a maximum value for the average coolant exit temperature for a given heat flux. The maximum allowable stress and pumping power result in minimum values for the average coolant exit temperature. Therefore, the design window for the coolant exit temperature is in between these limits. Other parameters influencing the design window are the neutron wall loading, the coolant channel size, and the coolant inlet temperature. Changing any of these parameters would alter the design window.

The input to the code includes the reactor parameters, physical properties of the coolant and structural material, coolant-channel geometry, and design constraints. For a given first-wall tube size and a given radiation heat flux on the first wall, the maximum wall temperature drop for the first-wall tube is found from Equation 10.4-5. Assuming a laminar flow, the maximum film temperature drop is then calculated from Equation 10.4-12, and the maximum-permissible coolant exit temperature for the first wall, $T_{ex,FW}$, is obtained from Equation 10.4-3. With this exit temperature, the average coolant velocity is computed from Equation 10.4-2. If $T_{ex,FW} \leq T_{in}$, or the coolant velocity is greater than or equal to the turbulent velocity, no solution for the laminar flow exists. In this case, the coolant velocity is set equal to the turbulent velocity, and the

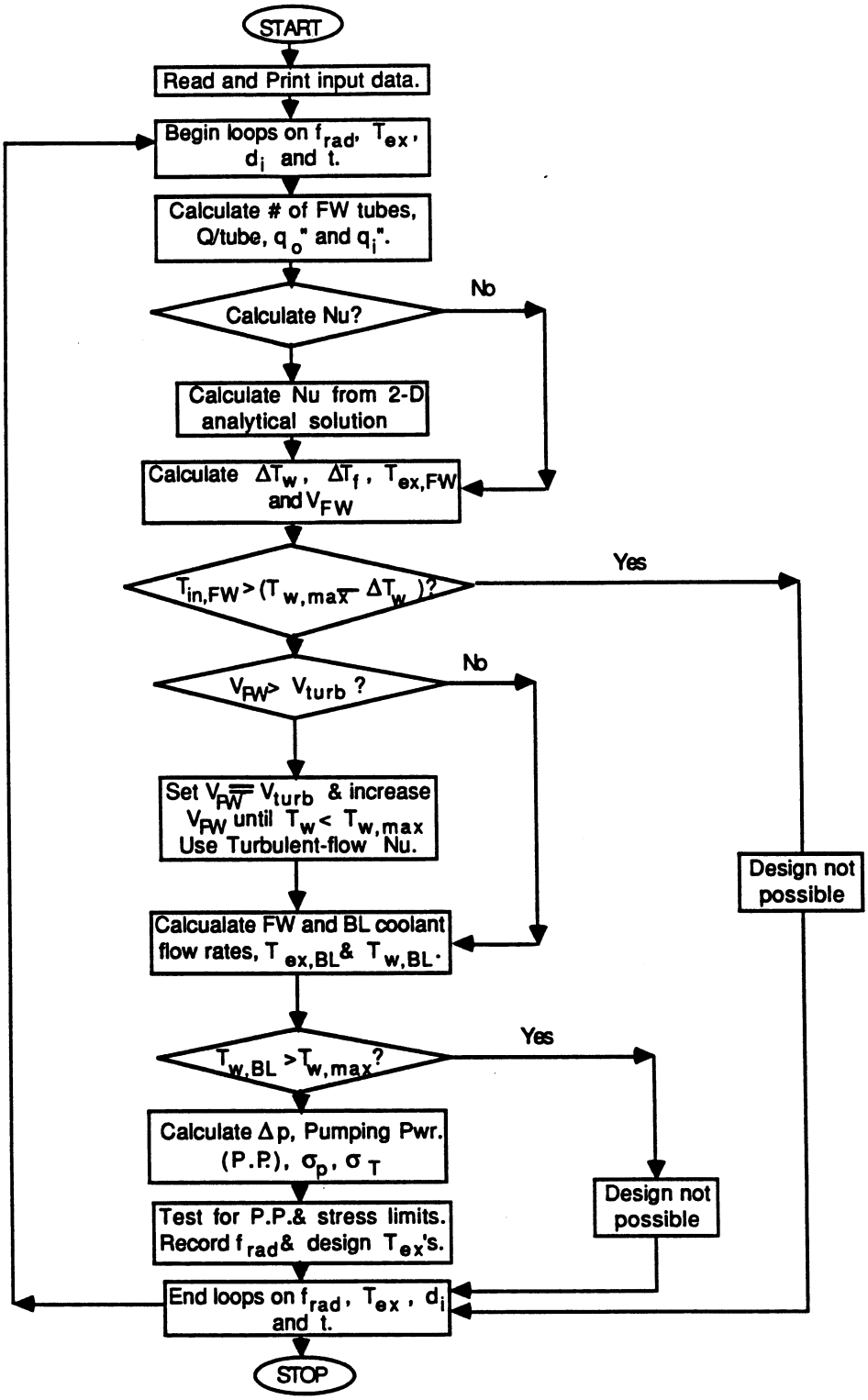

Figure 10.4-8. Flowchart of the TITAN-I thermal-hydraulic design code [124].

film temperature drop, ΔT_f, is recalculated using the Nusselt number for turbulent flow from Equation 10.4-17 (which is halved to account for nonuniform circumferential heat flux). The coolant exit temperature is found using this value of the film temperature drop in the turbulent regime and, if necessary, the coolant velocity is increased until the maximum structure temperature, $T_{w,Max}$, is within the design limit.

For design window calculations, the blanket is treated as a lumped-parameter system. The blanket-coolant exit temperature, $T_{ex,BL}$, is determined by energy balance so that, using the determined $T_{ex,FW}$, the mixed temperature of the first-wall and blanket circuits would match the input value of average coolant exit temperature. The film and wall temperature drops are calculated from Equations 10.4-20 and 10.4-21, and the maximum temperature of the blanket-coolant channel is found from Equation 10.4-19. If the maximum wall temperature is within the design limit, the calculated average coolant exit temperature is recorded as the highest possible exit temperature for the imposed radiation heat flux and structural-temperature limit.

Pressure drop and pumping power are calculated from the coolant velocity. The equations given in Section 10.4.4 are used to estimate the MHD and friction pressure drops. The coolant pressure is highest at the inlet of a coolant channel. Pressure stresses are, therefore, determined at the inlet point of all circuits.

The above procedures are repeated for different values of mixed coolant exit temperature and then for a range of heat fluxes on the first wall.

10.4.5.2. Design window and reference design

The major parameters of the TITAN-I design are given in Table 10.1-I, and the power flow to various FPC components is listed in Table 10.4-I. Relevant parameters of the thermal-hydraulic design are given in Table 10.4-II.

Figure 10.4-9 illustrates the thermal-hydraulic design window for the TITAN-I FPC and shows that a design with a radiation heat flux on the first wall of 4.9 MW/m^2 is possible. The sudden change in the slope of the top curve in Figure 10.4-9, corresponding to the structural-temperature limit, is caused by the change in flow from laminar to turbulent. Also, the pumping-power limit of 5% of electric output is more restrictive in this regime than the pressure stress of 108 MPa. The thermal-stress limit is not reached up to the maximum heat flux on the first wall.

The coolant flow paths in the first-wall and blanket circuits of TITAN-I are shown in Figure 10.4-10, and the variation of the coolant pressure along the length of the coolant

Table 10.4-II.

THERMAL-HYDRAULIC DESIGN PARAMETERS

First-wall heat flux	4.6	MW/m^2
Poloidal field at first wall	5.4	T
Toroidal field at first wall	-0.36	T
Coolant inlet temperature	320	°C
Structural-temperature limit	750	°C
Pressure-stress limit	108	MPa
Thermal-stress limit	300	MPa
Pumping-power limit[a]	50	MW

(*a*) Pumping-power limit is set at 5% of the net electric output.

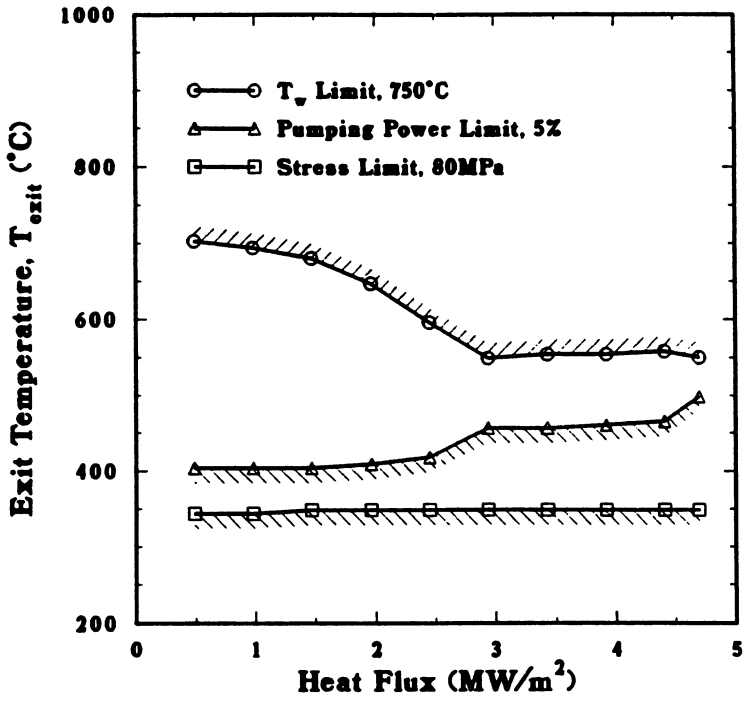

Figure 10.4-9. The thermal-hydraulic design window for the TITAN-I FPC.

A – Entrance
AB – Straight Duct
– Varying B-Field
B – Inlet/Contraction
– Bend
BC – Straight Tube
C – Bend, Expansion
CD – Straight Duct
– Varying B-Field
D – Expansion

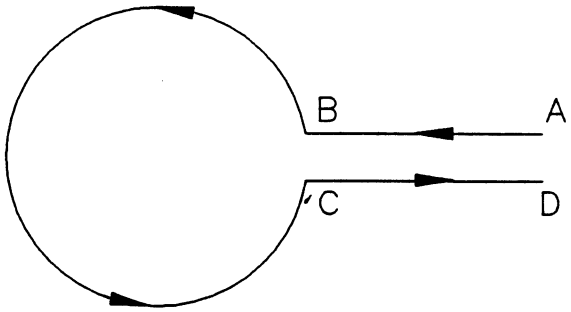

First-Wall Flow Circuit

E – Entrance
EF – Straight Duct
– Varying B-Field
F – Inlet/Contraction
– Bend
FG – Straight Channel
G – Bend, Expansion
GH – Straight Duct
– Varying B-Field
H – Expansion

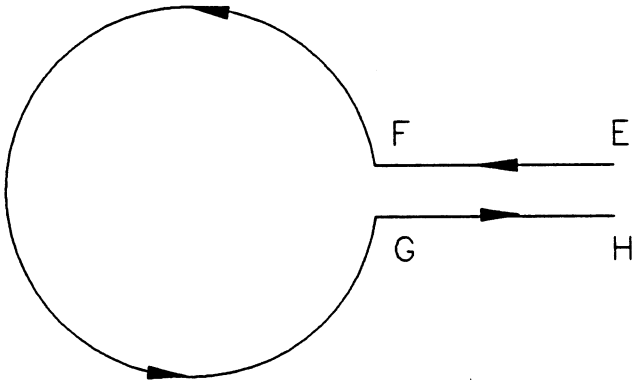

Blanket Flow Circuit

Figure 10.4-10. Coolant flow paths in the first-wall and blanket circuits.

channels of the first wall and blanket is shown in Figure 10.4-11. For the blanket components, the pressure distributions in rows 1 and 6 of the coolant channels of the IBC zone are shown. The pressure drop in the hot shield is negligible because of the low power density and low coolant flow rate.

The coolant flow velocity in the TITAN-I first-wall tube is 21 m/s and the maximum pressure drop is 10 MPa. Since substantial simplification is made by cooling two components (first wall and divertor) from the same cooling circuit, the delivery pressure of the coolant pump for the first-wall and divertor-coolant circuits is set at 12 MPa, the maximum pressure drop at the divertor (Section 11.5). The coolant pressure for the first wall is then reduced to 10 MPa by using an orifice (Section 10.4.7).

The coolant velocities in rows 1 and 6 (last) of IBC-coolant channels are, respectively, 0.5 and 0.2 m/s. The pressure drop is 3.0 MPa in row 1 and 0.5 MPa in row 6. The supply pressure of the blanket coolant pump is 3 MPa. Orifices are used to reduce the pressure to the required values at the inlet of each row of IBC channels (Section 10.4.7).

The pressure and thermal stresses at the inlet of a first-wall tube are shown in Figure 10.4-12. The maximum equivalent pressure and thermal stresses are, respectively, less than 50 and 150 MPa. The allowable pressure stress is a function of material temperature, increasing with the decreased temperature. For a coolant tube, the pressure is highest at the inlet and lowest at the exit. Conversely, the wall temperature is lowest at the inlet and highest at the exit. Figure 10.4-13 presents the pressure stress, average wall temperature, and the allowable stress along the length of a first-wall tube. The pressure stress in the first-wall tubes is 4 to 6 times smaller than the allowable stress. The stresses in the blanket channels are well below the design limits because of the low pressure, thick channel walls, and the small temperature gradient. Finite-element analyses of the pressure and thermal stresses in the first-wall and blanket components have verified these results (Section 10.4.6).

The main results of the thermal-hydraulic analyses of the TITAN-I FPC are given in Tables 10.4-III through 10.4-V.

10.4.6. Finite-Element Thermal and Stress Analyses

Two-dimensional thermal and stress analyses of the TITAN-I FPC were performed by the finite-element code, ANSYS [125], in order to refine and confirm the thermal-hydraulic design estimates. The blanket and shield of the TITAN-I design are not subjected to a high surface heat flux. For the first-wall channels, however, accurate descriptions of both

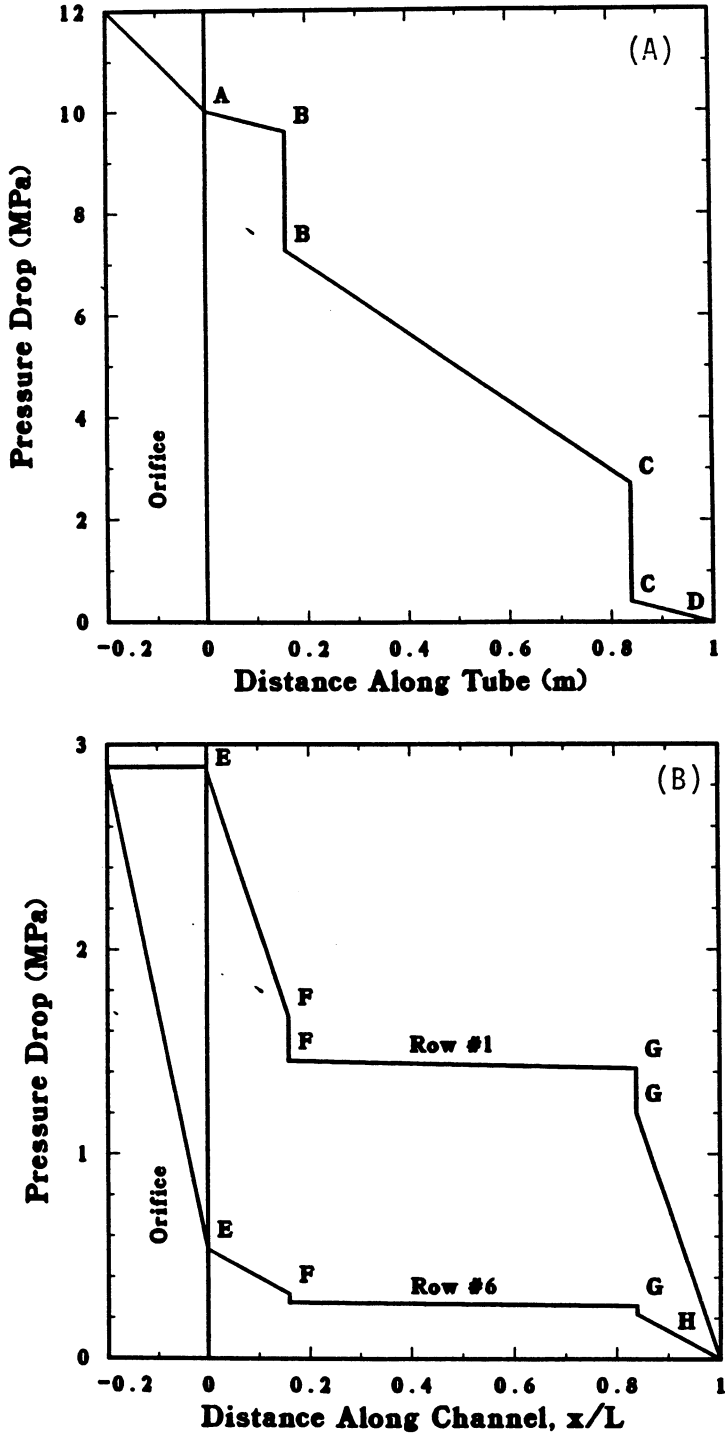

Figure 10.4-11. Pressure distributions in the first-wall (A) and the blanket-coolant channels (B). The pressure drop in the hot shield is negligible. Points A through H correspond to the coolant flow path in Figure 10.4-10.

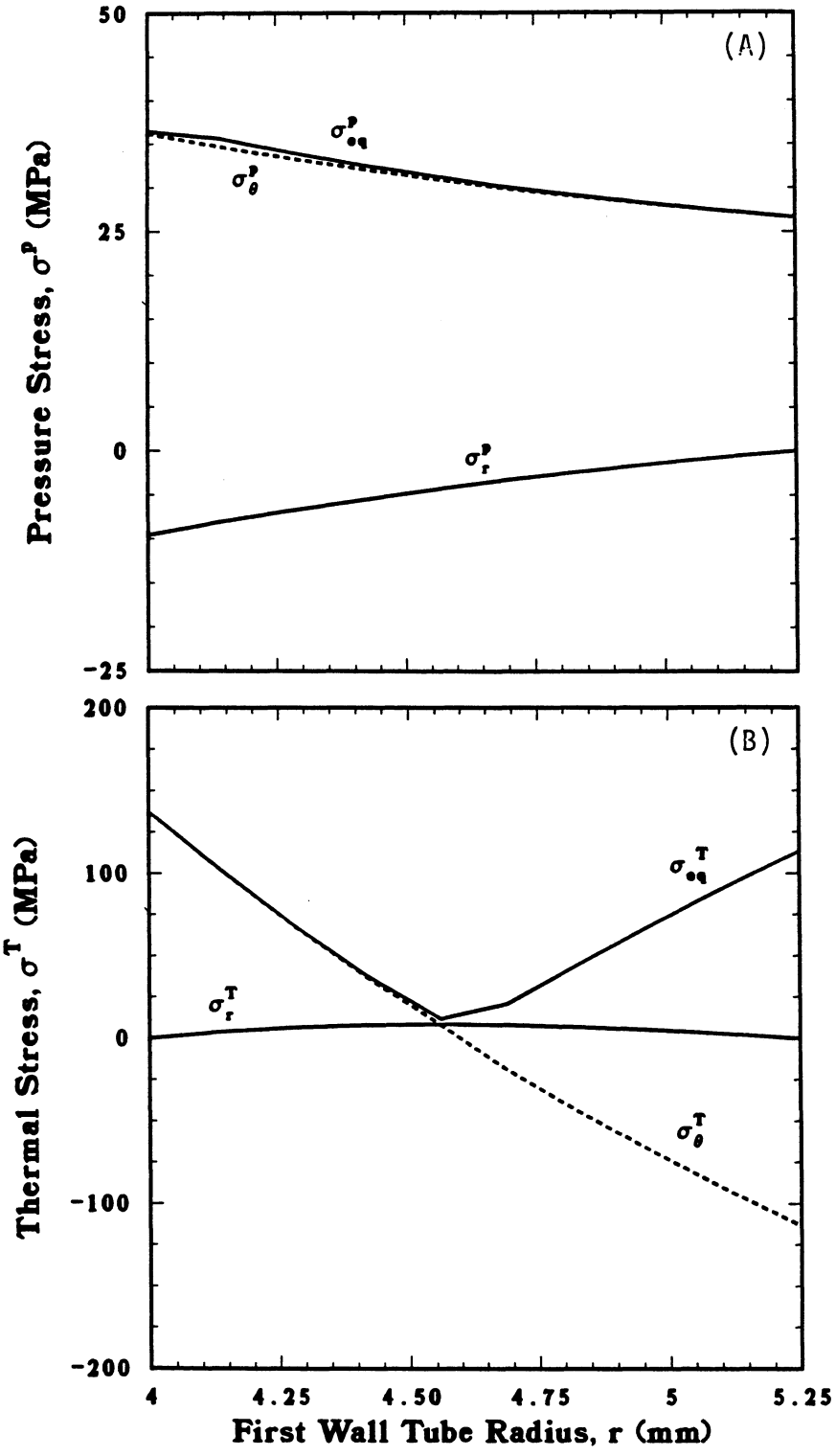

Figure 10.4-12. Pressure stresses (A) and thermal stresses (B) in the TITAN-I first wall as function of the radius of the coolant tube.

Table 10.4-III.

THERMAL-HYDRAULIC DESIGN OF TITAN-I FIRST WALL

Pipe outer diameter, b	10.5	mm
Pipe inner diameter, a	8.0	mm
Wall thickness, t	1.25	mm
Erosion allowance	0.25	mm
Structure volume fraction	0.400	
Coolant volume fraction	0.375	
Void volume fraction	0.225	
Coolant inlet temperature, T_{in}	320	°C
Coolant exit temperature, $T_{ex,FW}$	440	°C
Maximum wall temperature, $T_{w,Max}$	747	°C
Maximum primary stress	50	MPa
Maximum secondary stress	288	MPa
Coolant flow velocity, U	21.6	m/s
Pressure drop, Δp	10	MPa
Total pumping power[(a)]	37.7	MW
Reynolds number, Re	1.90×10^5	
Magnetic Reynolds number, Re_m	0.48	
Parallel Hartmann number, $H_{\|}$	3.04×10^3	
Perpendicular Hartmann number, $H_{\perp}$	2.01×10^2	
Parallel magnetic interaction parameter, $N_{\|}$	48.6	
Perpendicular magnetic interaction parameter, $N_{\perp}$	0.21	
Nusselt number, Nu	10.35	
Prandtl number, Pr	4.08×10^{-2}	
Peclét number, Pe	7.76×10^3	

(*a*) A pump efficiency of 90% is assumed.

Table 10.4-IV.

THERMAL-HYDRAULIC DESIGN OF TITAN-I IBC

Pipe outer diameter	52.5	mm
Pipe inner diameter	47.5	mm
Wall thickness	2.5	mm
Structure volume fraction	0.18	
Coolant volume fraction	0.72	
Void volume fraction	0.10	
Coolant inlet temperature	320	°C
Coolant exit temperature	700	°C
Maximum wall temperature	747	°C
Maximum primary stress(b)	30	MPa
Maximum secondary stress	5	MPa
Coolant velocity(b)	0.5	m/s
Pressure drop(b)	2.8	MPa
Total pumping power(a)	6.0	MW
Reynolds number(b)	2.75×10^4	
Magnetic Reynolds number(b)	0.066	
Parallel Hartmann number(b)	1.9×10^4	
Perpendicular Hartmann number(b)	1.3×10^3	
Parallel magnetic interaction parameter(b)	1.33×10^4	
Perpendicular magnetic interaction parameter(b)	6.15×10^1	
Nusselt number(b)	5.6	

(*a*) A pump efficiency of 90% is assumed.

(*b*) Values for the first row of IBC tubes.

Table 10.4-V.

THERMAL-HYDRAULIC DESIGN OF TITAN-I HOT SHIELD

Coolant inlet temperature	320	°C
Coolant exit temperature	700	°C
Maximum wall temperature	747	°C
Pressure drop	0.1	MPa
Total pumping power[a]	3.0	MW
First Zone		
Channel outer dimensions	60×60	mm
Wall thickness	5	mm
Structure volume fraction	0.30	
Coolant volume fraction	0.70	
Reynolds number	9.79×10^3	
Parallel Hartmann number[b]	7.00×10^3	
Perpendicular Hartmann number[b]	*nil*	
Nusselt number	3.6	
Second Zone		
Channel outer dimensions	112.5×37.5	mm
Wall thickness	16.25	mm
Structure volume fraction	0.90	
Coolant volume fraction	0.10	
Reynolds number	1.84×10^3	
Parallel Hartmann number[b]	1.30×10^3	
Perpendicular Hartmann number[b]	*nil*	
Nusselt number	8.2	

(*a*) A pump efficiency of 90% is assumed.

(*b*) Values for $B_p \sim 2\,\mathrm{T}$, $B_t \sim 0$.

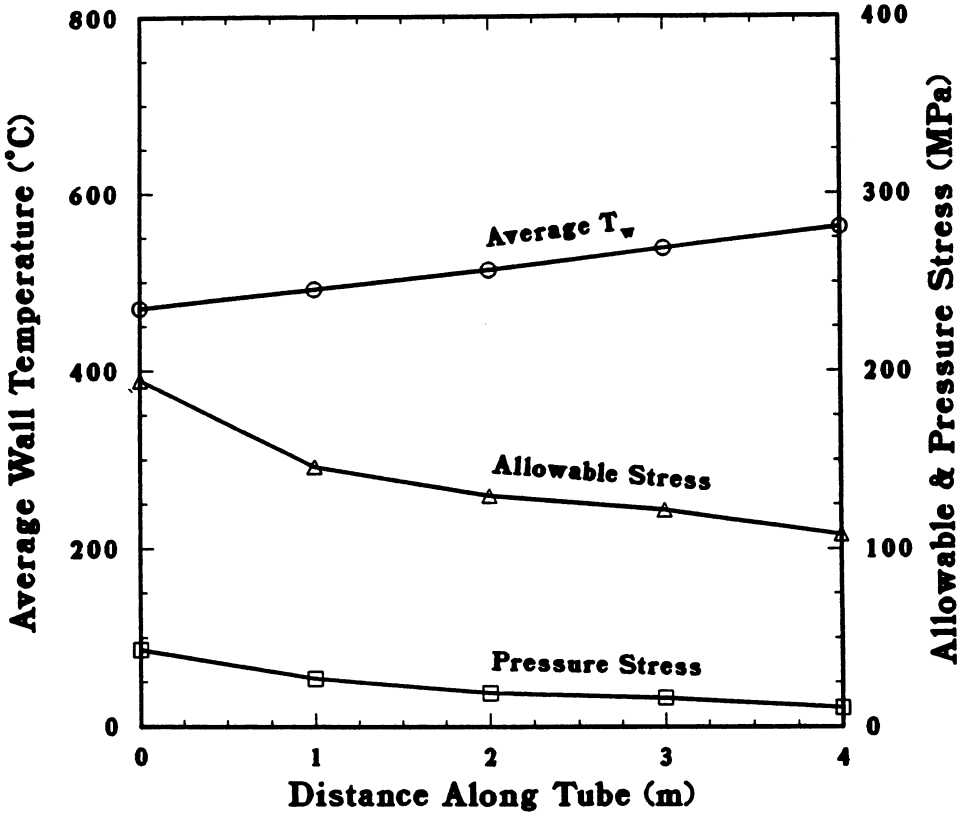

Figure 10.4-13. Safety factors for pressure stress in the first-wall tube.

thermal and pressure stresses should be included. The first-wall geometries and loading conditions suggest that both the thermal and mechanical fields will exhibit significantly smaller gradients in the poloidal direction than in the radial and toroidal directions. A 2-D modeling of the cross section at the location of the extreme value of the loading in the poloidal direction, therefore, is appropriate. This approach has been used in several analyses [2,123], but the assumptions involved were not clearly indicated or were overly conservative. One possible reason for the conservatism is the virtual invariance of the temperatures and, to a lesser degree the pressure stresses, to the assumptions for structures with large radius of curvature. The thermal stresses, however, exhibit more pronounced dependence on the modeling. Various assumptions and models for the finite-element analysis of the TITAN-I FPC are discussed in the next subsection and the results are summarized in the following subsections.

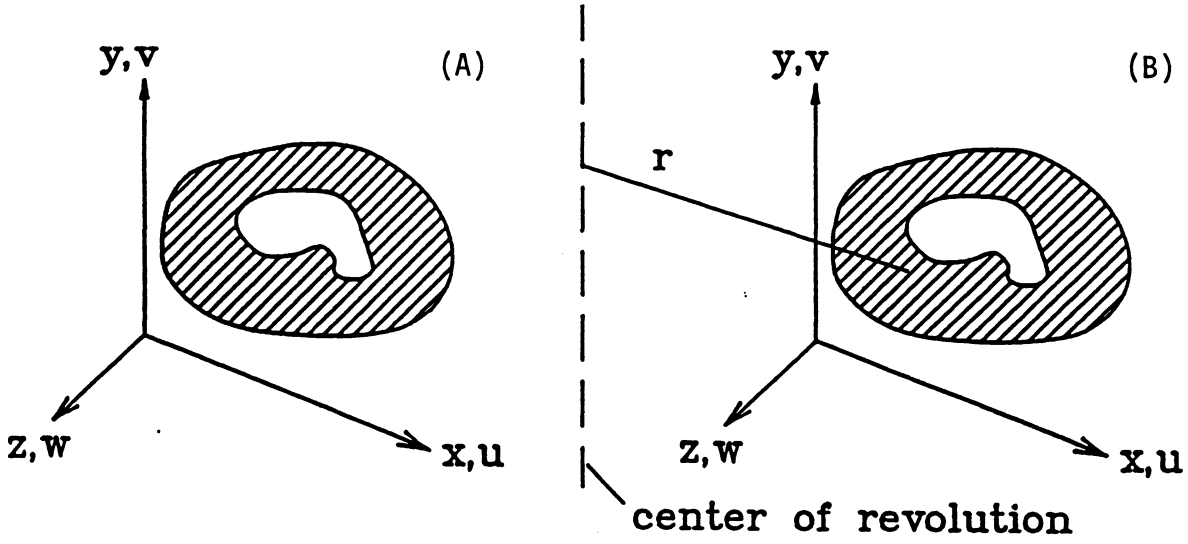

Figure 10.4-14. Displacement components for plane (A) and axisymmetric (B) problems.

10.4.6.1. Finite-element models

The six components of the strain tensor for small deformations, ϵ_{ij}, in the Cartesian coordinate system are given in terms of the displacements as:

$$\epsilon_{ij} = \frac{1}{2}\left(\frac{\partial u_i}{\partial x_j} + \frac{\partial u_j}{\partial x_i}\right), \tag{10.4-32}$$

where x_i $(i = 1, 2, 3)$ represents a Cartesian coordinate system and u_i denotes the displacements. If certain assumptions regarding the behavior in a direction are considered, the number of independent stress and strain components can be decreased significantly.

Plane-strain assumptions. The displacement components shown on Figure 10.4-14 are assumed to have the following form:

$$\begin{aligned} u_1 &= u(x, y), \\ u_2 &= v(x, y), \\ u_3 &= 0. \end{aligned} \tag{10.4-33}$$

These assumptions describe exactly a situation when a cylinder of arbitrary length is entirely constrained from axial movement and the deformation is independent of the axial dimension,

$$\begin{aligned} \epsilon_{xx} &= \frac{\partial u}{\partial x}, \\ \epsilon_{yy} &= \frac{\partial v}{\partial y}, \\ \epsilon_{xy} &= \frac{1}{2}\left(\frac{\partial u}{\partial y} + \frac{\partial v}{\partial x}\right), \\ \epsilon_{zz} &= 0. \end{aligned} \tag{10.4-34}$$

The constitutive equations including thermal strains are

$$\epsilon_{ij} = \frac{1}{E}[(1+\nu)\sigma_{ij} - \nu(\sigma_{xx} + \sigma_{yy} + \sigma_{zz})] + \alpha T, \tag{10.4-35}$$

where σ_{ij} is the stress tensor, E is the Young's modulus, α is the thermal-expansion coefficient, and T is based on some reference temperature. Using Equation 10.4-35 for $\epsilon_{zz} = 0$,

$$\sigma_{zz} = \nu(\sigma_{xx} + \sigma_{yy}) - E\,\alpha T. \tag{10.4-36}$$

If equivalent properties $E' = E/(1-\nu^2)$, $\nu' = \nu/(1-\nu)$, and $\alpha' = \alpha(1+\nu)$ are introduced, then the constitutive equations assume the following form:

$$\begin{aligned} \epsilon_{xx} &= \frac{1}{E'}(\sigma_{xx} - \nu'\sigma_{yy}) + \alpha' T, \\ \epsilon_{yy} &= \frac{1}{E'}(\sigma_{yy} - \nu'\sigma_{xx}) + \alpha' T, \\ \epsilon_{xy} &= \frac{1+\nu'}{E'}\sigma_{xy}. \end{aligned} \tag{10.4-37}$$

Additional mechanical field equations include equilibrium and compatibility equations.

Plane-stress assumptions. These assumptions approximately correspond to the behavior of a thin disk that is free of loading at the flat ends:

$$\begin{aligned} u_1 &= u(x,y), \\ u_2 &= v(x,y), \\ \sigma_{zz} &= \sigma_{xz} = \sigma_{yz} = 0. \end{aligned} \tag{10.4-38}$$

Since the disk is thin, the variation of these stress components must be small compared with the in-plane stresses. The strains for small deformations are:

$$\begin{aligned}
\epsilon_{xx} &= \frac{1}{E}(\sigma_{xx} - \nu\sigma_{yy}) + \alpha T\,, \\
\epsilon_{yy} &= \frac{1}{E}(\sigma_{yy} - \nu\sigma_{xx}) + \alpha T\,, \\
\epsilon_{xy} &= -\frac{1+\nu}{E}\,\sigma_{xy}\,, \\
\epsilon_{zz} &= -\frac{\nu}{E}(\sigma_{xx} - \sigma_{yy}) + \alpha T\,.
\end{aligned} \tag{10.4-39}$$

Comparing these expressions with Equation 10.4-37 shows that the in-plane quantities of a plane-strain problem can be obtained by solving the corresponding plane-stress problem with the equivalent properties. The out-of-plane stress component can be calculated from Equation 10.4-36. For thermal problems in toroidal fusion applications the out-of-plane forces can be high, since the αE product ranges from 1 to 3 for the structural materials considered, and the temperature difference between the current and the reference temperature can exceed 300 °C.

Axisymmetric deformation assumptions. The displacements are assumed to be given by

$$\begin{aligned}
u_1 &= u(x,y)\,, \\
u_2 &= v(x,y)\,, \\
u_3 &= 0\,.
\end{aligned} \tag{10.4-40}$$

The strain components are:

$$\begin{aligned}
\epsilon_{xx} &= \frac{\partial u}{\partial x}\,, \\
\epsilon_{yy} &= \frac{\partial v}{\partial y}\,, \\
\epsilon_{xy} &= \frac{1}{2}\left(\frac{\partial u}{\partial y} + \frac{\partial v}{\partial x}\right)\,, \\
\epsilon_{zz} &= \frac{u}{r}\,.
\end{aligned} \tag{10.4-41}$$

There are four stress components. The out-of-plane stress is not zero, and its value is generally less than that obtained from a plane-strain analysis of the same plane section

under the same loading conditions. If the geometry and the loading of the structure considered is nearly axisymmetric, then the modeling should also be axisymmetric. Note that plane-stress modeling underestimates, whereas plane-strain formulation overestimates the out-of-plane stress component.

Since the structural material is metallic, the relevant uniaxial stress measure is the von Mises stress, which is given by

$$\sigma_{eq} = \sqrt{\frac{1}{2}\left[(\sigma_1 - \sigma_2)^2 + (\sigma_2 - \sigma_3)^2 + (\sigma_1 - \sigma_3)^2\right]}, \qquad (10.4\text{-}42)$$

where σ_1, σ_2, and σ_3 are the principal stresses. Yielding in metals has been observed to occur as a result of distortion and not volume change; therefore, the equivalent stress is based on the equality of the distortional strain energy associated with a given 3-D stress state and the distortional energy caused by the uniaxial equivalent stress. Note that a hydrostatic state produces zero equivalent stress.

10.4.6.2. Thermomechanical analysis of the first wall

In this section the results obtained from plane-stress and axisymmetric analyses of the TITAN-I first wall are discussed. Pressure stresses as well as thermal stresses are calculated. The geometry analyzed is based on a circular tube with inner diameter of 8 mm, outer diameter of 10.5 mm, and radius of curvature of 66 cm. The internal pressure is 10 MPa. The radiation heat flux is uniform and emanates from the center of curvature of the first-wall tube and, hence, is incident only on the inner side of the tube. The heat flux on the circumference of a tube is assumed to be a cosine distribution, as is mentioned in Section 10.4.2. The peak heat flux is 4.6 MW/m^2, the internal heat-generation rate is 105 MW/m^3, the fluid bulk temperature is 427 °C, and the Nusselt number is 10.34. The calculations were performed using ANSYS [125]. The cross section of the first-wall tube is shown in Figure 10.4-15 and was modeled by utilizing symmetry. The boundary conditions for the thermal and mechanical analyses are also explained on Figure 10.4-15.

Pressure stresses. The in-plane pressure stresses exhibit the same axial symmetry within the tube cross section in both plane-stress and axisymmetric analyses. The effect of poloidal curvature appears only in the presence of a near-constant poloidal stress. The maximum equivalent stress is 41 MPa in the plane-stress analysis and 39 MPa in the axisymmetric analysis. The latter stress is lower because the curvature produces tensile stresses in the poloidal direction, and the stress state becomes closer to a hydrostatic state.

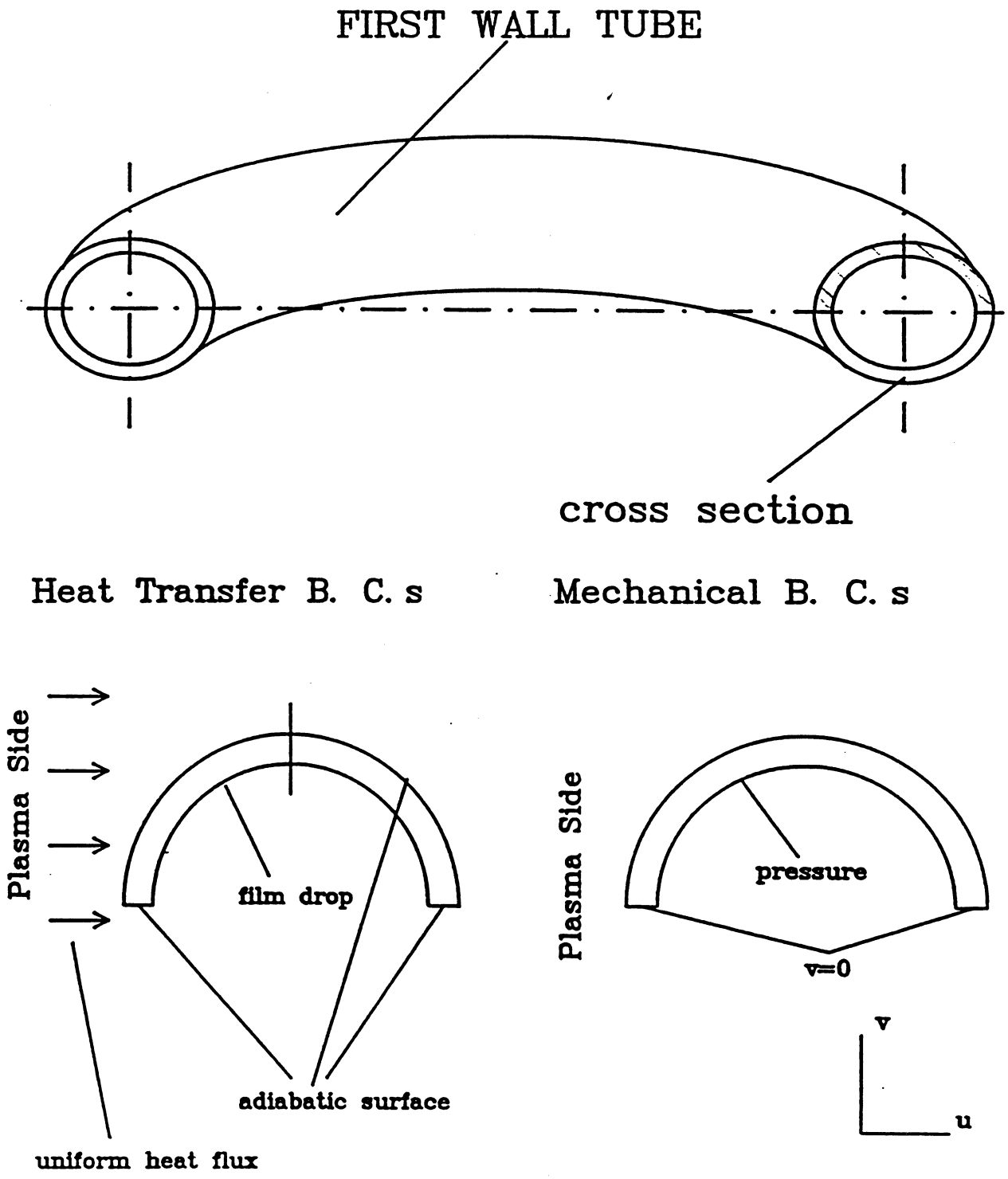

Figure 10.4-15. Model of the TITAN-I first-wall tube for finite-element analysis and the thermal and mechanical boundary conditions.

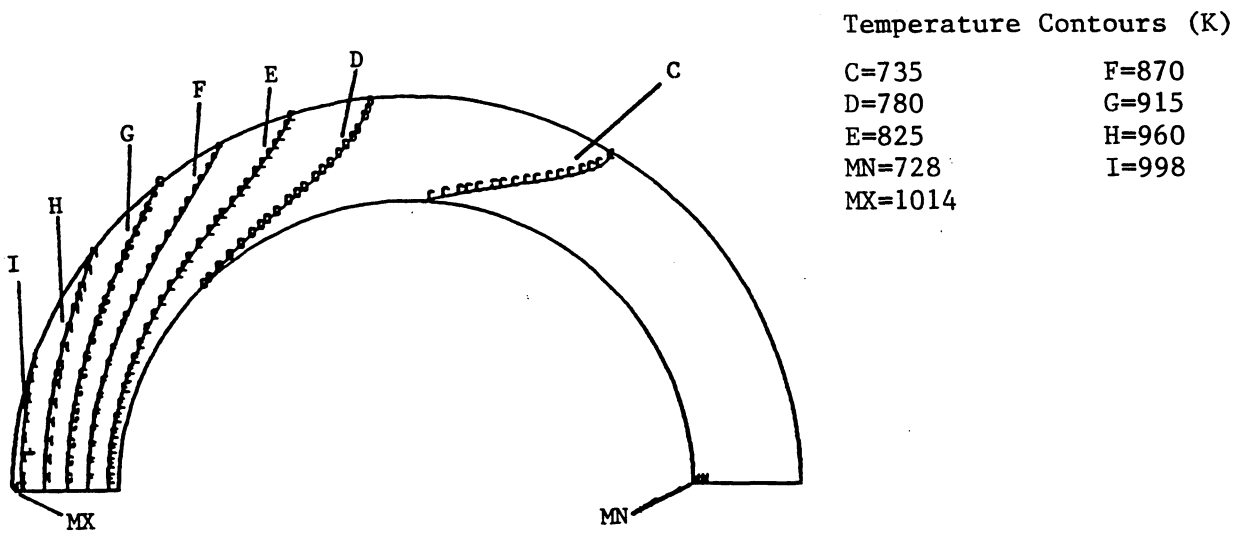

Figure 10.4-16. Temperature contours in the first wall of the TITAN-I design.

Temperatures. The maximum temperature and the temperature drop across the wall are lower than in the uniform-heat-flux case because of the cosine distribution of the surface heat flux. The temperature contours in Figure 10.4-16 are from the axisymmetric analysis. Results from the 2-D models are also very close to those given in Figure 10.4-16, and show the weak dependence of the thermal field on the fairly large radius of curvature. The maximum temperature of 741 °C occurs at the point closest to the plasma, and the minimum temperature of 429 °C is at the point farthest from the plasma at the inner radius. These results are in good agreement with the 1-D analysis reported in Section 10.4.5.2.

Thermal stresses. The equivalent stresses from the plane-stress model are shown in Figure 10.4-17. Figure 10.4-18 illustrates the stress contours of the poloidal and equivalent stresses, both of which are based on axisymmetric analysis. The asymmetry of the temperature field causes significant poloidal stresses with stress contours resembling the temperature contours. The maximum and minimum stresses are, respectively, 98.7 and 0.17 MPa in the plane-stress model, and 279 and 11.6 MPa in the axisymmetric model. Although ignoring the poloidal stresses in the calculation of the pressure stresses does not cause significant errors and proved to be conservative, the thermal stresses developed in a thin disk are different from those in an axisymmetric structure. Plane-stress results still

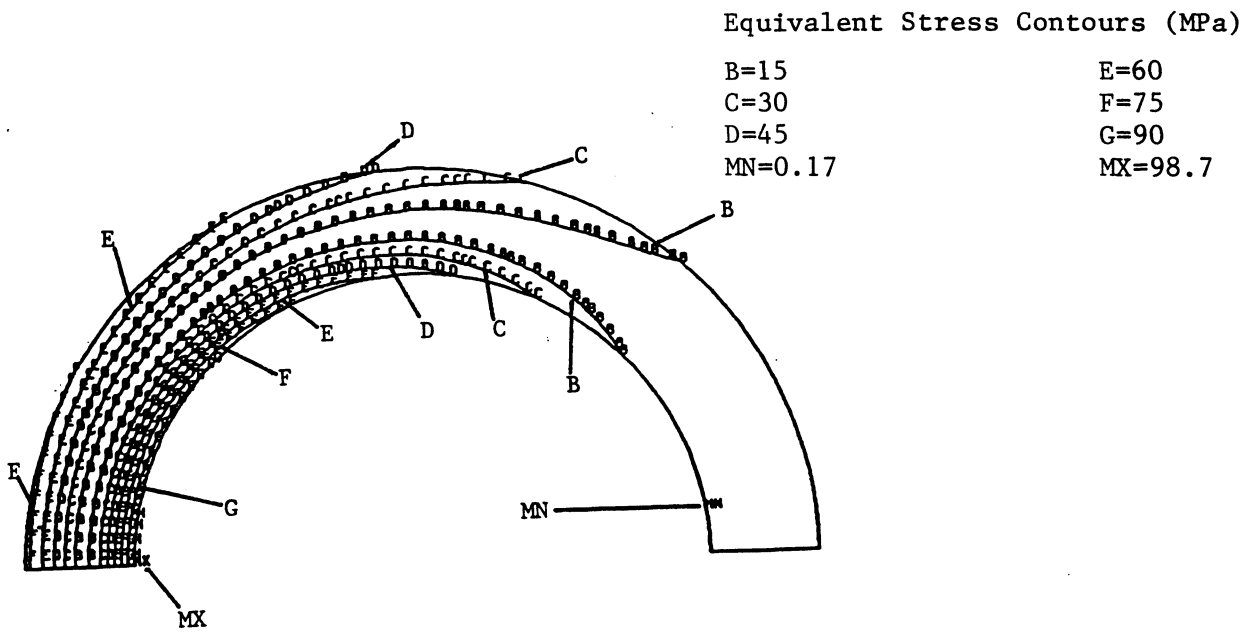

Figure 10.4-17. Equivalent stress in the first wall of the TITAN-I design from the plane-stress model.

give a good estimate of the magnitude of the stresses but have to be treated cautiously because of their non-conservative nature. Also, the asymmetric temperature distribution caused by the one-sided heating raises the stress level even further.

Summary: Assuming a value of 108 MPa as the allowable primary stress and 750 °C as the maximum wall temperature for the vanadium alloy, all structural design criteria are satisfied and the current design is feasible. Future analyses should address the effect of the poloidally varying coolant temperature and possible methods to relieve some of the poloidal thermal stresses.

10.4.6.3. Thermomechanical analysis of blanket and shield

The TITAN-I blanket consists of an array of self-supporting tubes. The blanket structure is subjected to heat generation and internal coolant pressure. Based on arguments given above, an axisymmetric finite-element model was set up for the analysis of the blanket structure. The results from the thermal-hydraulic code indicate that a low blanket-coolant pressure of 1 to 3 MPa is required (Section 10.4.5.2). Accordingly, the

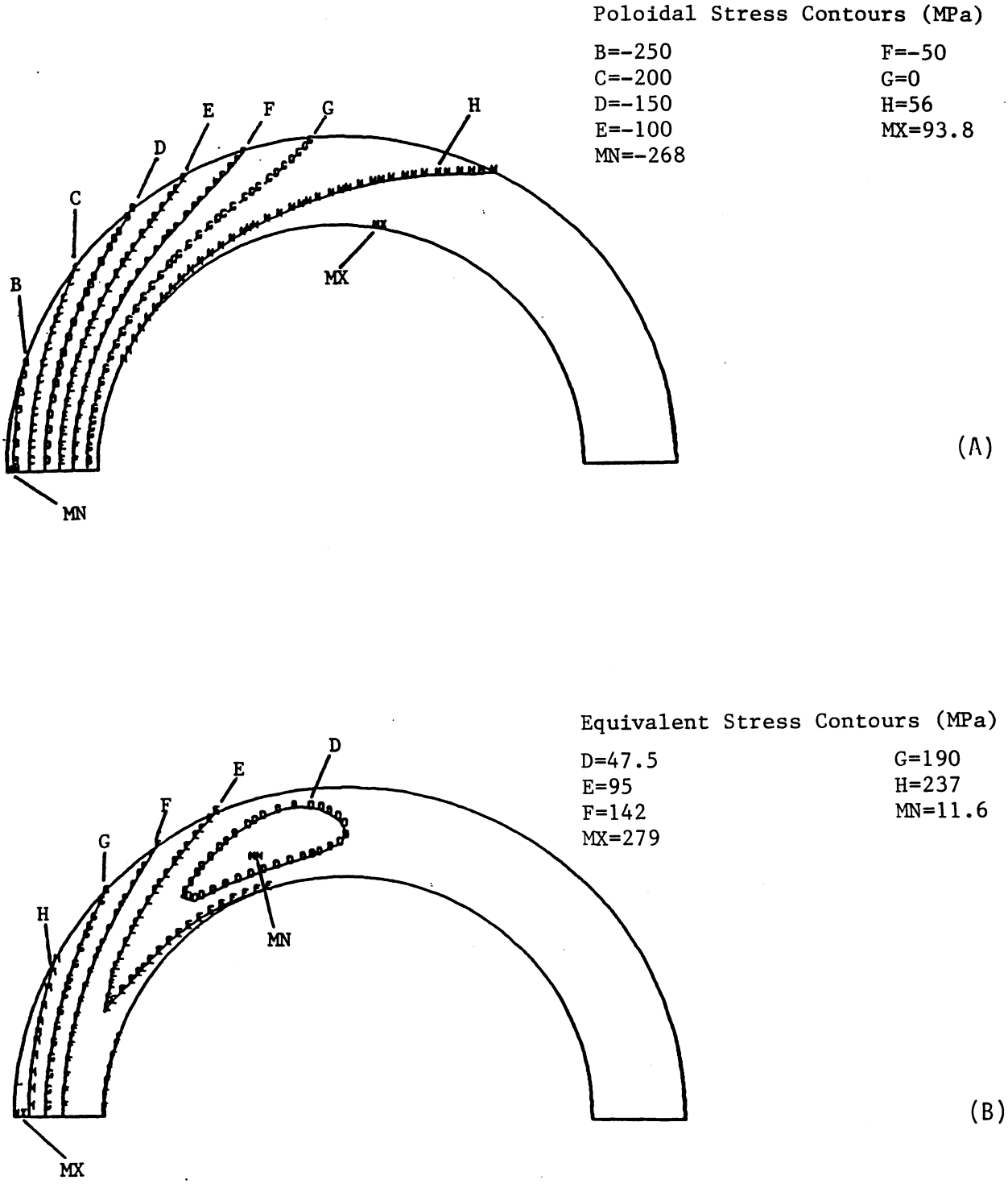

Figure 10.4-18. Poloidal stresses (A) and equivalent stresses (B) in the first wall of the TITAN-I design from the axisymmetric model.

blanket tubes will have a large ratio of radius-to-wall thickness, and a simple 1-D analysis is sufficient. The results of the thermal-hydraulic code have been verified by comparison to the finite-element results; the maximum primary and secondary stresses in the blanket are found to be about 30 and 5 MPa, respectively.

The hot shield of the TITAN-I design consists of a set of self-supporting, rounded-corner square and rectangular channels which offer the advantage of a lower void fraction, improving both the neutron energy multiplication and the shielding of the OH magnets. Coolant pressure is the main factor determining the size of the shield channels. Figure 10.4-19 shows the contours of the primary equivalent stresses, displaying stress concentrations at the corners. Figure 10.4-20 gives the dependence of the primary stresses on the channel geometry. Increasing the channel size would result in higher bending stresses at the corners. The radius of the fillet acts oppositely (*i.e.*, larger radius relieves stress concentration). Figure 10.4-20 is used in the thermal-hydraulic design (Section 10.4.5.1). For a given coolant pressure (< 3 MPa in TITAN-I shield) and a given allowable primary stress (108 MPa), the appropriate aspect ratio for the channel (c/t) is found from Figure 10.4-20. The wall thickness is then independently determined by the heat-transfer calculations based on maximum allowable wall temperature, which, together with c/t, completely prescribe the size of the channel.

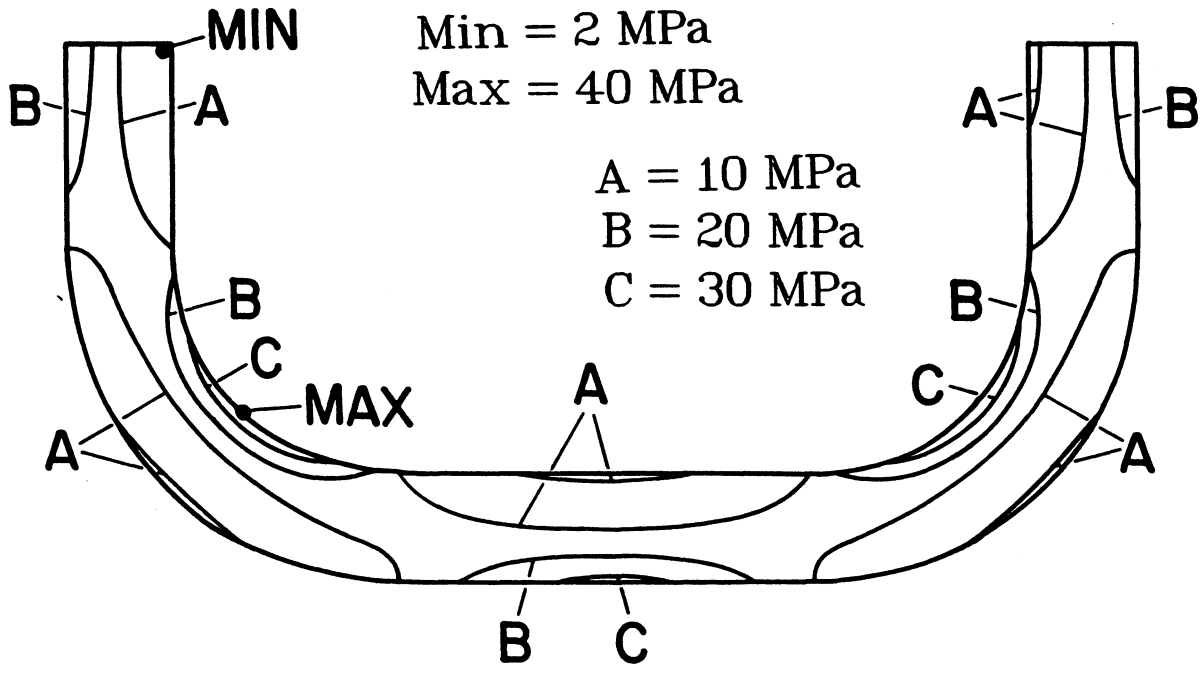

Figure 10.4-19. Contours of the equivalent primary stresses in TITAN-I shield.

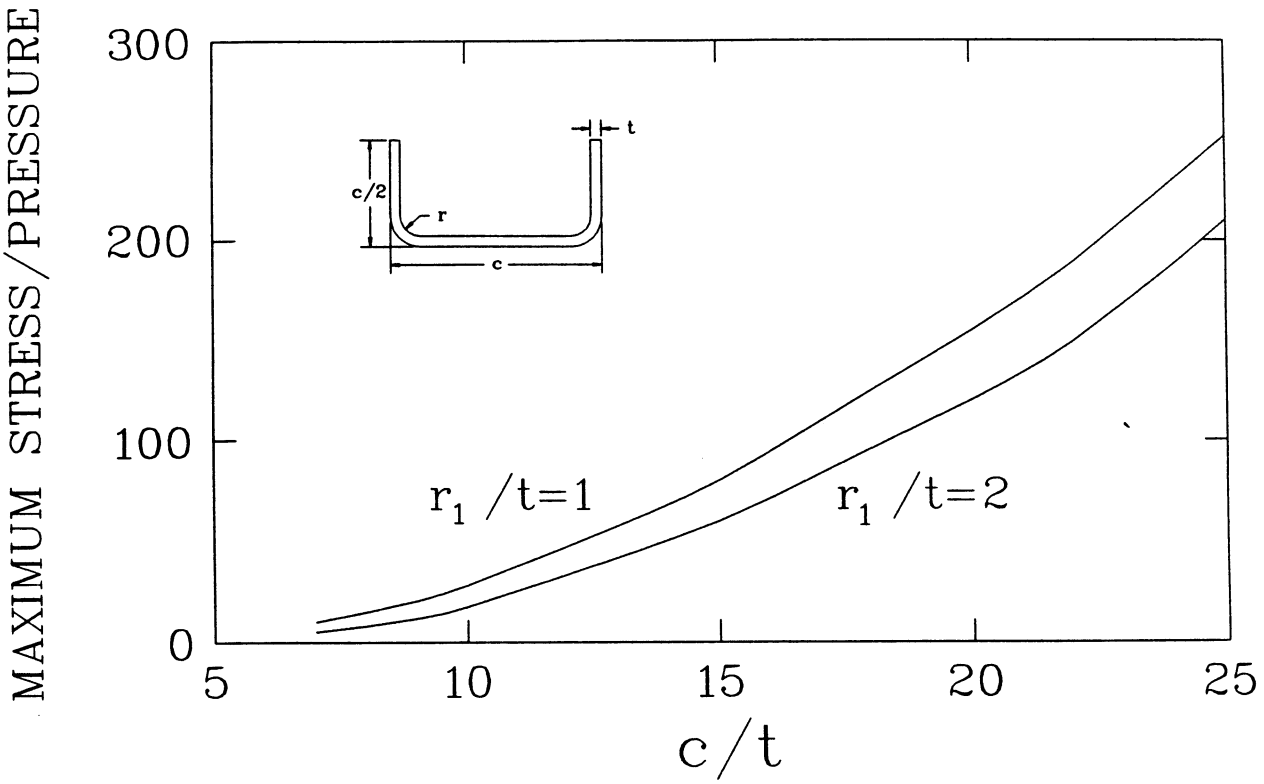

Figure 10.4-20. Geometry of the shield channels and the sensitivity of the pressure stresses to the channel geometry.

10.4.7. Coolant-Circulation Pumps

The pressure drops in the first-wall and divertor circuits are much higher than in the blanket circuit. The maximum pressure drops in the divertor, first-wall, and blanket-coolant circuits are, respectively, 12, 10, and 3 MPa. In order to simplify the design, the first-wall and divertor coolants are supplied from the same circuit. Therefore, two separate coolant pumps are used to circulate the lithium: one for the first-wall and divertor circuit, and the second for the blanket and shield circuit. The pressure drop in the intermediate heat exchanger is small ($\sim$ 0.1 MPa). The delivery pressure of the first-wall and divertor-coolant pump is 12 MPa. A single orifice is used to reduce the lithium pressure to 10 MPa for the first-wall circuit (Figure 10.4-11). Additional orifices are used, where necessary, to reduce the coolant pressure from 12 MPa to the required inlet pressure of the individual rows of divertor-coolant tubes. The blanket-coolant pump has a delivery pressure of 3 MPa. Orifices are used to reduce the pressure to match the requirements for each row of IBC and shield channels.

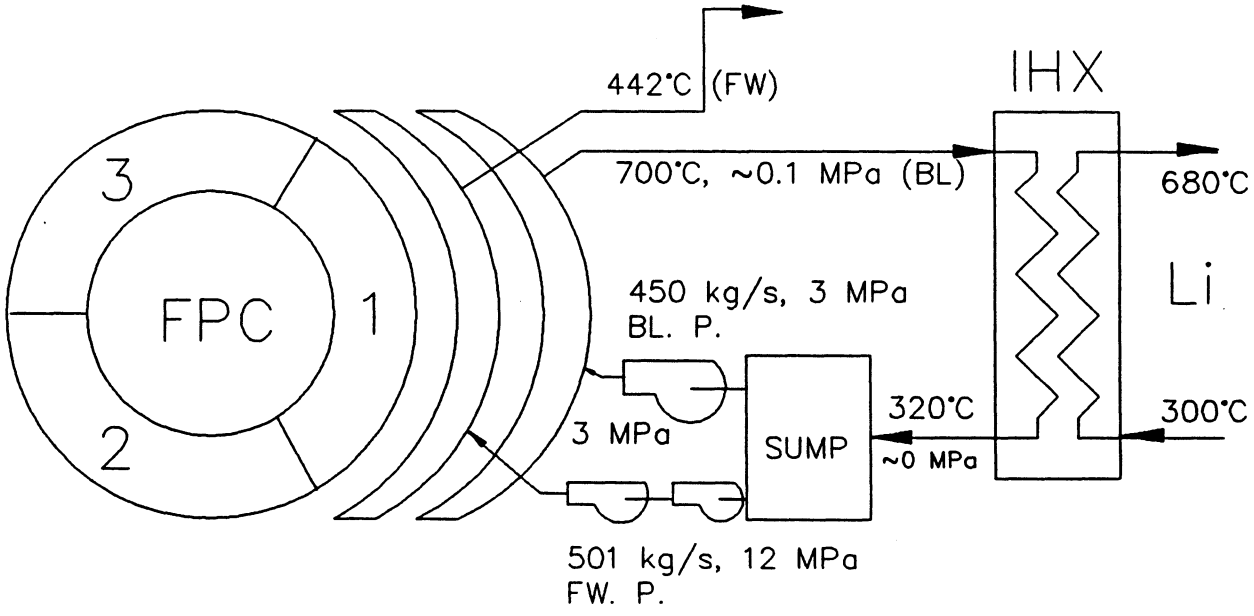

Figure 10.4-21. A schematic of the coolant circulation in the TITAN-I reactor.

Figure 10.4-21 is a schematic of the coolant flow in TITAN-I. All of the coolant-circulation pumps are centrifugal pumps. The pump capacity, Q (gallon per minute, GPM), the pump speed, N (rpm), and the head, H (feet of the fluid pumped) of a centrifugal pump are related through the specific speed, N_s (rpm) [126]. Conversion to SI units (Q in m^3/s and H in m) results in

$$N_s = 2.12 \times 10^{-2} \frac{N\sqrt{Q}}{H^{3/4}} . \qquad (10.4\text{-}43)$$

The fusion power core of TITAN-I is divided into three sectors separated by the three divertor modules. The coolant flow rates per sector are $1.2\,m^3/s$ (16,000 GPM) in the first-wall and divertor circuit, and $1.1\,m^3/s$ (14,500 GPM) in the blanket and shield circuit. Centrifugal pumps for feed water in large central stations have stage pressure of 7 MPa and speed of 9,000 rpm [126]. Therefore, a two-stage centrifugal pump with stage pressure of 6 MPa is suggested for the first-wall and divertor circuit and a single-stage pump is used for the blanket circuit. From Equation 10.4-43, the required speed of the first-wall and divertor pump, at the capacity of $1.2\,m^3/s$, is 8,100 rpm. The required speed of the blanket and shield pump is 5,200 rpm at the capacity of $1.1\,m^3/s$. The specific speed is assumed to be 2,000 rpm which results in a pump efficiency of about 90%.

10.4.8. First-Wall Erosion

Material erosion is one of the critical issues of the first-wall design. While a thin wall will reduce the temperature drop across the wall of the coolant tube, a thicker wall is necessary to reduce the pressure stress and material erosion. Therefore, it is necessary to include an erosion allowance so that enough material remains to keep the pressure stress within the design limit at the end of life of the first wall. The erosion allowance for the first-wall tube is 0.25 mm, which is adequate according the present state of understanding of the erosion mechanisms and the quantification of various erosion rates.

Several potential processes for the erosion of first-wall material have been identified:

1. Sputtering by ions and neutral atoms,
2. Erosion by the high-velocity coolant impact and/or cavitation,
3. Mechanical abrasion caused by the impact of high-velocity suspended foreign particles,
4. Fretting abrasion resulting from flow-induced vibration of the coolant tubes,
5. Corrosion caused by chemical reaction with the coolant.

The TITAN reactors operate with a highly radiative plasma and utilize high-recycling divertors as the impurity-control system. As a result, the particle flux on the first wall is substantially reduced and the the edge-plasma temperature is below the sputtering threshold. The sputtering erosion of the TITAN-I first wall is expected to be less than 0.1 mm/y (Section 5). Erosion from the impact of lithium and foreign particles is expected to be very small. Cavitation is not likely because the coolant pressure is high and the vapor pressure of lithium is low. To prevent vibration, the first-wall-coolant tubes are rigidly attached to each other by tack-welding the adjacent tubes together at the back.

Corrosion of vanadium alloys by lithium is not well tested at this time. Hays [52] measured a total depth of material removal of 7.6×10^{-3} mm (or 0.133 mm/y) in a 500-h test of corrosion resistance of Nb-1Zr alloy exposed to 1073 to 1143 °C liquid lithium flowing at 50 m/s. Given the very low corrosion rate of Nb-1Zr by hot lithium flowing at 50 m/s, it can be expected that the lithium coolant at 350 °C flowing in the first-wall tube at 21 m/s will have a very small corrosion effect on vanadium alloys. A detailed discussion of the first-wall erosion is given in Section 10.2.2.3.

10.4.9. Summary

The thermal-hydraulic design of the first wall and blanket of the TITAN-I reactor is feasible using liquid lithium as the coolant. This design is economically attractive because of the high exit temperature of the blanket coolant and the resulting high thermal-energy conversion efficiency of 44% (Section 10.6). The main design features and improvements which have contributed to the feasibility of this design are as follow:

1. Use of high-recycling divertors so that the first-wall sputtering erosion is almost negligible;
2. Use of small-diameter, thin-walled circular tubes as coolant channels for the first wall;
3. Separation of the first-wall and blanket-coolant circuits;
4. Alignment of the coolant channels with the dominant, poloidal magnetic field;
5. Use of turbulent-flow heat transfer to remove the high heat flux on the first wall.

The present design of the TITAN-I FPC is based on the most suitable experimental data and appropriate extrapolations available. A number of critical issues remain. The MHD pressure-drop equations for bend, contraction, and varying magnetic field need to be substantiated by further large-scale experiments and numerical and theoretical analyses. In MHD turbulent-flow heat transfer, experimental data should be extended to cover a wider range of Hartmann numbers especially suited for the TITAN-I regime of operation (*i.e.*, high coolant velocity in a relatively weak magnetic field). The combined effect, if any, of the parallel and perpendicular magnetic fields on flow transition and turbulent-flow heat transfer should also be investigated.

The effect of nuclear volumetric heating in the coolant on film temperature drop has been neglected in the present design, as it has been in most previous fusion-reactor design studies. For high volumetric nuclear heating in the coolant, the additional film temperature drop could be appreciable [127] and should be included in future design studies.

10.5. MAGNET ENGINEERING

Three types of magnets are used in the TITAN-I design: normal-conducting copper coils for the ohmic-heating (OH) and equilibrium-field trim magnets, normal-conducting, integrated blanket coils (IBC) for the divertor and toroidal-field (TF) magnets, and superconducting coils for the equilibrium-field (EF) magnets. Each coil system has a unique set of operating conditions that lead to unique constraints on the coil design. A detailed magnetics design of the TITAN-I magnet systems is presented in Section 4. The engineering and design constraints of TITAN-I magnet systems are discussed in the following subsections.

A poloidal cross section of the TITAN-I FPC is shown in Figure 10.5-1. The OH, EF, and trim coils are symmetric about the midplane and the upper OH coils are labeled 1 through 7 in a counterclockwise direction. The six concentric blanket pipes shown in this figure are the IBCs which produce the toroidal magnetic field. Figure 10.5-2 shows the poloidal cross section of the TITAN-I design through one of the divertor modules, illustrating the divertor IBCs.

10.5.1. Ohmic-Heating Coils

The OH coils are used for start-up and subsequently utilized as part of the poloidal-field (PF) driver-coil set of the oscillating-field current-drive (OFCD) system. The TITAN-I OH coils are normal conducting with copper as the conductor and helium as the coolant. Water coolant was ruled out because of the TITAN-I safety guideline that no water is allowed inside the primary-loop containment structure because of the presence of the liquid-lithium coolant of the FPC (Section 13.3). The insulating material is spinel ($MgAl_2O_4$), chosen for its superior resistance to irradiation damage (Section 10.2.3).

The TITAN-I design has 14 OH coils, connected in series, with the same current density. Table 10.5-I shows the size, location, and current (number of turns) in each coil as have been determined by the magnetics constraints (Section 4) and the plasma start-up requirements (Section 6). The TITAN-I start-up scenario is chosen such that the start-up power is directly extracted from the power grid without requiring any on-site power-storage system (other than the coils themselves).

The TITAN-I start-up switching sequence is shown in Figure 10.5-3. The corresponding current and voltage waveforms are presented in Figure 10.5-4. The TITAN-I start-up sequence uses a bipolar swing of the OH-coil currents and begins with charging the OH

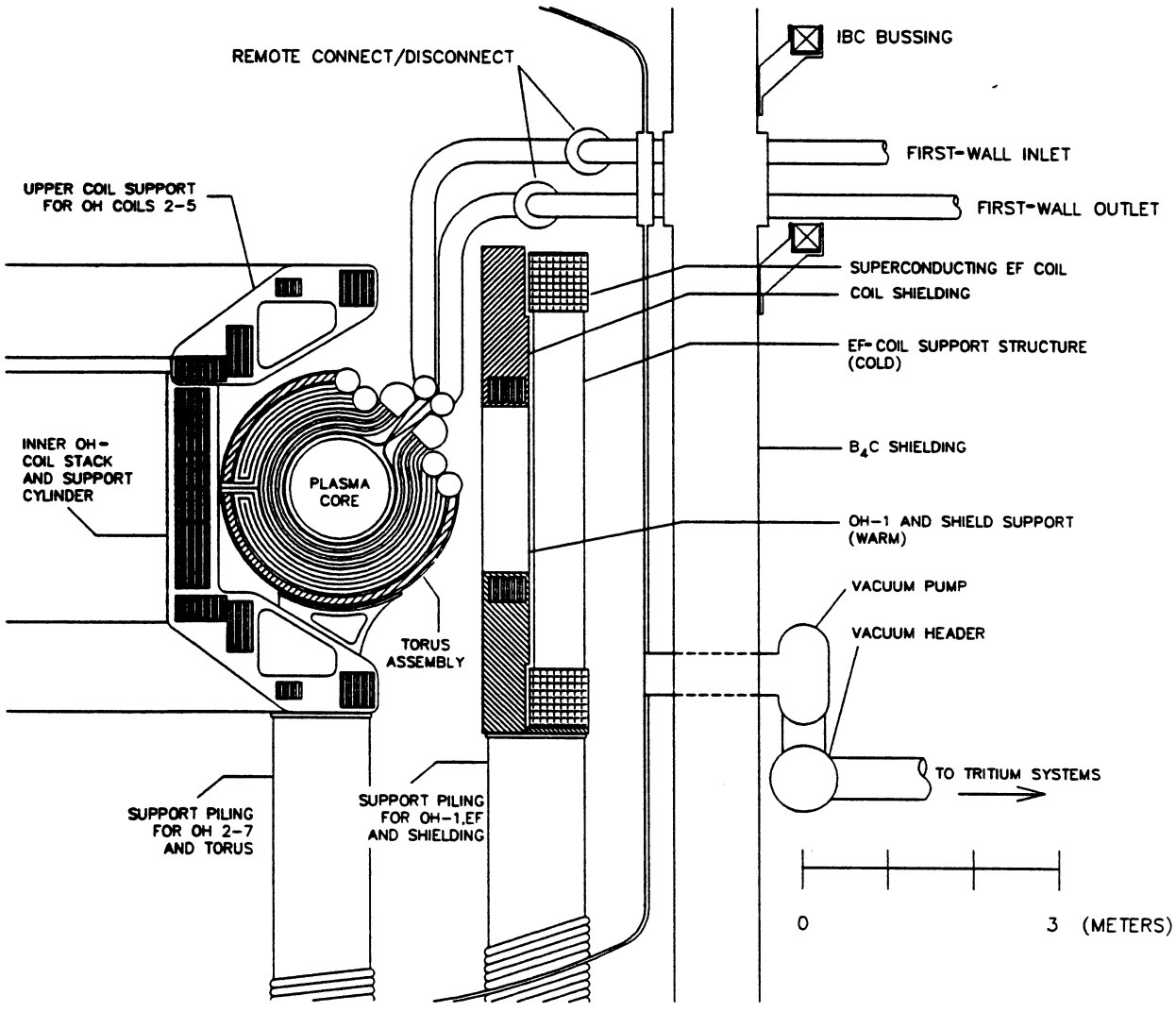

Figure 10.5-1. Poloidal cross section of the TITAN-I FPC illustrating the coil layout.

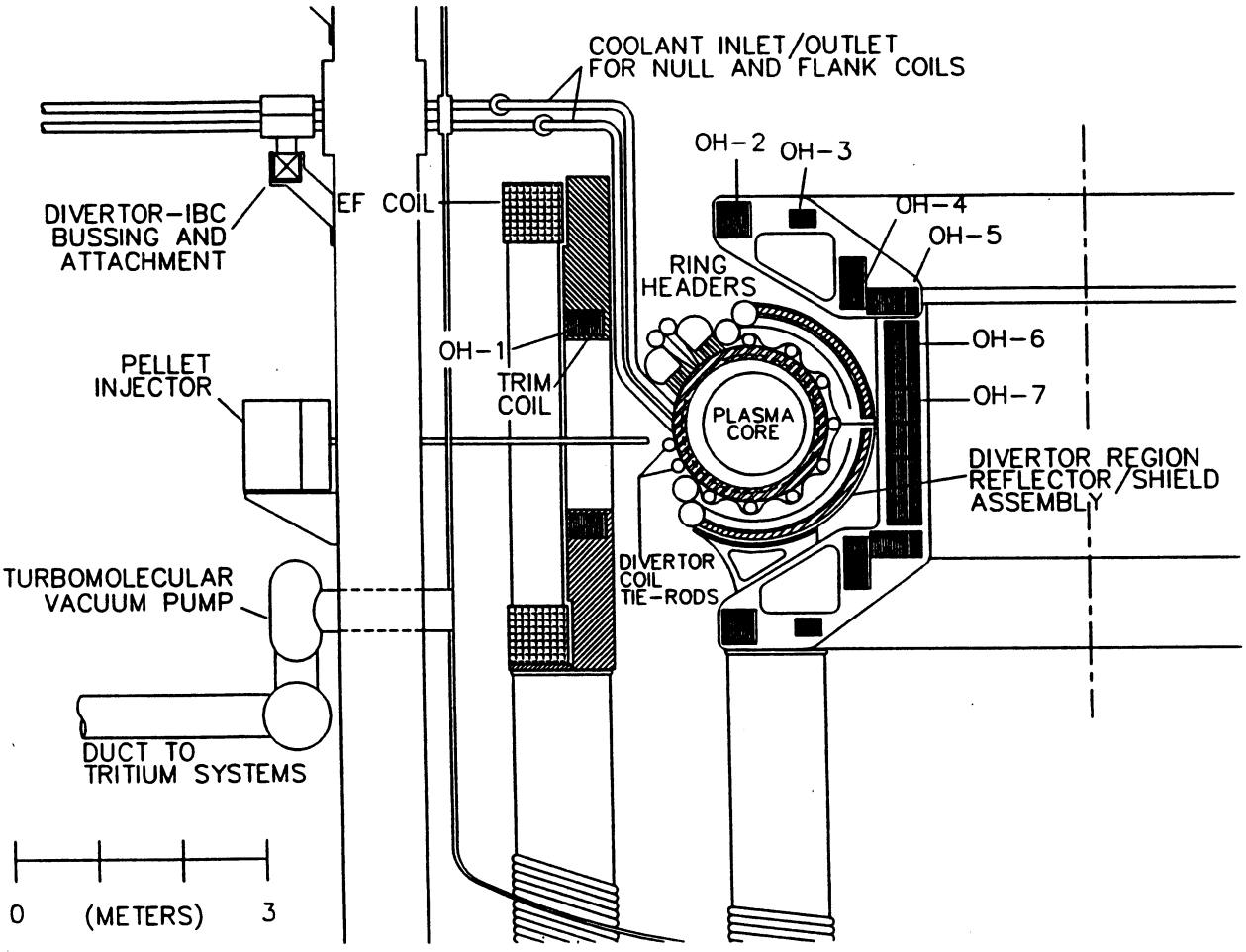

Figure 10.5-2. Poloidal cross section of the TITAN-I FPC through one of the divertor modules, illustrating the divertor IBCs.

Table 10.5-I.

PARAMETERS OF TITAN-I POLOIDAL-FIELD COILS

Function	$R^{(a)}$ (m)	$\pm z^{(a)}$ (m)	$\Delta R^{(a)}$ (m)	$\Delta z^{(a)}$ (m)	$I^{(b)}$ (MA)	$j^{(c)}$ (MA/m^2)	Mass$^{(d)}$ (tonne)	Turns
Trim	5.77	1.20	0.20	0.30	0.	0.	15.9	10
EF	6.50	2.49	0.70	0.70	−9.62	19.78	144.9	88
OH-1	6.00	1.20	0.20	0.30	0.75	12.50	16.5	10
OH-2	4.11	2.41	0.40	0.42	2.10	12.50	31.7	28
OH-3	3.29	2.40	0.30	0.20	0.75	12.50	9.1	10
OH-4	2.71	1.65	0.30	0.60	2.25	12.50	22.4	30
OH-5	2.25	1.43	0.60	0.30	2.25	12.50	18.6	30
OH-6	2.15	0.81	0.40	0.78	3.90	12.50	30.8	52
OH-7	2.15	0.21	0.40	0.39	1.95	12.50	15.4	26

(a) Each coil has a mean radius of R, a height of z (coils are symmetric about the equatorial plane), and a cross section of $\Delta R \times \Delta z$.

(b) Mean steady-state values for the EF coils and back-bias values for the OH coils for a symmetric bipolar swing.

(c) Averaged over the entire coil cross section.

(d) A density of 7.3 tonne/m^3 is assumed.

coils to their full back-bias values. The OH coils are then discharged into a transfer resistor, while the EF coils are connected in parallel to the OH coils ("Formation and fast discharge" phase in Figures 10.5-3 and 10.5-4). The value of the transfer resistor is set by the constraint on the maximum voltage across the superconducting EF coils. The fast-discharge phase lasts about 1 to 2 seconds.

As the OH coils are discharging, the voltage across the circuit drops. When the voltage across the OH coils reaches that of the grid power supply, the transfer resistor is disconnected from the circuit and the grid power supply is directly applied to the OH and EF coils ("Slow-ramp" phase). The OH coils are driven to their full, forward-bias current value and the EF coils and the plasma to their respective steady-state currents. The voltage of the grid power supply is usually a few kilovolts and its value is determined by the maximum power from the grid. The current-drive system begins operation during this phase and will be fully operational at the burn phase, maintaining the steady-state current in the plasma. With the proper magnetics design of the OH and EF coils, this start-up scenario will provide approximate plasma equilibrium throughout the start-up sequence (Section 6). A pair of small, normal-conducting trim coils are used to maintain exact equilibrium during the start-up sequence and are also used during the steady-state operation for plasma-equilibrium control and OFCD cycles (Section 7). After achieving the steady-state burn condition, the OFCD system is initiated while the OH coils are discharged slowly, from the full forward-bias current value to zero, in order to minimize the recirculating power and the coil-cooling requirements. Initiation of OFCD operation during the slow-ramp phase is advantageous.

The electrical requirements for each of the 14 OH coils are listed in Table 10.5-I for a symmetric bipolar swing (*i.e.*, forward- and back-bias current values are the same). Electrical engineering aspects of OH and EF coils (voltages and power consumption) are discussed in Section 6. In this section, magnetic engineering issues such as removal of joule heat during the current swing, and the magnetic forces on the coils and associated support structure are discussed. Some of the features of the TITAN-I final PF-coil design which mitigate these concerns are: (1) the lower value of the current density in the OH coils has reduced the joule losses, (2) the inner OH coil (coils 6 and 7) are positioned in a vertical stack to simplify the design of the support structure and to help ease the FPC maintenance, and (3) the distance between the EF coil and OH-1 (the OH coil closest to the EF coil) is increased to reduce the vertical forces on both OH-1 and EF coils during the start-up sequence.

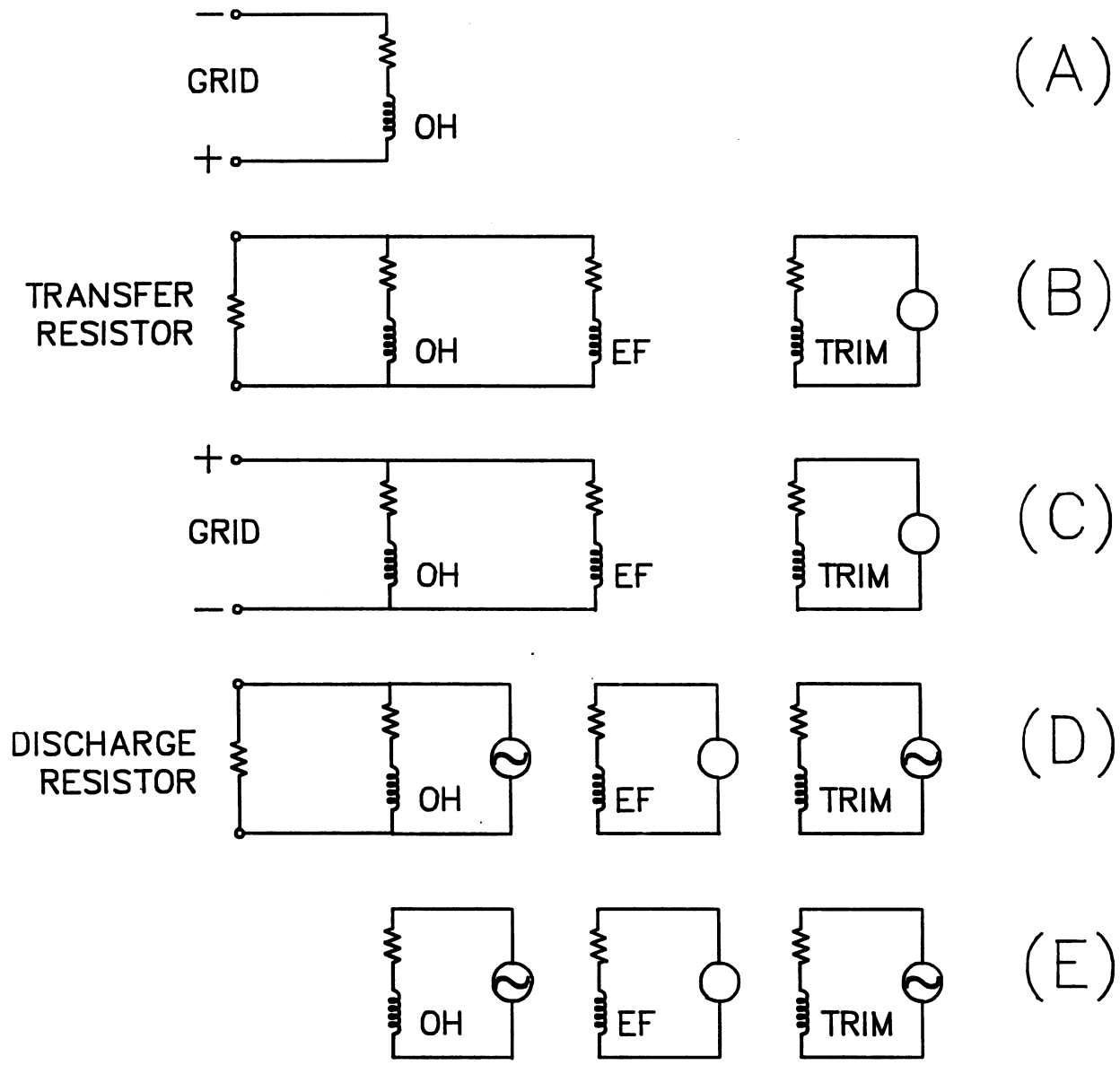

Figure 10.5-3. Start-up sequence for the TITAN-I reactor: (A) Charge-up – OH coils are charged to full back-bias value, (B) Formation and fast discharge – OH coils are discharged through a transfer resistor (EF coils are connected in parallel to the OH coils), (C) Slow ramp – grid power drives the OH coils to full forward bias current and the EF coils to their steady-state value, (D) Transition – the OH coils are slowly discharged while OFCD is initiated, and (E) Steady state – current-drive system is fully operational. Initiation of OFCD operation during the slow-ramp phase is advantageous.

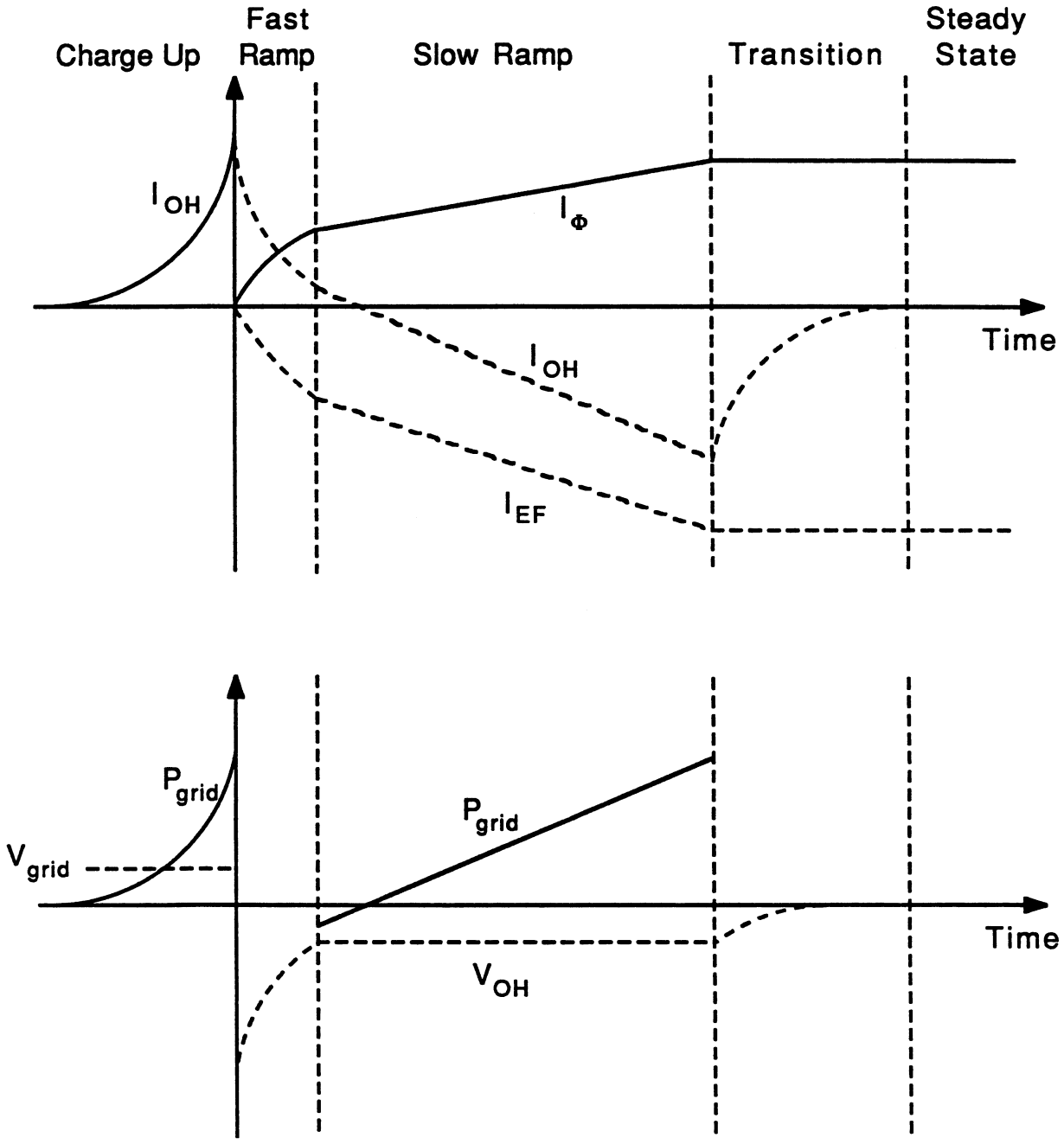

Figure 10.5-4. Schematic of coil currents and voltages during the TITAN-I start-up sequence corresponding to Figure 10.5-3: (A) Charge-up, (B) Formation and fast-discharge, (C) Slow-ramp, (D) Transition, and (E) Steady-state phases. Note that the time axis is not in scale.

10.5.1.1. Heat removal

During normal operation, about 14 MW of heat is generated in the OH and trim coils by the OFCD cycles (OH and trim magnets are also the poloidal-field drive coils of OFCD) as well as by nuclear heating. During the start-up sequence which lasts about 120 s, however, a much larger amount of heat is produced in the OH coils with peak heating rates in the range of 200 to 300 MW (depending on the details of the start-up sequence such as the charge-up time, maximum power from the grid, *etc*). The TITAN-I OH-magnet cooling system is designed only to handle the steady-state load of normal operation. The additional joule heating in the copper conductor of the OH coils during the start-up sequence ($\sim$ 200 J/cm^3) is absorbed by the coils, and adiabatically raises the temperature of the copper conductor by about 60 °C (from 20 to 80 °C).

The internal design of the OH coils is shown in Figure 10.5-5. Coolant channels are provided on one face of the conductor while the insulator material, spinel ($MgAl_2O_4$), is plasma-sprayed on the opposite face. The conductor is then packed in a double-pancake form. The current enters the top pancake and exits through the bottom one, as is shown in Figure 10.5-5 (the coolant channel inside the conductor is aligned in the vertical direction in this figure). A coolant plenum is added inside each coil casing and is fed by six coolant inlets, located 60° apart in the toroidal direction. The helium coolant in the plenum enters between the two pancakes, flows vertically through the coolant channels in the conductor, and exits at the top and bottom into the two outlet plena. The inlet and exit temperatures of the helium coolant are, respectively, 20 and 80 °C during the normal operation of the reactor. For a coolant pressure of 20 atm, the total coolant flow rate (OH and trim coils) is about 14 m^3/s, resulting in a peak velocity of about 5 m/s in each coil. Lower-pressure coolant could be used but would result in a higher coolant velocity in the coils.

The coolant for the OH-2 through OH-7 coils is supplied through six pairs of vertical manifolds. Each pair is located 60° apart in the toroidal direction and feeds into the corresponding inlet and outlet of each OH coil. Assuming a maximum coolant velocity of 20 m/s in the manifolds, the diameter of each manifold would be about 30 cm; smaller size manifolds are also possible but require a higher coolant velocity. The coolant for OH-1 and trim coils is supplied through the EF shield (see Figure 10.5-1) which also cools the shield itself.

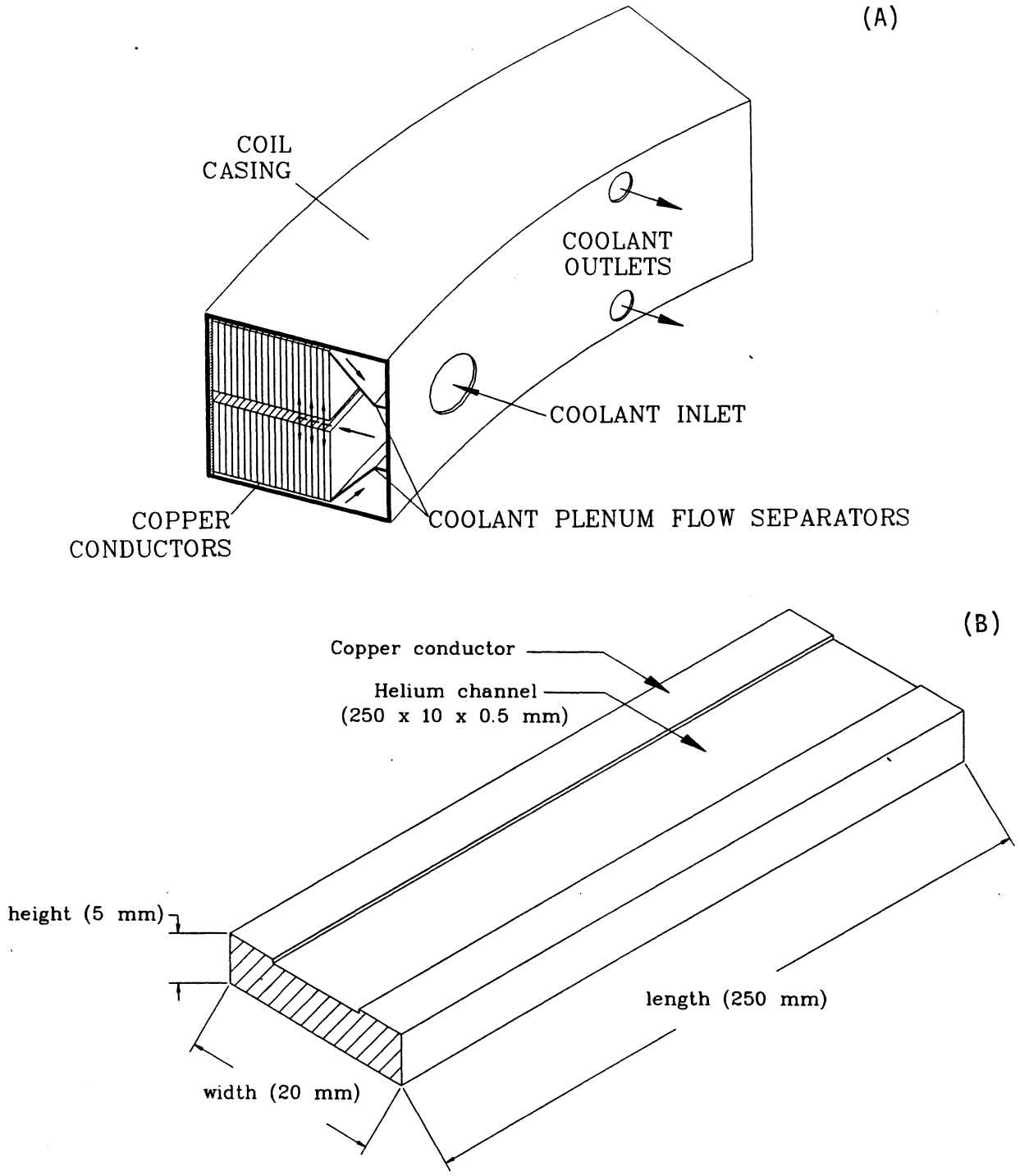

Figure 10.5-5. The cross section of one of the TITAN-I OH or trim coils (A) and the conductor for the OH and trim coils (B). A coolant channel is provided on one face of the conductor with the insulator material plasma-sprayed on the opposite face.

Table 10.5-II.

VERTICAL FORCES ON PF COILS DURING START-UP (MN)

Coil	Back Bias	Forward Bias
Trim[a]	0.	0.
EF[b]	0.	−59.8
OH-1	−3.2	35.1
OH-2	−30.1	19.3
OH-3	−15.6	−1.1
OH-4	−43.8	2.9
OH-5	−38.2	−8.0
OH-6	−22.3	16.0
OH-7	−4.6	1.7

(*a*) Peak force on trim coils is about -20 MN.

(*b*) Peak repulsive force on EF coils is about +40 MN, average force during steady-state operation is -43.9 MN.

10.5.1.2. Support structure for OH coils

The vertical forces on the upper OH coils during the start-up sequence are tabulated in Table 10.5-II. Negative values indicate forces towards the equatorial plane (attractive forces between each pair of coils). Because of the up-down symmetry of the coil set, the forces on lower coils are equal and opposite to those of the upper coils. Vertical forces on coils OH-4 through OH-7 are directly transmitted through the vertical stack of the coils. Vertical forces on the OH-1 and trim coils are much smaller than the weight of the upper EF shield and are supported by 12 columns between the upper and lower EF shields. The vertical forces on the EF coils are supported by 12 cold (cryogenic) columns. The oscillating forces on the TITAN-I coil system during OFCD cycles are described in Section 10.5.3.4.

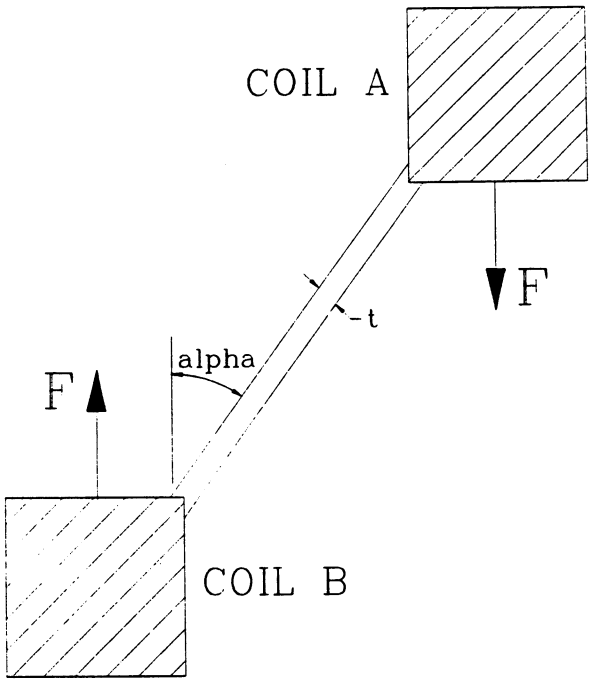

Figure 10.5-6. The model geometry used for buckling analysis of the conical-shell support structure for the OH coils.

The support scheme for OH-2 and OH-3 coils uses a conical-shell framework, as is shown in Figure 10.5-1. The force of each coil is carried between neighboring coils by conical shells of structural steel. Structural requirements were determined by calculating the buckling force and applying a safety factor of 6. The required thickness of the support-shell, t, is given by [129]

$$t = \left[\frac{6F\sqrt{3(1-\nu^2)}}{2\pi E\cos^2\alpha}\right]^{1/2}, \qquad (10.5\text{-}1)$$

where F is the applied load (from Table 10.5-II), ν is Poisson ratio, E is Young's modulus, and α is the angle measured between the conical shell and vertical direction. Figure 10.5-6 illustrates the geometry. The calculated thicknesses of the conical shell for $\nu = 0.3$ and $E = 193$ GPa are listed in Table 10.5-III. Explicit dynamic analysis of the support structure was not performed. The safety factor of 6 takes into account the reversing stresses, from compression to tension [128]. The support shells are continuous in toroidal extent to avoid asymmetric sagging along the toroidal length of the coil.

10.5.2. Equilibrium-Field Coils

The TITAN-I design has only two superconducting coils, the equilibrium-field (EF) magnets. These coils are horizontal, circular coils with a mean radius of ~ 6.5 m and are located about 2.5 m above and below the midplane of the device. The diameter of these coils is chosen so that there is sufficient radial clearance between the coil and the FPC to allow vertical removal of the torus during annual maintenance. The coils are designed to last the lifetime of the plant and can, therefore, be permanently installed. A robust support system and adequate nuclear shielding will ensure that normal reactor transients will have little or no effect on the EF coils. Typical operating currents of the EF coils are listed in Table 10.5-I, and the magnetic forces are listed in Table 10.5-II.

The TITAN-I superconducting EF coils are made of NbTi conductor and steel structure. Because of their permanent nature, simple geometry, and the relatively low field produced by these coils, little or no extrapolation of current technology should be required. Therefore, detailed engineering analyses of the cryogenics systems, conductor design, and internal design of the coils, were not performed.

The TITAN-I design also uses a pair of small, normal-conducting EF-trim coils (Figure 10.5-1 and Table 10.5-I). The trim coils help to produce the exact equilibrium

Table 10.5-III.

THICKNESS OF STRUCTURAL-SUPPORT SHELL

Between Coils	Angle, α	Shell Thickness (cm)
OH-2 & OH-4	55°	2.7
OH-3 & OH-4	45°	1.6
OH-4 & OH-7 [(b)]	20°	3.1[(a)]
OH-5 & OH-7 [(b)]	–	5.7[(a)]
OH-6 & OH-7 [(b)]	–	6.7[(a)]

(*a*) Based on compressional stress and not buckling.

(*b*) Carries the forces of the upper coils.

field during the start-up sequence and the OFCD cycles, and are used for controlling the plasma position during the steady-state burn. The design of the trim coils is similar to that of the OH coils and these trim coils are cooled and supported by the OH-coil cooling system and support structure (Section 10.5.1).

10.5.3. Integrated Blanket Coils (IBCs)

The divertor and the TF coils of the TITAN-I design are based on the integrated-blanket-coil (IBC) concept [104]. The IBC concept utilizes the lithium coolant of the primary circuit, flowing in the poloidal direction within the blanket, as the electrical conductor for the divertor and TF coils. Although the electrical resistivity of lithium is about 20 times that of copper, the low toroidal-field requirement of the RFP, combined with the large cross-sectional area available to the IBC and the recovery of the joule losses by the primary coolant, results in acceptable power requirements for the divertor and TF coils. The joule losses in the TITAN-I divertor and TF coils are, respectively, 24 and 120 MW.

The TITAN-I IBC also acts as the toroidal-field driver coil for the OFCD system. Intrinsic plasma processes in RFPs generate voltages and currents within the plasma in order to maintain the plasma in a near-minimum-energy state. This nonlinear coupling between the toroidal and poloidal magnetic fluxes in the plasma can be used to rectify current oscillations created at external coils into a net steady-state current in plasma. Detailed magnetics design of the TITAN-I OFCD system is reported in Section 7. The TF coils of TITAN-I oscillate at 25 Hz with TF-coil currents ranging between 30% and 170% of the mean steady-state value of 7.0 MA-turns (including the current in the divertor trim coils). The poloidal-field system also oscillates at 25 Hz. It is also necessary to oscillate the divertor coils to maintain the plasma separatrix at the proper location.

Several critical engineering issues which have been identified for the IBC design adopted for TITAN-I are: (1) steady-state and oscillating (OFCD) power-supply requirements for low-voltage, high-current coils; (2) time-varying forces caused by the OFCD cycles; (3) integration of the primary heat-transport system with the electrical systems; (4) sufficient insulation to stand off induced voltages; and (5) suitable time constants for various components to permit the coil currents to oscillate at 25 Hz. Heat removal is not an issue for the IBC because the joule heating is produced directly in the primary coolant.

10.5.3.1. Electrical engineering of toroidal-field IBC

Design of the power supplies is one of the critical issues in the engineering of the TF IBC because the IBC approach requires that the electrical and hydraulic systems be physically connected. These connections must be (1) made in the proper location to ensure that the electric current flows in the correct direction through the coils and (2) made away from the remote connect/disconnects of the hydraulics system in order to minimize the number of remote operations during torus replacement. Another operational constraint is that the intermediate heat exchangers (IHXs) and coolant pumps should be grounded (no electric current flowing through them).

Each TF IBC in TITAN-I is a one-turn coil with low voltage and high current (3.85 V, 520 kA per coil). Power supplies rated for such conditions would be expensive and would exhibit high internal-power losses if based on currently available technology. Large homopolar generators would have lower losses but they are a future technology. Connecting all TF IBCs of TITAN-I in series and/or providing more electrical turns in each IBC would raise the voltage of the power supply to a more manageable value. This method had to be ruled out, however, because of thermal-hydraulic considerations.

Figure 10.5-7 illustrates the electrical and hydraulic layout of the TITAN-I IBC system. The TITAN-I FPC comprises three sectors which are connected to each other through the divertor modules. To increase the power-supply voltage, the four IBCs in each sector are electrically connected in series which allows a better match of current and voltage for the power supply (15.4 V, 541 kA). This circuit, however, requires two IHXs per sector for the IBC-cooling circuit.

The TITAN-I TF IBC has the following resistances: each IBC coil, $R_{TF} = 7.40\,\mu\Omega$; the cold leg of the coolant, $R_c = 142\,\mu\Omega$ (from the coolant pumps to the FPC); and the hot leg of the coolant, $R_h = 366\,\mu\Omega$ (from FPC to the IHX). Figure 10.5-7 shows that, because of the series connection of the IBCs and grounding of the pumps and heat exchangers, a leakage current will flow through the cold and hot legs. The leakage current is small in magnitude but causes unequal coil currents, necessitating a small balancing power supply to accompany each main power supply. The load on each balancing power supply (7.7 V, 27 kA) is much smaller load than that of the main power supply (15.4 V, 541 kA) and leaks through the cold legs to ground.

The piping layout (also shown in Figure 10.5-7) between the coils and heat exchangers is consistent with the flow paths and electrical circuit developed to minimize the current leakage. As a result, the electric current and coolant flow opposite to one another in two of the four TF coils in each sector. In the other two coils, the current and coolant

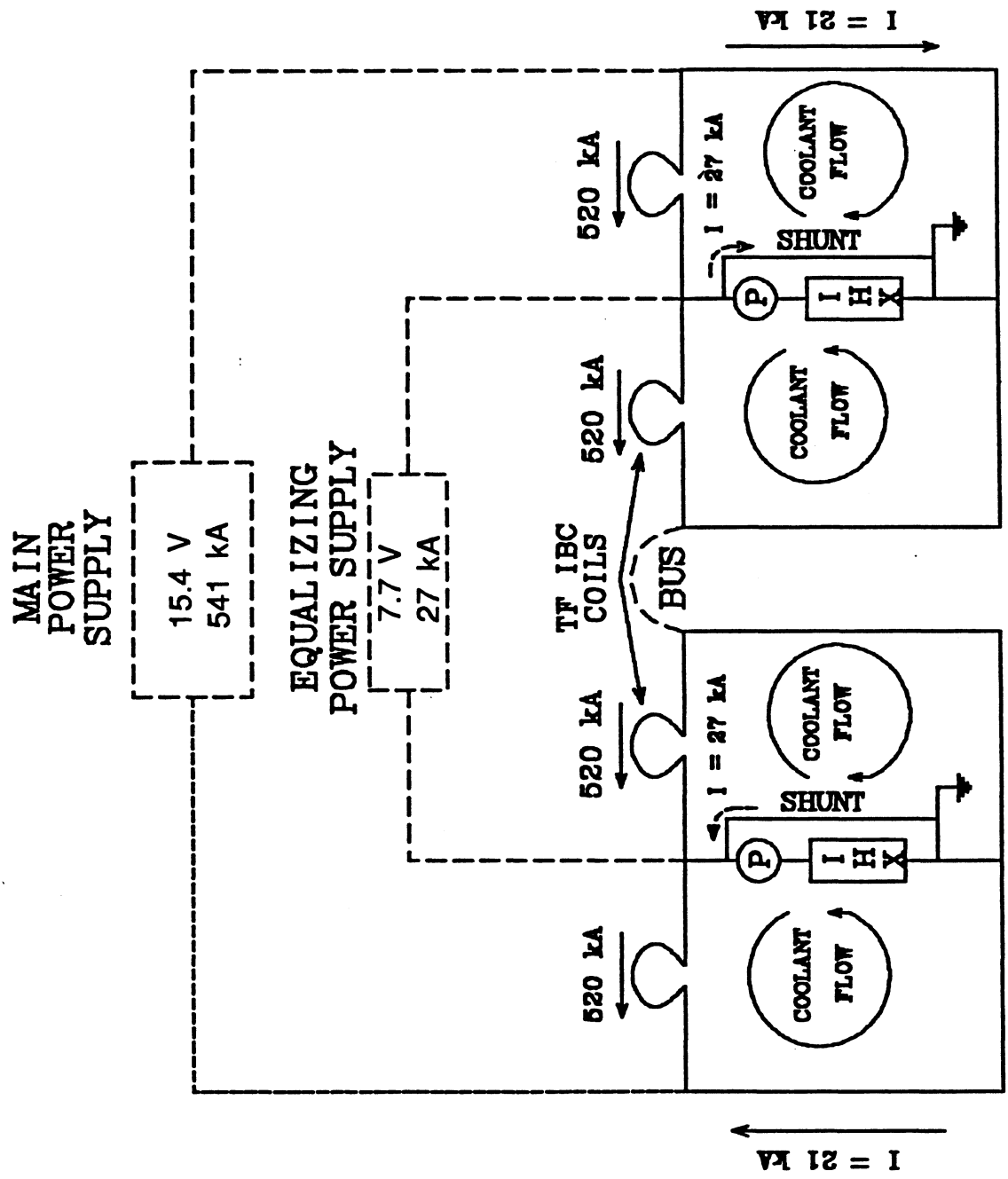

Figure 10.5-7. Schematic of the electrical and hydraulic layout of TITAN-I TF IBCs.

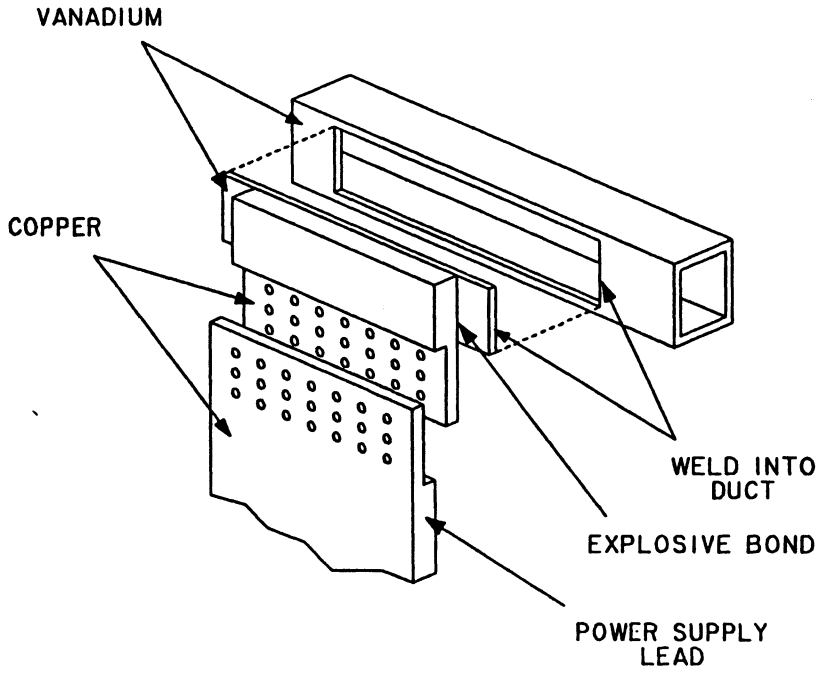

Figure 10.5-8. Electric bussing attachment to lithium duct.

both flow from the cold leg to the hot leg. Figure 10.5-8 shows the electrical bussing attachment of the power-supply leads to the lithium duct. Based on this design, the joule losses in all 12 TF coils are about 24 MW with an extra 1.95 MW of heating in the hot and cold legs.

10.5.3.2. Electrical engineering of divertor IBC

The impurity-control system of the TITAN-I design consists of three toroidal-field divertors (Section 5). Each divertor consists of one nulling coil and two flanking coils to produce the local effects necessary for field nulling. Because of the loss of coverage of TF IBCs in the divertor region, a pair of trim coils is added to each divertor in order to control the toroidal-field ripple and to minimize the toroidal extent of the perturbation. The detailed magnetics design of the IBC divertor coils is given in Section 4. The poloidal cross section of the TITAN-I FPC through one of the divertor modules is shown in Figure 10.5-2, illustrating the divertor IBCs.

The divertor IBCs operate at somewhat higher current densities than the TF coils, thereby requiring much greater voltages. Furthermore, the current in each nulling coil is exactly equal to that of the two flanking coils. The divertor IBCs are connected in

order to take advantage of the symmetric currents and larger voltages. Figure 10.5-9 shows the electrical and hydraulic layout of the divertor IBCs. The resistances of the nulling, flanking, and trim coils are, respectively, 0.47, 0.93, and 0.43 mΩ. The resistance of the hot leg is estimated to be 29 mΩ. Because the resistance of the cold leg is larger than that of the hot leg, the power supplies are grounded at the cold leg location; an arrangement similar to that of Figure 10.5-7 would require a current to flow to ground inside the power supply.

Only two power supplies per divertor module are required because the equalizing power supplies are not needed for the divertor IBCs (Figure 10.5-9). The first power supply, rated at 147.75 V and 169 kA, feeds the null and flanking coils. The second power supply, rated at 11.64 V and 135 kA, feeds the trim coils. The joule losses in the divertor IBCs (three divertors) are 117 MW with an additional 3.5 MW in the hot legs.

10.5.3.3. OFCD power supplies

The TITAN-I design operates at steady state using an oscillating-field current-drive (OFCD) system. Detailed magnetics design of the TITAN-I OFCD system is reported in Section 7. The TF coils of TITAN-I oscillate at 25 Hz with TF-coil currents ranging between 30% to 170% of the mean steady-state value of 7.0 MA-turns (including the current in the divertor trim coils). It is also necessary to oscillate the divertor coils to maintain the plasma separatrix at the proper location.

Inductive coupling of the reactor components (*e.g.,* the TF and PF coils, plasma, plasma liner or first wall, and other conducting material surrounding the FPC) causes time delays in the current rise and fall, and induces voltage drops in addition to that caused by the resistance of the components. Therefore, the following requirements emerge: (1) IBC power supplies should be able to provide adequate steady-state and oscillating voltages and currents, (2) sufficient insulation should be added to standoff induced voltages, (3) suitable time constants for various components are required to permit the coil currents to oscillate at 25 Hz, and (4) the coil busing must be resized to handle the peak load.

Oscillation at 25 Hz requires a peak-to-minimum discharge time of 20 ms. The time constant for the TF IBC is calculated to be $\sim$ 3.2 ms; therefore, more than six IBC time constants will elapse over the discharge period. The skin depth for the OFCD currents in the IBC was taken into account in calculating the performance of the OFCD system (Section 7). Also, the peak induced voltage by the OFCD cycles across a four-coil TF-IBC sector is about 400 V which is easily manageable by the spinel insulator.

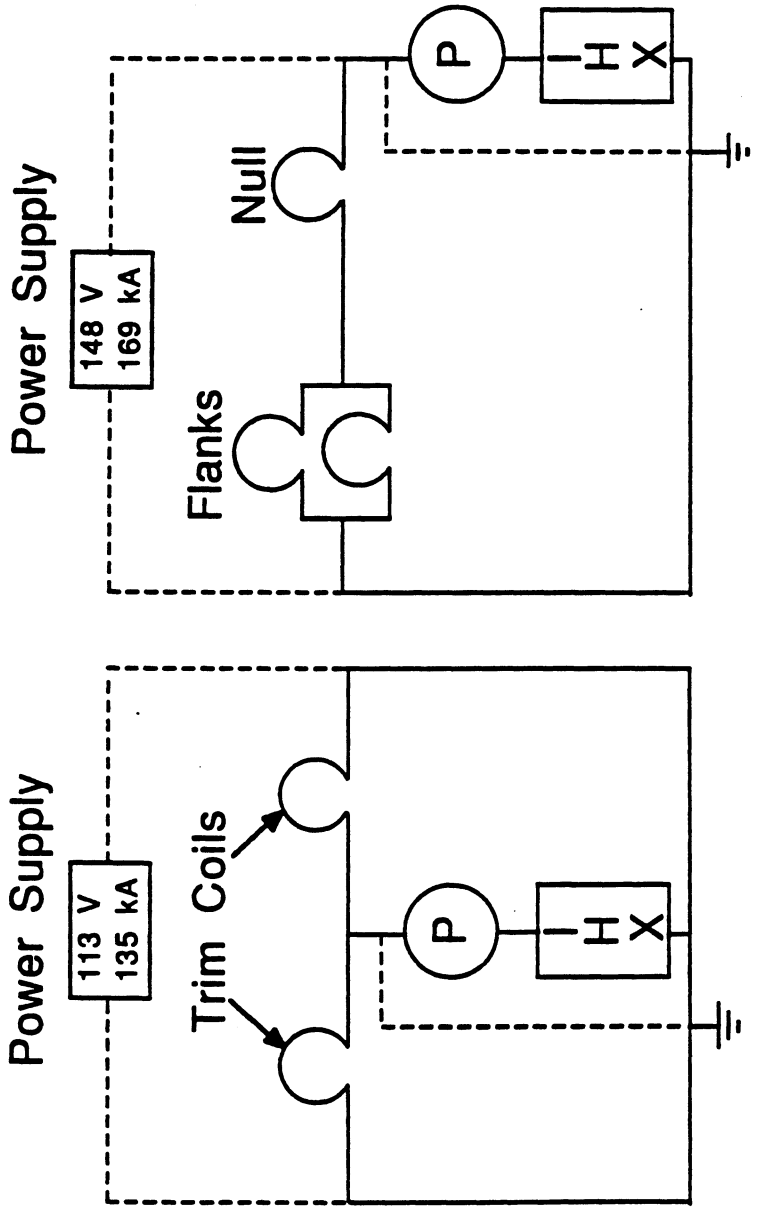

Figure 10.5-9. Schematic of the electrical and hydraulic layout of TITAN-I divertor IBCs.

The power supply criteria listed above can be met in principle by using steady-state systems for the nominal values (Figure 10.5-8) and adding an additional oscillating supply to superimpose the required voltage and current variations. However, because of the large impedance of the toroidal-field circuit during the OFCD cycles (about 0.1 mΩ for each TF coil), the oscillating voltage on each TF coil ($\sim$ 50 V) is much larger than the steady-state value ($\sim$ 3.8 V). If the impedance of the hot and cold legs is dominated by their resistances, the resulting joule heating in the hot and cold legs during the OFCD cycle would be much larger than the power supplied to the TF coils (Figure 10.5-8). Therefore, the design of the OFCD power supplies should take into detailed account the impedances of the hot and cold legs which in turn depend on the piping arrangement.

Detailed analyses of the OFCD power supplies and the leakage currents were not performed because of the complexity of the problem and because the results are very sensitive to the detailed arrangement of the pipings; the TITAN-I design is not in sufficient detail to warrant this level of electrical analyses. Instead, the leakage currents were calculated based on simple estimates of the internal inductances of coolant pipings. The internal inductances of the hot and cold legs of the TITAN-I design, based on low-frequency estimates for a round wire, are calculated to be in the range of 4 to 8 μH (0.6 to 1.2 mΩ) which would reduce the currents and, therefore, the joule losses in the hot and cold legs substantially. Since the direction of the leakage currents in adjacent hot legs or adjacent cold legs are different (Figure 10.5-8), the mutual inductances between these legs could also be exploited by pairing the appropriate legs to further increase the impedances, thereby reducing the leakage currents and the joule losses in the hot and cold legs.

It is necessary to oscillate the divertor coils during the OFCD cycle to maintain the plasma separatrix at the proper location. The OFCD analysis in Section 7 was performed assuming full coverage by TF coils, and the impact of the divertor coils was ignored. This analysis showed that the reversal parameter, F, ranges between -0.032 to -0.173 about the mean value of -0.1 during the OFCD cycle. Since the magnitude of oscillation of the toroidal flux was found to be small, the strength of the toroidal field on the plasma surface would be directly proportional to the reversal parameter, and the magnitude of the current oscillations in the divertor coils would be about 2/3 of the steady-state value. The voltage oscillations applied to the divertor coils are roughly equal to the steady-state values, in contrast to the TF coils, because the divertor coils operate at much higher current densities and have higher resistances.

The analysis in Section 7 for the performance of the OFCD is scaled to include the impact of the divertor coils. This analysis of full-coverage TF coils predicts 18.23 and

29.15 MW of joule heating in the TF coils, respectively, for oscillating and steady-state portions. Noting that steady-state joule losses in the TF coils in the presence of the divertor coils (Section 4) are 24 MW, the joule losses in the TF coils during the OFCD cycle are estimated to be 25.6 MW for the steady-state portion (24 MW in the coil and 1.6 MW in the hot and cold legs) and 16 MW for the oscillating voltages (15 MW in the coils and 1 MW in the hot and cold legs).

The steady-state joule losses in the divertor coils were found to be 117 MW in the coils (Section 4) and 3.5 MW in the hot and cold legs (Section 10.5.3.2). Assuming that current oscillations in the divertor coils would be 2/3 of the steady-state value, the oscillating losses are estimated at 26 MW in the coils and 0.8 MW in the hot and cold legs. The resulting OFCD power-supply parameters for the divertor and TF-IBC systems are listed in Table 10.5-IV.

During the start-up sequence, particularly during the initial RFP-formation phase, the TF coils must be able to swing from a small positive current (12 kA) to a small negative current (-1.2 kA) within 10 ms. The circuit time constant of the TF IBC is calculated to be ~ 3.2 ms, therefore $\sim 95\%$ of the current swing will occur within the allotted 10 ms. The voltage induced by the start-up transient would peak at ~ 70 V, of the same order as the peak induced voltage by OFCD cycles. A thin layer of spinel insulator can withstand this voltage, even allowing for significant degradation resulting from radiation damage.

10.5.3.4. Oscillating coil forces

Interaction of the TF-IBC current with the reactor magnetic fields produces forces on the coils. These forces are of three kinds: (1) over-turning moments generated by the interaction of the IBC current with the vertical field, (2) centering forces resulting from the radial variation of the toroidal field, and (3) out-of-plane forces caused by the spatial variation of the magnetic fields near the separation of TF coils created by the divertor.

The magnitudes of the forces on the TITAN-I TF IBCs vary over time as the currents oscillate during the OFCD cycle. Structural support, therefore, is designed for the peak loads, as is listed in Table 10.5-V. These forces are much lower than the corresponding forces in tokamaks, since the coil currents are much lower in RFPs.

The OFCD cycles generate oscillating forces on the TF-IBC tubes. If the driving frequency is at or near the resonant frequency of the structure, large deformations and stresses can result, causing fatigue failure or catastrophic rupture. To assess the effect of

Table 10.5-IV.

PARAMETERS OF TITAN-I IBC POWER SUPPLIES

TF-IBC Power Supplies	Main	Balancing
Steady State		
Voltage (V)	15.4	7.7
Current (kA)	541.	27.
Cost (M$)	2.75	0.25
Oscillatory		
Voltage	200.	100.
Current	420.	21.
Cost (M$)	5.25	0.25
Busing cost[(a)] (M$)	7.1	0.35
Total cost per sector (M$)	15.1	0.85
Divertor-IBC Power Supplies	Null/Flank	Trim
Steady State		
Voltage (V)	148.	113.
Current (kA)	169.	135.
Cost (M$)	3.0	2.25
Oscillatory		
Voltage	200.	160.
Current	113.	90.
Cost (M$)	3.0	2.25
Busing cost[(a)] (M$)	2.2	1.8
Total cost per sector (M$)	8.2	6.3

(*a*) Based on a unit cost of 60 $/kA-m.

Table 10.5-V.

PEAK FORCES ON TOROIDAL-FIELD IBC TUBES

	Average	Peak
Over-turning moment (kN m)	$\sim 0.$	1.6
Centering force (kN)	−0.1	−0.7
Out-of-plane force (kN)	1.6	−4.0

these oscillating forces on the lifetime of the TF-IBC tubes, a dynamic analysis must be performed to calculate the strain range experienced by the IBC tubes during each cycle and the result then compared to the minimum-strain range that will cause fatigue failure in V-3Ti-1Si.

The OFCD system produces both in-plane and out-of-plane forces which oscillate about some small average value. The cyclic in-plane forces are shown in Figure 10.5-10. The small steady force on the coolant tubes has little effect on the analysis of the cyclic strains induced by the OFCD. A key aspect of dynamic structural analysis concerns the resonant frequency of a cyclically loaded component. If the loading frequency is at or near the natural frequency of a particular deformation mode and the loads excite that mode, then very small loads can cause relatively large strains and deformations. A finite-element model was used to calculate the natural frequencies and mode shapes of the IBC tube. The IBC tube was modeled as a poloidal hoop with 60 two-node beam elements and two free ends that represent the inlet and outlet headers. The natural frequency of the out-of-plane deformation modes can be controlled by tying neighboring TF-IBC tubes together, thus increasing the lateral stiffness of the structure. This method raises the resonant frequency of the out-of-plane modes and is expected to prevent excessive strains caused by over-turning moments on the tubes. Hence, only in-plane forces and vibrations will be considered here.

The presence of the coolant has an impact on the natural frequency of the TF-IBC tubes. The tubes themselves provide all the structural stiffness of the component, but the added weight of the coolant changes their inertia, thereby lowering the natural frequency of the combined structure. This effect was modeled by increasing the density of the

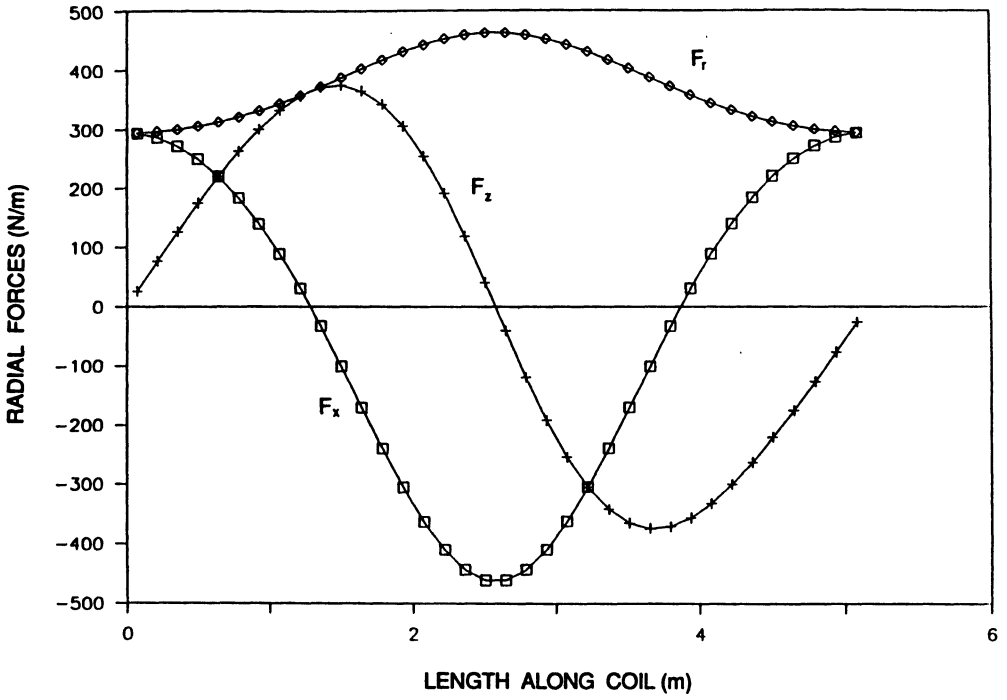

Figure 10.5-10. Cyclic, in-plane forces induced in TF-IBC tubes by the OFCD system.

vanadium tubes from 6100 kg/m^3 to an effective density of 8232 kg/m^3. This correction was calculated assuming that the total mass of the tube and coolant cross section is contained in the tube wall.

The lowest-frequency in-plane mode is basically a rotation about the attachment points at the ends of the straight portions of each IBC tube. The natural frequency of this mode is 5.4 Hz, which is well below the OFCD frequency. The natural frequencies of the next two in-plane vibration modes are 25 and 44 Hz. Fortunately, the in-plane forces are primarily radial, so no force exists to excite this mode. In addition to these bending modes, there are extensional deformation modes, the most fundamental of which represents a uniform radial deflection of the tube. These modes are always stiffer than the bending modes. For a complete ring, the natural frequency for this mode is about 1100 Hz, so the resonance of extensional deformation modes should not be a problem for TITAN-I. Because the oscillating forces caused by the OFCD are primarily radial, they will tend to excite the extensional modes and resonance should not be a problem.

The TF-IBC cyclic forces (Figure 10.5-10) were examined with a finite-element model to assess the impact of these forces on the blanket design. The peak stress was found to be only 0.3 MPa, corresponding to a cyclic-strain range of 3×10^{-4}%. Since endurance

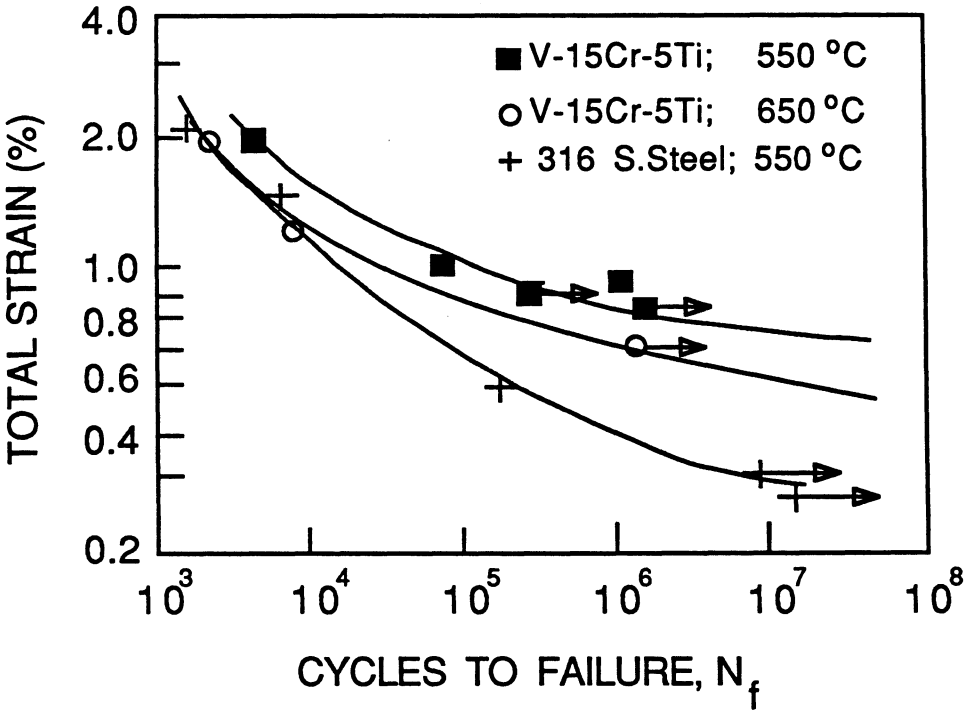

Figure 10.5-11. Fatigue behavior of V-15Cr-5Ti. Arrows indicate the strain value for very large number of cycles.

data were not available for V-3Ti-1Si, data for V-15Cr-5Ti were used. Figure 10.5-11 shows that the OFCD-induced strain range is three orders of magnitude lower than the endurance limit for V-15Cr-5Ti. Therefore, failure is not expected to occur as a result of the cyclic forces induced by OFCD. Compliant layers of metallic fibers are provided between TF-IBC tubes for support. Their resilience, which is not accounted for in this analysis, should dampen the loads even further.

10.6. POWER-CYCLE ANALYSIS

One of the advantages of using liquid lithium as the coolant for TITAN-I is the ability to remove the thermal energy from the reactor at a high thermal potential so that a high power-cycle efficiency can be realized. Both the inlet and exit temperatures of the primary coolant affect the power-cycle efficiency. The inlet temperature affects the pinch point and, hence, the maximum steam pressure in a Rankine power cycle. In a steam generator, the pinch point is the location at which the water temperature reaches the boiling point. At this pinch point, the temperature of the hot fluid must

be higher than the boiling point of water at the desired pressure by some amount for efficient heat transfer. Otherwise, a large heat-transfer area, which would correspond to a large steam generator, is required. The exit temperature determines the maximum steam temperature. High steam pressure as well as high steam temperature are essential for obtaining a high power-cycle efficiency.

The thermal-hydraulic design determines the inlet and exit temperatures of the primary coolant. Details of thermal-hydraulic design of the first wall and blanket are presented in Section 10.4 and the thermal design of the divertor is discussed in Section 11. An important feature of the thermal-hydraulic design of the TITAN-I first wall and blanket is the separation of the coolant circuits for these components in order to handle the high surface heat flux on the first wall. As a result, the first-wall coolant has a much lower exit temperature than that of the blanket and shield coolant. The divertor coolant also has a different exit temperature from those of the first-wall and blanket coolants. In effect, TITAN-I has three separate circuits for primary lithium: the first-wall, the divertor, and the blanket and shield circuits. The inlet temperatures of all three circuits are identical, while the exit temperatures are different. Therefore, several options for the power cycle are available and are discussed in Section 10.6.2. The total thermal power, coolant temperatures, and flow rates in these three circuits are given in Table 10.6-I, and the parameters of the reference power cycle is given in Section 10.6.3.

10.6.1. Secondary-Coolant Loop

The purpose of the secondary-coolant loop is to separate the primary coolant and the containment building from the power-generation cycle (*e.g.*, from water or steam of the steam cycle) for additional safety, even though the secondary loop and the intermediate heat exchanger (IHX) would degrade the thermal potential of the primary coolant. Lithium and sodium were considered for the coolant of the secondary loop. Liquid lithium is preferable to sodium for several reasons: (1) with lithium as the primary as well as secondary coolant, only one type of main coolant would be used in the plant; (2) storage and handling of the coolant would be much easier; (3) the heat capacity of lithium is about twice that of sodium, therefore, the total amount of coolant would be much less; (4) lithium is also less reactive with water than is sodium; and (5) the turbulent-flow heat-transfer capability of lithium is better than that of sodium which could result in smaller surface area in the IHX.

One advantage of sodium is the low solubility of tritium in sodium compared to lithium. Therefore, if sodium is used as the secondary coolant instead of lithium: (1) tri-

Table 10.6-I.

THERMAL-POWER DISTRIBUTION IN TITAN-I

First-wall coolant circuit		
Thermal power	736	MWt
Inlet temperature	320	°C
Exit temperature	440	°C
Coolant flow rate	1464	kg/s
Divertor-plate coolant circuit		
Thermal power	29	MWt
Inlet temperature	320	°C
Exit temperature	540	°C
Coolant flow rate	31	kg/s
IBC and hot-shield coolant circuit[a]		
Thermal power	2170	MWt
Inlet temperature	320	°C
Exit temperature	700	°C
Coolant flow rate	1363	kg/s

(*a*) Including divertor-IBC circuit.

tium inventory in the secondary loop would be smaller by about two orders of magnitude and (2) tritium permeation to the steam cycle might be lower depending on the partial pressure of tritium in the primary coolant. If the salt-extraction method is used to remove tritium from the primary coolant, the tritium concentration in the primary coolant could be reduced to less than 1 appm [5], corresponding to a tritium partial pressure of $\sim 10^{-9}$ torr. Since this pressure is much smaller than the obtainable pressure by cold trap in sodium at 115 °C [130], the maximum partial pressure of the tritium in the secondary coolant (sodium or lithium) and tritium permeation to the steam side would be set by the tritium pressure in the primary coolant. Therefore, the only benefit in using sodium would be the much lower tritium inventory in the secondary coolant. For the TITAN-I design, it was decided that this advantage is not significant and overall it would be advantageous to use liquid lithium also as the secondary coolant.

10.6.2. Power-Cycle Options

The total thermal power of the TITAN-I reactor is removed by three primary-coolant circuits: the first-wall, divertor, and IBC and shield circuits (Table 10.6-I). The inlet temperature of lithium for all three circuits is 320 °C but the exit temperatures are different (respectively, 440, 540, and 700 °C for the first-wall, divertor, and IBC and shield coolants). Of the total thermal power, only about 1% is removed by the divertor coolant, about 25% by the first-wall coolant, and 74% by the IBC and shield coolant. Since the thermal power in the divertor circuit is very small, it would be advantageous to mix the divertor coolant with that from one of the other two circuits. If the first-wall and divertor coolants are mixed at the exit, the mixed exit temperature would be 442 °C, leading to two separate streams of the primary coolant removing, respectively, 765 and 2170 MWt of power with exit temperatures of 442 and 700 °C.

Figure 10.6-1 shows three possible variations of power cycles (A-C) for the TITAN-I design. In (A), the two streams from the first wall and divertor and from the IBC and shield are mixed at the exit (for a mixed exit temperature of 556 °C) and then fed to only one power cycle. In (B), the two coolant streams are partially mixed in a special IHX, resulting in a higher steam temperature and pressure than in (A). Option (C) uses two separate power cycles for the two streams of coolant, one for the first-wall and divertor stream and the other for the IBC and shield stream. Each of these two power cycles has its own IHXs, steam generators, and turbine-generator set.

Power cycle (A) is the simplest and least costly, but it has a lower thermal efficiency compared to the other two options because of its lower primary-coolant exit temperature.

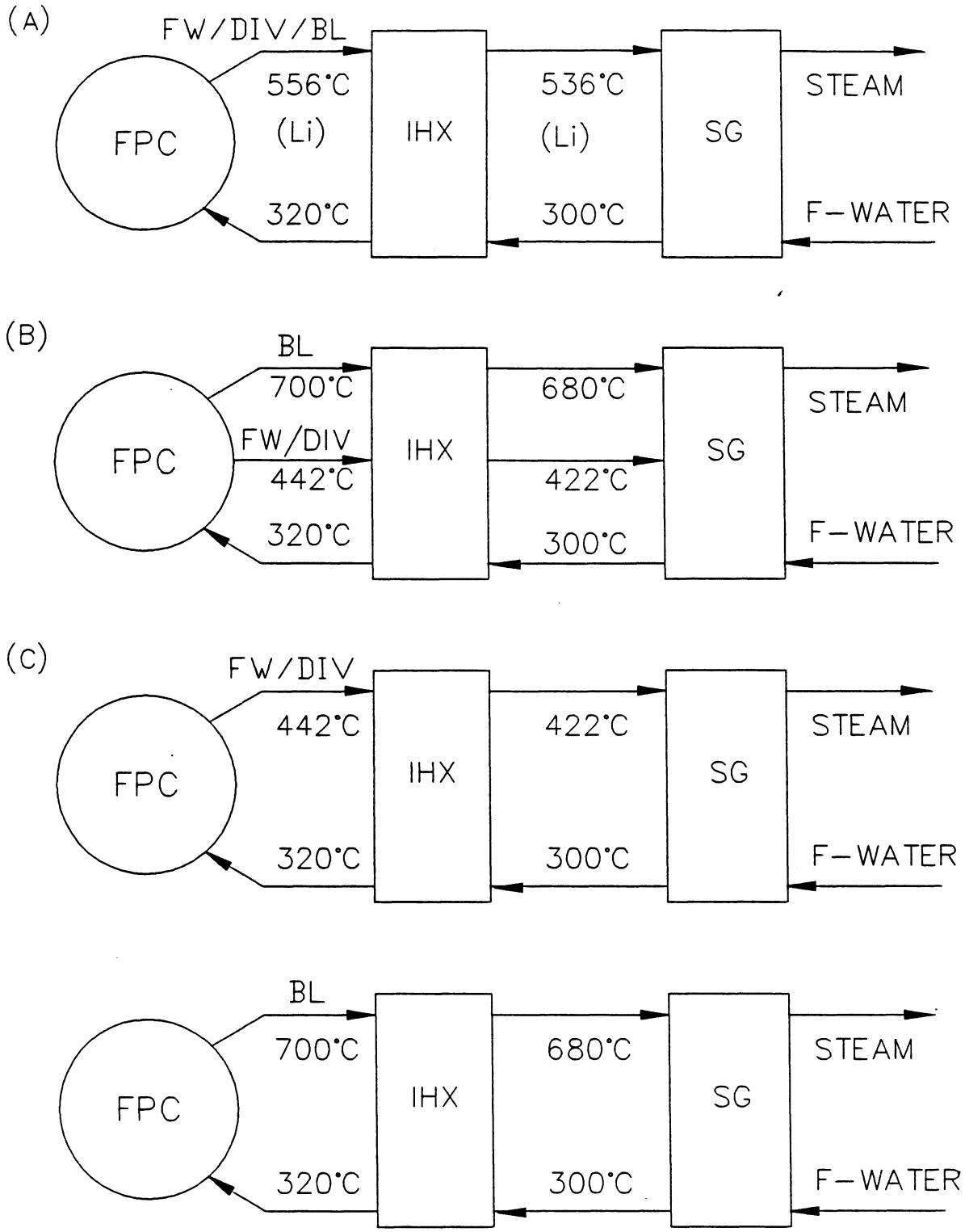

Figure 10.6-1. Power-cycle options for the TITAN-I design.

For power cycle (B), a new and complicated design of the IHX and steam generator is necessary, resulting in a higher capital cost compared to (A). The total capital cost of option (C) is likely to be the highest. The dual power cycles of option (C) are as simple as that of (A); the only difference is the duplication of several components and the increased total capital cost as a result of economies-of-scale. The overall thermal efficiency of option (C) is the highest because the primary-coolant streams are not mixed and the high exit temperature of the IBC and hot-shield coolant is efficiently used.

Economic comparison of the three power-cycle options of Figure 10.6-1 for TITAN-I has shown that option (C) would result in the most economical system because its higher thermal efficiency would offset the extra cost. Therefore, this option has been chosen as the reference power cycle for the TITAN-I design.

10.6.3. Reference Power Cycle

A schematic flow diagram of a reheat power cycle is presented in Figure 10.6-2. In this diagram, one high-pressure turbine (HPT), one reheater, one low-pressure turbine (LPT), and two regenerative feed-water heaters are shown explicitly. An intermediate-pressure turbine is also used in each cycle. The actual number of components varies for the two power cycles of TITAN-I.

The TITAN-I FPC consists of three sectors with one IHX and one steam generator per sector for the first-wall and divertor coolant stream. The steam produced in these three steam generators is mixed and fed to a single turbine-generator set. For the IBC and shield stream, two IHXs are used per sector based on electrical engineering requirements of the IBCs (Section 10.5.3). The secondary coolants of each pair of these IHXs are mixed and fed to one steam generator (per sector). As in the first-wall and divertor cycle, the steam from all three steam generators is mixed and fed to one turbine-generator set.

The power-cycle analysis is performed by the computer code PRESTO [131]. The pinch-point temperature difference in the steam generators of each of these power cycles is kept above 20 °C. For both the first-wall and divertor cycle and the IBC and shield cycle, the temperature drop in the IHXs is set at 20 °C.

Figure 10.6-3 shows the results of the analysis of the TITAN-I reference power cycles as temperature-energy diagrams. The first-wall and divertor power cycle is a superheat Rankine cycle with four stages of feed-water heating. No steam reheat after expansion through the high-pressure turbine is used. The throttle steam conditions (temperature and pressure) are, respectively, 396 °C and 10.7 MPa (1550 psia). The condenser back

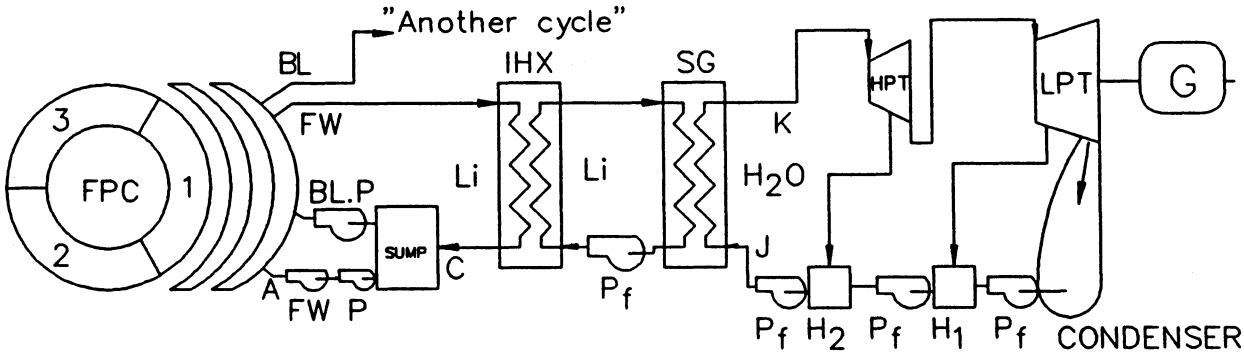

Figure 10.6-2. Schematic of the flow diagram of a reheat power cycle.

pressure is 6.76×10^3 Pa (2 inches of mercury). The inlet temperature of the feed water is 169 °C, and the temperature difference at the pinch point is 21.6 °C. The total thermal power in this cycle is 765 MWt and the steam flow rate is 326 kg/s. The gross thermal efficiency of the first-wall and divertor power cycle is 37.0%.

The IBC and shield power cycle is a superheat Rankine cycle with two reheat stages and seven stages of feed-water heating. The temperature and pressure of the throttle steam are, respectively, 565.6 °C and 21.4 MPa (3100 psia). The maximum steam temperature is limited to 565.6 °C (1050°F), although higher temperatures are reported. The superheater and the reheaters are arranged in series. Figure 10.6-3 also shows the temperature-energy diagram for the IBC and shield power cycle. The condenser back pressure is 6.76×10^3 Pa (2 inches of mercury), similar to that of the first-wall and divertor power cycle. The inlet temperature of the feed water is 258 °C and the temperature difference at the pinch point is 34 °C. The total thermal power in this cycle is 2170 MWt and the steam flow rate is 703 kg/s. The gross thermal efficiency of this cycle is 46.5%.

The main results and parameters of the first-wall and divertor cycle and the IBC and shield cycle are given in Table 10.6-II. The overall gross thermal efficiency for the TITAN-I design is 44%.

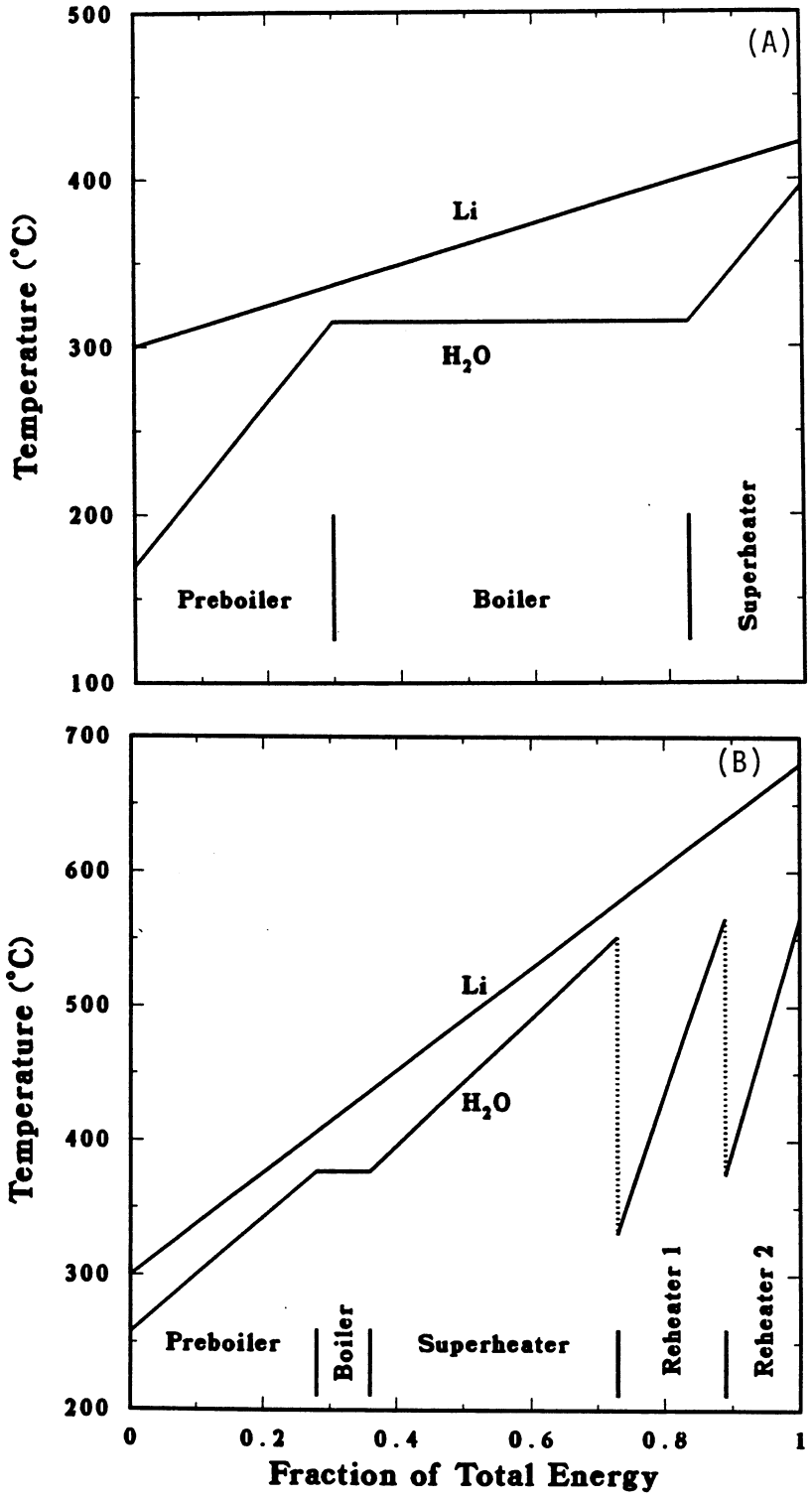

Figure 10.6-3. Temperature-energy diagram for the first-wall and divertor (A) and IBC and shield (B) power cycles.

Table 10.6-II.

PARAMETERS OF THE TITAN-I POWER CYCLE

First-wall and divertor power cycle:		
Total thermal power in the primary coolant	765	MWt
Primary-coolant inlet temperatures	320	°C
Primary-coolant exit temperatures	442	°C
Secondary-coolant inlet temperatures	300	°C
Secondary-coolant exit temperatures	422	°C
Throttle steam temperature	396	°C
Throttle steam pressure	10.7	MPa
Steam flow rate	326	kg/s
Condenser back pressure	6.76×10^3	Pa
Stages of feed-water heating	4	
Feed-water inlet temperature	169	°C
Gross thermal efficiency	37.0%	
IBC and shield power cycle:		
Total thermal power in the primary coolant	2170	MWt
Primary-coolant inlet temperatures	320	°C
Primary-coolant exit temperatures	700	°C
Secondary-coolant inlet temperatures	300	°C
Secondary-coolant exit temperatures	680	°C
Steam temperature after 1st reheat	565.6	°C
Steam temperature after 2nd reheat	550.0	°C
Throttle steam pressure	21.4	MPa
Steam flow rate	703	kg/s
Condenser back pressure	6.76×10^3	Pa
Stages of feed-water heating	7	
Feed-water inlet temperature	258	°C
Gross thermal efficiency	46.5%	
Overall gross thermal efficiency	44.0%	

10.6.4. Summary

The total thermal power of TITAN-I is removed from the reactor core by two different primary-coolant streams: the first-wall and divertor circuit with a mixed exit temperature of 442 °C, and the IBC and shield circuit with an exit temperature of 700 °C. In order to maximize the overall thermal efficiency, two separate Rankine power cycles are used.

The first-wall and divertor power cycle is a superheat Rankine cycle with no reheat and four stages of feed-water heating with a gross efficiency of 37.0%. The IBC and shield power cycle is a two-stage reheat, superheat Rankine cycle with seven stages of feed-water heating with a gross thermal efficiency of 46.5%. The resulting overall gross thermal-conversion efficiency of TITAN-I is 44%.

10.7. SUMMARY AND CONCLUSIONS

The TITAN-I reactor is a compact, high-neutron-wall-loading (18 MW/m^2) design. A comprehensive list of the operating parameters of TITAN-I can be found in Appendix A. The TITAN-I fusion power core (FPC) is cooled by liquid lithium and uses a vanadium alloy (V-3Ti-1Si) as the structural material. The V-3Ti-1Si is chosen primarily because of its irradiation behavior, its high-temperature capabilities, and its compatibility with liquid lithium. The radiation lifetime of this alloy is estimated to be 15 to 18 MW y/m^2, with the lower limit resulting in one year of operational life at 75% availability. The neutronics performance of this lithium-vanadium system is good, with a tritium-breeding ratio of 1.18 (from 3-D neutronics calculations), and an energy multiplication of 1.14 using 30% enriched lithium.

High-velocity (20 m/s) liquid lithium flowing in the turbulent regime cools the first wall and divertor plates. A thermal-hydraulics design window has been computed, revealing a maximum heat flux capability of $\sim 5\,MW/m^2$ under the conditions of TITAN-I. A separate low-velocity lithium circuit cools the IBC and hot shield. Separation of the two coolant circuits leads to the option of dual power cycles with a combined gross efficiency of 44%.

The TITAN-I blanket is arranged as an integrated blanket coil (IBC) with the lithium coolant also acting as the conductor for the toroidal-field and divertor magnets. The IBC eliminates the need for separate coils and neutron shielding for such coils, thereby simplifying the FPC and making the reactor torus assembly more accessible. The IBC system

requires high-current, low-voltage power supplies and appears feasible with current technology. The power-supply cost for the TF IBCs is moderate ($\sim$ 50 M\$); the development of large, steady-state homopolar generators could reduce this cost.

The TITAN-I design shows that liquid-metal-cooled high-power-density RFP reactors appear feasible and attractive. Feasibility issues for this concept have been addressed and resolved, given the inadequacy of experimental data in certain areas. As always, further research is needed to validate the technological requirements of TITAN-I design.

REFERENCES

[1] D. L. Smith, B. A. Loomis, and D. R. Diercks "Vanadium-Base Alloys For Fusion Reactor Applications – A Review," *J. Nucl. Mater.* **135** (1985).

[2] D. L. Smith, G. D. Morgan, M. A. Abdou, C. C. Baker, J. D. Gordon, *et al.*, "Blanket Comparison and Selection Study – Final Report," Argonne National Laboratory report ANL/FPP-84-1 (1984).

[3] E. E. Bloom, "Mechanical Properties of Materials in Fusion Reactor First-Wall and Blanket Systems," *J. Nucl. Mater.* **85-86** (1979) 795.

[4] B. A. Loomis and O. Carlson, *Proc. 3rd Annual Conf. on Reactive Metals*, Buffalo, NY (1985) 227.

[5] K. Natesan, "Influence of Nonmetallic Elements on the Compatibility of Structural Materials with Alkali Metals," *J. Nucl. Mater.* **115** (1983) 251.

[6] D. N. Braski, "The Effect of Neutron Irradiation on the Tensile Properties and Microstructure of Several Vanadium Alloys," in *Proc. ASTM Conf. on Fusion Reactor Materials*, Seattle, WA (1986).

[7] I. LeMay, *Principles of Mechanical Metallurgy*, Elsevier, New York (1982) p. 367.

[8] S. S. Manson and C. R. Ensign, NASA report TM.X-52999 (1971).

[9] N. M. Ghoniem and R. W. Conn, "Assessment of Ferritic Steels for Steady State Fusion Reactors," *Fusion Reactor Design and Technology* **II**, International Atomic Energy Agency, IAEA-TC-392-62 (1983) p. 389.

[10] D. L. Harrod and R. E. Gold, "Mechanical Properties of Vanadium and Vanadium-Base Alloys," *Int. Met. Rev.* **4** (1980) 163.

[11] R. E. Gold and R. Bajaj, "Mechanical Properties of Candidate Vanadium Alloys for Fusion Applications," *J. Nucl. Mater.* **122-123** (1984) 759.

[12] "ASME Boiler and Pressure Vessel Code, 1977 Code Cases-Nuclear Components," 1977 edition, Case N-47 (1977) 1592-10.

[13] D. N. Braski, "The Effects of Helium on the Tensile Properties of Several Vanadium Alloys," in *Alloy Development for Irradiation Performance,* U. S. Department of Energy report DOE/ER-0045/13 (1984).

[14] "Materials Handbook for Fusion Energy Systems," Department of Energy report DOE/TIC-10122 (1980).

[15] G. Plotter, ORNL-Isotope Sales Office, private communications (March 1987).

[16] M. S. Freed and K. J. Kelly, "Nuclear Propulsion Program Quarterly Report," Pratt & Whitney Aircraft Division of United Aircraft Corp. report PWAC-355 (1961).

[17] J. R. DiStefano, Oak Ridge National Laboratory report ORNL-3551 (1964).

[18] D. L. Smith, R. H. Lee, and R. M. Yonco, *Proc. 2nd Int. Conf. on Liquid Metal Technology in Energy Production*, Richland, WA CONF-800401-P2 (1980) 2-72.

[19] R. L. Ammon, "Vanadium and Vanadium-Alloy Compatibility Behaviour with Lithium and Sodium at Elevated Temperatures," *Int. Metals Rev.* **4** (1980) 255.

[20] R. L. Klueh, "The Effect of Oxygen on the Corrosion of Niobium and Tantalum by Liquid Lithium," Oak Ridge National Laboratory report ORNL-TM-4069 (1973).

[21] R. L. Klueh, *Corrosion by Liquid Metals,* J. E. Draley and J. R. Weeks (Eds.), Plenum Press, New York (1970) pp. 177-196.

[22] R. W. Harrison, *Corrosion by Liquid Metals,* J. E. Draley and J. R. Weeks (Eds.), Plenum Press, New York (1970) pp. 217-250.

[23] C. W. Hickum, Jr., "Corrosion Products of the Tantalum-Interstitial Oxygen-Potassium System at 1800°F (982°C)," *J. Less Common Met.* **14** (1968) 315.

[24] E. E. Hoffman, "Corrosion of Materials by Lithium at Elevated Temperatures," Oak Ridge National Laboratory report ORNL-2674 (1959).

[25] E. E. Hoffman and R. W. Harrison, "The Compatibility of Refractory Metals with Liquid Metals," *Proc. Symposium on Metallurgy and Technology of Refractory Metals*, Washington, D. C. (1968) 251.

[26] V. A. Lyashenko, *Proc. 2nd United Nations Int. Conf. on Peaceful Uses of Atomic Energy*, Geneva **7** (1958) 111.

[27] W. F. Brehm, Jr., J. L. Gregg, and Li Che-Yu, *Trans. AIME* **242** (1968) 1205.

[28] H. U. Borgstedt, "Zur Bestandigkeit des Vanadiums und der Legierung V-3Ti-15Nb in Flussigem Lithium bei 700°C," *J. Nucl. Mater.* **51** (1974) 221.

[29] W. E. Ray, R. L. Miller, S. L. Schrock, and G. A. Whitlow, "The Structure of Sodium Corrosion Deposits and their Effects on Heat Transfer," *Nucl. Technol.* **16** (1972) 249.

[30] M. G. Kamdar, *Fracture* **1** (1977) 387.

[31] F. L. LaQue and H. R. Copson (Eds.), *Corrosion Resistance of Metals and Alloys,* 2nd edition, Reinhold Publishing Corporation, New York (1963).

[32] W. D. Manly, "Fundamentals of Liquid Metal Corrosion," *Corrosion* **12** (1956) 336.

[33] C. H. Adelhelm, H. U. Borgstedt, and J. Konys, "Corrosion of V-3Ti-1Si in Flowing Lithium," *Fusion Technol.* **8** (1985) 541.

[34] O. K. Chopra and D. L. Smith, "Corrosion Behavior of Vanadium Alloys in Flowing Lithium," in *Proc. 3rd Int. Conf. on Fusion Reactor Materials*, Karlsruhe, Federal Republic of Germany (1987).

[35] J. H. DeVan and R. L. Klueh, "The Effect of Oxygen on the Corrosion of Vanadium and V-20%Ti by Liquid Lithium," *Nucl. Technol.* **24** (1974) 64.

[36] F. A. Schmidt and J. C. Warner, "Diffusion of Carbon, Nitrogen, and Oxygen in Vanadium between 60 and 1825°C," *J. Less Common Met.* **26** (1972) 325.

[37] R. W. Powers and M. V. Doyle, *J. App. Phys.* **30** (1959) 514.

[38] E. A. Gulbransen and K. F. Andrews, *J. Electrochem. Soc.* **97** (1950) 396.

[39] T. S. Verkhoglynadova, T. C. Dubovik, and G. V. Samsonov, *Poroshk. Metall.* **1** (1961) 9.

[40] D. L. Olson, G. N. Reser, and D. K. Matlock, "Liquid Lithium Corrosion Rate Expressions for Type 304 L Stainless Steel," *Corrosion* **36** (1980) 140.

[41] R. A. Shunk, *Constitution of Binary Alloys,* Second supplement, McGraw Hill, New York (1969) p. 166.

[42] E. Veleckis and R. K. Edwards, "Thermodynamic Properties in the System Vanadium-Hydrogen, Niobium-Hydrogen, and Tantalum-Hydrogen," *J. Phys. Chem.* **67** (1969) 683.

[43] J. R. Mareche, C. J. Rat, and A. Herold, *J. Phys. Chem.* **73** (1976) 1.

[44] R. Cantelli, F. M. Mazzolai, and M. Nouvo, *J. Phys. Chem. Solids* **31** (1970) 1811.

[45] B. Craig, "Hydrogen Damage," *Metals Handbook,* 9th edition **13** (1987) 171.

[46] A. Coulon *et al.*, "Erosion and Erosion Corrosion of Metals," *Proc. 5th Int. Conf. on Erosion by Solid and Liquid Impact*, Newnham College Cambridge, U. K. (1979) 25-1.

[47] J. E. Field *et al.*, "Liquid Jet Impact and Damage Assessment for Brittle Solids," *Proc. 5th Int. Conf. on Erosion by Solid and Liquid Impact*, Newnham College Cambridge, U. K. (1979) 13-1.

[48] G. Dearnaley, "Ion Implantation and Ion Beam Mixing in Corrosion Science and Technology," *Proc. of an Int. Sym. Cosponsored by the Corrosion Division of the Electrochemical Soc. and the European Federation of Corrosion*, Pennington, NJ (1983) 1-16.

[49] G. W. Vickers, "Characterization and Determination of Erosion Damage Resulting from Liquid Jet Impact," Ph. D. Thesis, University of Manchester, Institute of Science and Technology, U. K. (1972).

[50] J. E. Field, S. van der Zwaag, and D. Townsend, "Liquid Impact Damage Assessment for a Range of Infra-Red Materials," *Proc. of 6th Int. Conf. on Erosion by Liquid and Solid Impact*, Newnham College, U. K. (1983) 21-1.

[51] B. J. Hockey, "Erosion of Ceramic Materials: The Role of Plastic Flow," *Proc. 5th Int. Conf. on Erosion by Solid and Liquid Impact*, Newnham College Cambridge, U. K. (1979) 26-1.

[52] L. G. Hays, "Corrosion of Niobium-1% Zirconium Alloy and Yttria by Lithium at High Flow Velocities," NASA-JPL Technical report 32-1233 (1967).

[53] E. Schnetzer (Ed.), "3000-Hour Test Two-Stage Potassium Turbine," NASA report NASA CR-72273 (1967).

[54] P. F. Tortorelli and J. H. DeVan, "Corrosion of Path A PCA, Type 316 Stainless Steel and Fe-12Cr-1MoVW Steel in Flowing Lithium," in *Alloy Development for Irradiation Performance*, Semi-annual Progress Report for Period Ending March 1986, U. S. Department of Energy report DOE/ER-0045/16 (1986).

[55] P. F. Tortorelli and J. H. DeVan, "Corrosion of an Fe-12Cr-1MoVW Steel in Thermally Convective Lithium," *Proc. Topical Conf. on Ferritic Alloys for use in Nuclear Energy Technologies*, Snowbird, UT (1983) 215.

[56] O. K. Chopra and D. L. Smith, "Corrosion of Austenitic and Ferritic Steels in Flowing Lithium Environment," in *Alloy Development for Irradiation Performance*, Semi-annual Progress Report for Period Ending March 1986, U. S. Department of Energy report, DOE/ER-0045/16 (1986).

[57] H. U. Borgstedt, M. Grundmann, and J. Konys, "Studies of Corrosion and Impact on Mechanical Properties of SS 304 and 12% Cr Steel by Liquid Lithium," *Fusion Technol.* **8** (1985) 536.

[58] G. E. Bell, Oak Ridge National Laboratory, private communications.

[59] C. Bagnall, G. C. Burrow, M. G. Down, and Z. L. Kardos, "Chemistry Control by Trapping in a Liquid Lithium System," *J. Mater. for Energy Systems* **3** (1981) 222.

[60] J. R. Weston, W. F. Calaway, R. M. Yonco, and V. A. Maroni, in *Proc. 2nd Int. Conf. on Liquid Metal Tech. in Energy Production*, CONF-800401-P2, Richland, WA (1980).

[61] P. F. Tortorelli, J. H. DeVan, and J. E. Selle, "Effects of Nitrogen in and Nitrogen-Getters in Lithium on the Corrosion of Type 316 Stainless Steel," in *Proc. Int. Corrosion Forum Devoted to the Protection and Performance of Materials*, National Association of Corrosion Engineers, Atlanta, GA (1979).

[62] "Nuclear Propulsion Program," Pratt & Whitney Aircraft Division of United Aircraft Corp. reports PWAC-573, PWAC-574, PWAC-581 (1957-1958).

[63] P. F. Tortorelli, J. H. DeVan, J. E. Selle, and H. P. Upton, *Proc. 8th Symp. on Eng. Problems of Fusion Research*, San Francisco, CA, IEEE report 79CH1441-5 NPS (1979) 1610.

[64] M. S. Goikham, V. F. Shatinskii, and S. V. Rybakov, "Increasing the Life of 12Kh18N10T Steel and EI437B Alloy in Lithium," *Sov. Mater. Sci.* (1979) 510.

[65] G. A. Whitlow, R. L. Miller, W. L. Wilson, and T. A. Galioto, "Observations on the In-Sodium Corrosion Tribology of Aluminide Coatings on Inconel-718," *Microstructural Sci.* **3** (1975) 775.

[66] G. C. Burrow, M. G. Down, and C. Bagnall, "Corrosion Inhibition Experiments in Liquid Lithium," *J. Nucl. Mater.* **103-104** (1981) 657.

[67] "SINTIMID: Der neue Polymidwerkstoff," Metallwerk Plansee GmbH, A-6600 Reutte/Tirol, Austria (1987).

[68] G. B. Engle and W. P. Eatherly, *High Temperature-High Pressure* **4** (1972) 119.

[69] J. L. Kaae, "Effect of Irradiation on the Mechanical Properties of Isotropic Pyrolytic Carbons," *J. Nucl. Mater.* **46** (1973) 121.

[70] G. R. Hopkins and R. J. Price, "Fusion Reactor Design with Ceramics," *Nucl. Eng. Des./Fusion* **2** (1985) 111.

[71] R. J. Price, "Neutron Irradiation-Induced Voids in β-Silicon Carbide," *J. Nucl. Mater.* **48** (1973) 47.

[72] R. J. Price, "Properties of Silicon Carbide for Nuclear Fuel Particle Coatings," *Nucl. Technol.* **35** 1977.

[73] Hitachi/Toshiba Company, private communications.

[74] G. P. Pells, "Ceramic Materials for Fusion Reactor Application," *J. Nucl. Mater.* **122-123** (1984) 1338.

[75] K. Tanimura, N. Itoh, and F. W. Clinard, Jr., "Volume Change in Al_2O_3 and $MgAl_2O_4$ Induced by 14-MeV Neutron Irradiation," *J. Nucl. Mater.* **150** (1987) 182.

[76] G. F. Hurley and F. W. Clinard, Jr., "Fracture Toughness and Hardness of Neutron-Irradiated Al_2O_3, $MgAl_2O_4$," and $Y_3Al_5O_{12}$," *Special Purpose Materials*, Annual Progress Report Ending October 1979, U. S. Department of Energy report DOE/ER-0048/1 (1980) 51.

[77] F. W. Clinard, Jr., G. F. Hurley, L. W. Hobbs, D. L. Rohr, and R. A. Youngman, "Structural Performance of Ceramics in a High-Fluence Fusion Environment," *J. Nucl. Mater.* **122-123** (1984) 1386.

[78] C. A. Parker, L. W. Hobbs, K. C. Russel, and F. W. Clinard, Jr., "Damage Structures in Fast Neutron Irradiated Magnesium Aluminate and Electron Irradiated Aluminum Oxynitride Spinels," *J. Nucl. Mater.* **133-134** (1985) 741.

[79] F. W. Clinard, Jr., L. W. Hobbs, and R. A. Youngman, "Microstructure of Neutron-Irradiated $MgAl_2O_4$," *Special Purpose Materials*, Annual Progress Report Ending October 1979, U. S. Department of Energy report DOE/ER-0048/1 (1980) 59.

[80] G. W. Keilholtz, P. E. Moore, H. E. Robertson, Oak Ridge National Laboratory report ORNL-4678 (1971).

[81] G. F. Hurley, J. C. Kennedy, F. W. Clinard, Jr., R. A. Youngman, and W. R. McDonell, "Structural Properties of MgO and $MgAl_2O_4$ after Fission Neutron Irradiation Near Room Temperature," *J. Nucl. Mater.* **103-104** (1981) 761.

[82] F. W. Clinard, Jr., "Ceramics for Application in Fusion Systems," *J. Nucl. Mater.* **85-86** (1976) 393.

[83] F. W. Clinard, Jr., "Ceramics for Fusion Devices," *J. Mater. For Energy Systems* **6** (1984) 100.

[84] G. F. Hurley and F. W. Clinard, Jr., "Swelling of Neutron-Irradiated Al_2O_3 and $MgAl_2O_4$," *Special Purpose Materials*, Annual Progress Report Ending October 1979, U. S. Department of Energy report DOE/ER-0048/1 (1980) 45.

[85] F. W. Clinard, Jr. and G. F. Hurley, "Ceramic and Organic Insulators for Fusion Applications," *J. Nucl. Mater.* **103-104** (1981) 705.

[86] F. W. Clinard, Jr., G. F. Hurley, and L. W. Hobbs, "Neutron Irradiation Damage in MgO, Al_2O_3 and $MgAl_2O$ Ceramics," *J. Nucl. Mater.* **108-109** (1982) 655.

[87] W. A. Coghlan, F. W. Clinard, Jr., N. Itoh, and L. R. Greenwood, "Swelling of Spinel after Low-Dose Neutron Irradiation," in *Proc. 2nd Int. Conf. on Fusion Reactor Materials,* Chicago, IL (1986).

[88] W. Klaffky,"Radiation-Induced Conductivity of Al_2O_3," *Special Purpose Materials*, Annual Progress Report Ending October 1979, U. S. Department of Energy report DOE/ER-0048/1 (1980) 19.

[89] G. P. Pells, S. N. Buckley, G. J. Hill, and M. J. Murphy, "Radiation Effects in Electrically Insulating Ceramics," Harwell Laboratory report AERE-R 11715 (1985).

[90] R. W. Klaffky, "RIC of Al_2O_3 Experiment and Theory," *Phys. Rev. B* **21** (1980) 3610.

[91] J. W. McCauley and N. D. Corbin, *Progress in Nitrogen Ceramics*, F. L. Riley (Ed.), Martinus Nijhof, Boston (1983) 111.

[92] J. D. Lee (Ed.), "MINIMARS Conceptual Design: Final Report," Lawrence Livermore National Laboratory report UCID-20773 (1986) Vol. 1, Sec. 10.

[93] M. E. Sawan and P. L. Walstrom, "Superconducting Magnet Radiation Effects in Fusion Reactors," *Fusion Technol.* **10** (1986) 741.

[94] W. W. Engle, Jr., "A User's Manual for ANISN, A One-Dimensional Discrete Ordinates Transport Code with Anisotropic Scattering," Oak Ridge Gaseous Diffusion Plant report K-1693 (1967).

[95] R. MacFarlane, "Nuclear Data Libraries from Los Alamos for Fusion Neutronics Calculations," *Trans. Am. Nucl. Soc.* **36** (1984) 271.

[96] Code of Federal Regulations, "Licensing Requirements for Land Disposal of Radioactive Waste," Title 10, part 61, Nuclear Regulatory Commission, Washington, DC (December 1982).

[97] J. F. Briesmeister (Ed.), "MCNP – A General Monte Carlo Code for Neutron and Photon Transport, Version 3A," Los Alamos National Laboratory report LA-7396-M, Rev. 2 (1986).

[98] J. H. Holroyd and J. T. D. Mitchell, "Liquid Lithium as Coolant for Tokamak Fusion Reactors," Culham Laboratory report CLM-R231 (1982).

[99] R. W. Moir, J. D. Lee, W. S. Neef, D. L. Jassby, D. H. Berwald, *et al.*, "Feasibility Study of a Fission Suppressed Tokamak Fusion Breeder," Lawrence Livermore National Laboratory report UCID-20514 (1984).

[100] J. C. R. Hunt and R. Hancox, "The Use of Liquid Lithium as Coolant in a Toroidal Fusion Reactor, Part I Calculation of Pumping Power," Culham Laboratory report (1971).

[101] D. K. Sze, R. Clemmer, and E. T. Cheng, "LiPb, A Novel Material for Fusion Applications,"in *Proc. 4th ANS Topical Meeting on the Technology of Controlled Nuclear Fusion*, King of Prussia, PA (1980).

[102] B. G. Logan *et al.*, "Mirror Advanced Reactor Study (MARS)," Lawrence Livermore National Laboratory report UCRL-53563 (1984).

[103] C. Copenhaver, R. A. Krakowski, N. M. Schnurr, R. L. Miller, C. G. Bathke, *et al.*, "Compact Reversed-Field-Pinch Reactor (CRFPR): Fusion-Power-Core Integration Study," Los Alamos National Laboratory report LA-10500-MS (1985).

[104] D. Steiner, R. C. Block, and B. K. Malaviya, "The Integrated Blanket-Coil Concept Applied to the Poloidal Field and Blanket Systems of a Tokamak," *Fusion Technol.* **7** (1985) 66.

[105] M. Z. Hasan and N. M. Ghoniem, "The Use of Liquid-Metal Coolants in the Thermal-Hydraulic Design of the First Wall and Blanket of High-Power-Density Fusion Reactors," University of California Los Angeles report UCLA-PPG-1086/ENG-8742 (1987).

[106] R. A. Gardner, "Laminar Pipe Flow in a Transverse Magnetic Field with Heat Transfer," *Int. J. Heat and Mass Transfer* **7** (1968) 1076.

[107] H. Madarame and M. S. Tillack, "MHD Flow in Liquid-Metal Blankets with Helical Vanes," University of California Los Angeles report UCLA-ENG-8616/PPG-948 (1986).

[108] F. Issaci, N. M. Ghoniem, and I. Catton, "Magnetohydrodynamic Flow in a Curved Pipe," *Phys. of Fluids* **31** (1988) 65.

[109] R. A. Gardner and P. S. Lykoudis, "Magneto-fluid-mechanics Pipe Flow in a Transverse Magnetic Field, Part 1, Isothermal Flow," *J. Fluid Mech.* **47** (1971) 737.

[110] A. L. Loeffler, M. Macuilatis, and M. A. Hoffman, "MHD Round Pipe Flow Experiments," U. S. Air Force report USAF-RAL 67-0236 (1967).

[111] A. L. Joumotte and C. Hirsch, "Ecoulement Magnetohydrodynamique en Conduites," *Mechanique Applique* (1967) 960.

[112] S. Globe, "The Effect of Longitudinal Magnetic Field on Pipe Flow of Mercury," *J. Heat Transfer* **83** (1961) 445.

[113] F. W. Fraiz, "The Effect of Strong Longitudinal Magnetic Field on the Flow of Mercury in a Circular Tube," Ph. D. Thesis, Massachusetts Institute of Technology (1966).

[114] M. A. Hoffman, "Magnetic Field Effect on the Heat Transfer of Potential Fusion Reactor Coolants," Lawrence Livermore National Laboratory report UCRL-33993 (1972).

[115] P. S. Lykoudis, "Transition from Laminar to Turbulent Flow in Magneto-fluid-mechanic Channels," *Rev. Mod. Phys.* **32** (1960) 796.

[116] H. Branover, S. Sukoriansky, G. Talmage, and E. Greenspan, "Turbulence and the Feasibility of Self-Cooled Liquid Metal Blankets for Fusion Reactors," *Fusion Tech.* **10** (1986) 822.

[117] D. S. Kovner, E. Yu. Krasilnikov, and I. C. Panevin, "Experimental Study of the Effects of a Longitudinal Magnetic Field on Convective Heat Transfer in a Turbulent Tube Flow of Conducting Liquid," *Magnitnaya Gidrodinamika* **2** (1966) 101.

[118] R. A. Gardner and P. S. Lykoudis, "Magento-fluid-mechanics Pipe Flow in a Transverse Magnetic Field, Part 2, Heat Transfer," *J. Fluid Mech.* **48** (1971) 129.

[119] E. Yu. Krasilnikov, "The Effect of a Transverse Magnetic Field upon Convective Heat Transfer in Magnetohydrodynamic Channel Flow," *Magnitnaya Gidrodinamika* **1** (1965) 37.

[120] H. Schlichting, *Boundary Layer Theory,* 7th edition, McGraw-Hill, New York (1979).

[121] C. C. Cheng and T. S. Lundgren, "Duct Flow in MHD," *Z. Angew. Math. Phys.* **12** (1961) 100.

[122] E. E. Sechler, *Elasticity in Engineering,* John Wiley & Sons, Inc., New York (1952).

[123] R. A. Bolay and J. H. Weimer, *Theory of Thermal Stress,* John Wiley & Sons, Inc., New York (1960).

[124] M. Z. Hasan, "A Computer Code for Optimum Thermal-Hydraulic Design of the First Wall and Blanket of a Reversed-Field-Pinch Fusion Reactor," University of California Los Angeles report UCLA-PPG-1045 (1987).

[125] G. J. DeSalvo and J. A. Swanson, "ANSYS User's Manual," Swanson Analysis Systems, Inc. (1979).

[126] I. J. Karassik, W. C. Krutzsch, W. H. Fraser, and J. P. Messina (Eds.), *Pump Handbook,* McGraw-Hill, New York (1976).

[127] M. Z. Hasan, "Effects of Non-uniform Surface Heat Flux and Uniform Volumetric Heating on Blanket Design for Fusion Reactors," *Fusion Technol.* **16** (1989) 44.

[128] O. W. Eshbach and M. Souders (Eds.), *Handbook of Engineering Fundamentals,* 3rd edition, John Wiley & Sons, Inc., New York (1975).

[129] *Handbook of Structural Stability,* edited by Column Research Committee of Japan, Tokyo (1971) 4-235.

[130] K. Natesan and D. L. Smith, "The Influence of nonmetallic Impurities on the Compatibility of Liquid Lithium with Potential CTR Containment Materials," *Nucl. Technol.* **22** (1974) 392.

[131] L. C. Fuller and T. K. Stovall, "User's Manual for PRESTO: A Computer Code for the Performance of Regenerative Superheated Steam-Turbine Cycles," Oak Ridge National Laboratory report ORNL-5547, NASA CR-159540 (1975).